universität wien

DISSERTATION

Titel der Dissertation

Selectivity and conduction studies in bacterial voltage-gated sodium channels by molecular dynamics simulations

Verfasser

Song Ke, MSc

angestrebter akademischer Grad

Doktor der Naturwissenschaften (Dr. rer. nat.)

Wien, 2015

Studienkennzahl lt. Studienblatt:	A 796 610 449
Dissertationsgebiet lt. Studienblatt:	Pharmazie
Betreuer:	Mag. Dr. Anna Weinzinger, Assistant Prof. Hannes Todt, M.D.

Abstract

Voltage gated Na^+ channels are essential for the generation of action potentials, and thus are vital for mediating heart rates, neuronal signal transductions and muscle contractions. Selective ion permeation is a critical biological function of these channels. Recently released 3-D crystal structures of bacterial voltage-gated sodium ion channels provide great opportunities to unravel key structural functions and mechanisms of their vertebrate counterparts at atomistic level. This thesis presents three scientific publications, focusing on exploring the ion selectivity between sodium and calcium ions, sodium ion conductance mechanisms and structural dynamics as well as investigations of potential drug access pathways for charged channel blockers, in the vicinity of the selectivity filter domain via molecular dynamics simulations.

This thesis elucidates the energetic differences between sodium and calcium ion permeations through the selectivity filter. A key structural configuration of the selectivity filter during outward transition simulations is discovered and suggested to be crucial in initiating channel slow inactivation. A potential external engineered access pathway for positive charged local anesthetics via a mutant in the selectivity filter is also proposed. In summary, this thesis indicates the feasibilities of utilizing bacterial voltage gated sodium channels as templates to probe key channel functions of mammalian sodium channels and sheds light on key roles of the selectivity filter domain with regard to ion conduction, selectivity and drug access.

Zusammenfassung

Spannungsgesteuerte Na+ Kanäle sind essentiell für die Generierung von Aktionspotentialen und in weiterer Folge wichtig für die Regulierung von Herzfrequenzen, die neuronale Signalübertragung und Muskelkontraktionen. Ein selektiver Ionenfluss ist hierbei essentiell für die biologische Funktion dieser Kanäle. Kürzlich veröffentlichte 3-D-Strukturen von bakteriellen spannungsgesteuerten Natriumionenkanälen bieten große Chancen, wichtige strukturelle Funktionen und Mechanismen auf atomarer Ebene zu verstehen. In dieser Dissertation werden drei wissenschaftliche Publikationen präsentiert. Analysiert werden die Ionenselektivität zwischen Natrium und Calcium-Ionen, der Natriumfluss und Strukturdynamik des Filters, sowie potenzielle Arzneimittelzugangswege für geladene Kanalblocker. Die Methode der Wahl ist hierbei die Moleküldynamiksimulation. Diese Arbeit zeigt unter anderem energetischen Unterschiede zwischen Natrium- und Calciumionenfluss durch den Selektivitätsfilter. Außerdem konnte gezeigt werden, dass Konfigurationsänderungen im Selektivitätsfilter abhängig von der Richtung des Ionenflusses sind. Diese Strukturänderungen könnten eine entscheidende Rolle bei der Initiierung der langsamen Inaktivierung spielen. In der dritten Publikation wird ein möglicher externer, mutationsgenerierter Zugangsweg für positiv geladene Lokalanästhetika im Bereich des Selektivitätsfilters analysiert. Zusammenfassend zeigt diese Arbeit das bakterielle Natriumkanäle als Vorlage für ein besseres Verständnis der Funktionen von Säugetiernatriumkanälen geeignet ist. Es konnten wichtige Einblicke in die Selektivität, Dynamik, den Ionenfluss und mögliche Zugangswege für Arzneistoffe gewonnen werden.

Acknowledgements

First and foremost, I am very grateful to my supervisor Dr. Anna Weinzinger for accepting me into her group at Department of Pharmacology and Toxicology, University of Vienna. Her enthusiasm and dedication to unravel the profound structural and dynamic information of biomolecules keep motivate me to explore this intriguing and challenging field. I have gained considerable expertise and experience from her helpful discussions, novel scientific insights and exceptional writing skills. Moreover, her considerate understanding and tolerance really helps me to go through the hard time during my studies.

I would like to thank the PhD program, Molecular Drug Targets (MolTag) from Austrian Science Fund. Especially, the speaker of this program, Prof. Steffen Hering, who is also the head of the Department, organizes this successful program and provides large amounts of conveniences for daily administrations of my work in Vienna.

I thank my colleagues Tobias Linder and Eva-Maria Zangerl in the molecular modeling group, who create a truly interactive and helpful environment with Gromacs, scripting, programming and scientific discussions as well as their helps for coordinating my life in Vienna.

I want to express my gratitude to Dr. Ulrich Zachariae, a fantastic host to allow me to carry out my internship in Dundee. I deeply admire his sophisticated biophysical knowledge and vivid explanations of those theoretical backgrounds. I especially appreciate for his kind and generous help when I was in critical conditions.

I thank our collaborators, Prof. Hannes Todt, who is also my co-supervisor, Peter Lukacs and Prof. Eugene Timin for their insightful and inspiring discussions in this thesis.

Last but not at least, I want to thank my family, especially my parents Zhi and Liping, and my wife, Yiqiong for their loves and supports during my thesis. Their attitudes and philosophies in life and their firm beliefs in me are keys to help me keep focused, determined, and accomplish this three-year intensive yet interesting scientific adventure.

Table of Contents

Table of Contents

Figure 1.1 of the introduction was reused with permission from *John Wiley and Sons* Ltd: *Journal of Physiology.* **590**:2577–2589. © 2012

Figure 1.2, Figure 1.3, Figure 1.5 and Figure 1.6A of the introduction was reused under open access from *Elsevier.* Ltd: *Journal of Molecular Biology.* **427**:3–30. © 2015

Figure 1.4 of the introduction was reused with permission from *Macmillian Publisher* Ltd: *Nature.* **486:**135–139. © 2012

Figure 1.6B of the introduction was permitted to reuse with non-profit purpose from *the Rockefeller University Press*: *Journal of General Physiology.* **139**:507–516. © 2012

Figure 1.7 of the introduction was reused with permission from *Macmillian Publisher* Ltd: *Nature.* **475**:353–358. © 2011

Figure 1.8A and B of the introduction was reused with permission from *Elsevier.* Ltd: *Biophys. J.* **105**:1737–1745. © 2013

Figure 1.8C of the introduction was reused with permission from *Elsevier.* Ltd: *Biophys. J.***91:** L81–83. © 2006

Figure 3.1 was reused and modified from PhD thesis of C. Kappel (2011) thesis originate from G. Schroeder master thesis: http://www.mpibpc.mpg.de/277968/Kappel-Christian_2011_PhD-Thesis_Goe.pdf

Figure 3.2 was adopted from: http://isaacs.sourceforge.net/phys/pbc.html

Figure 3.1 was reused and modified from Justin Lemkul's tutorial: http://www.bevanlab.biochem.vt.edu/Pages/Personal/justin/gmx-tutorials/umbrella/05_pull.html

Figure 3.5A of the method was reused with permission from *AIP Publishing LLC*: *Journal of Chemical Physics.* **121**:10847–10851. © 2004

Abbreviations

AMBER	Assisted Model Building with Energy Refinement
BacNa_Vs	Bacterial voltage-gated sodium channels
Ca_Vs	Voltage-gated calcium channel
CPU	Central Processing Unit
CTD	C-terminal Domain
FEP	Free Energy Pertubation
GPU	Graphic Processing Unit
GROMACS	GROningen MAchine for Chemical Simulations
K_Vs	Voltage-gated potassium channel
LINCS	LINear Constraint Solver
LJ	Lennard Jones (potential)
LJ-PME	Lennard Jones-Particle Mesh Ewald
MD	Molecular Dynamics
MM	Molecular Mechanics
Na_Vs	Voltage-gated sodium channels
NpT	Isothermal-isobaric Ensemble
NVT	Canonical Ensemble
PB	Poisson-Bolzmann
PBC	Periodic Boundary Conditions
PD	Pore domain
PME	Particle Mesh Ewald
PMF	Potential of Mean Force
QM	Quantum Mechanics
SF	Selectivity Filter

Abbreviations

SIMD	Single Instruction, Multiple Data
TM	Transmembrane
TTX	Tetrodotoxin
vdW	Van der Waals
VSD	Voltage sensor domain
WHAM	Weighted Histogram Analysis Method

1 Introduction (Biological Background)

1.1 Voltage gated sodium channels (Na_VS)

1.1.1 Membrane protein and ion channels

Living cells are encompassed, maintained and protected by biological membranes. These fluid phospholipid bilayers, on the one hand, provide a barrier, and on the other hand, enable selective communication between the cytoplasm and the extracellular fluid via vast amount of polypeptides attached on the surface of, embedded in or penetrated to it. These polypeptides are termed membrane proteins.

Ion channels belong to a major superfamily of membrane proteins expressed ubiquitously in the human body. They can be gated by a variety of triggers (e.g. voltage, ligand, light, pressure, etc) and selectively allow specific ion fluxes (mainly Na^+, K^+, Ca^{2+}, Cl^-, etc) according to concentration and electrochemical gradients across the cell membrane within several milli-seconds. Such rapid and transient processes mediate signal transduction and initiate cellular events in excitable cells.

1.1.2 Overview of voltage gated sodium channels (Na_VS)

More than half a century ago, Hodgkin and Huxley's pioneering studies on action potential of the squid giant axon using the voltage clamp method unveiled that voltage-dependent activation of sodium inward current initiates electrical signals in nerves (Hodgkin and Huxley, 1952a; b; c; d). Mammalian voltage-gated sodium ion channels (Na_VS) were identified as complexes with large α subunits of 260 kDa to suffice their functions. They consist of approximately 2000 amino acids organized in four homologues repeats (I-IV); each of them contains six transmembrane segments including two key functioning modules: a voltage sensor domain (VSD) and a pore domain (PD) (Beneski and Catterall, 1980; Noda et al.,

1986, 1984; Goldin et al., 1986). The α subunits of Na_Vs are of great importance in generation and propagation of action potentials along the cell membrane and are, therefore, essential for the neuronal signaling cascade and the muscle contraction. Activated by the increase of membrane potential via changes of ion concentration gradient across the membrane, Na_Vs exclusively allow abundant inward flux of sodium ions within several milliseconds. This process causes the rising phase or depolarization of the action potential. (Peters and Ruben, 2014; Payandeh and Minor Jr., 2015). This instantaneous current is rapidly eliminated by a mechanism termed fast inactivation rendering the channel non-conductive (discuss in detail in chapter **1.2**). Besides fast inactivation, there exist slow inactivation mechanisms, which last several seconds and even minutes; this special gating phenomenon prolongs depolarizing pulses by reducing the number of channels available to open and then regulates excitability (Silva, 2014). In addition, one or two auxiliary β subunits modulate the kinetics and voltage dependence of activation and inactivation (Isom et al., 1992, 1995) (see **Figure 1.1** for details).

So far, nine human Na_Vs subtypes have been discovered named $Na_V1.1$- $Na_V1.9$. $Na_V1.1$, 1.2, 1.3 and 1.6 are the primary sodium channels in the central nervous system. $Na_V1.7$, 1.8 and 1.9 are primarily located in the peripheral nervous system. $Na_V1.4$ is expressed in skeletal muscle, whereas $Na_V1.5$ is found in the heart (Goldin, 1999). Several mutations in Na_Vs, which induce changes of the structures and functions of the channel, are clinically detrimental and some are even fatal. Mutation induced diseases include long QT and Brugada syndrome ($Na_V1.5$), epilepsy ($Na_V1.1$-1.3 and $Na_V1.6$), periodic paralysis ($Na_V1.4$) and neuropathic pain ($Na_V1.7$-1.9), etc. Details can be found in the review by Andavan and Lemmens-Gruber (Andavan and Lemmens-Gruber, 2011). Site-directed mutagenesis studies suggest that these mutants are associated with almost all key physiological functions including voltage sensing, gating and inactivating, blockade of conducting currents or a complex interplay of these mechanisms. (Peters and Ruben, 2014)

Na_Vs are native targets for a large variety of natural occurring toxins and xenobiotics. Some are benign and beneficial, such as local anesthetics, which do help relieve pain during surgery, whereas toxins like tetrodotoxin, which can cause irreversible block of Na_Vs' outer pore, lead to a sudden loss of heart rate and breath. The interactions of these compounds with Na_Vs facilitate aforementioned key mechanisms of channel functions. Therefore, the development and modifications of small molecules are critical strategies for the treatment of ion channel related diseases termed channelopathies. (Goldschen-Ohm and Chanda, 2014)

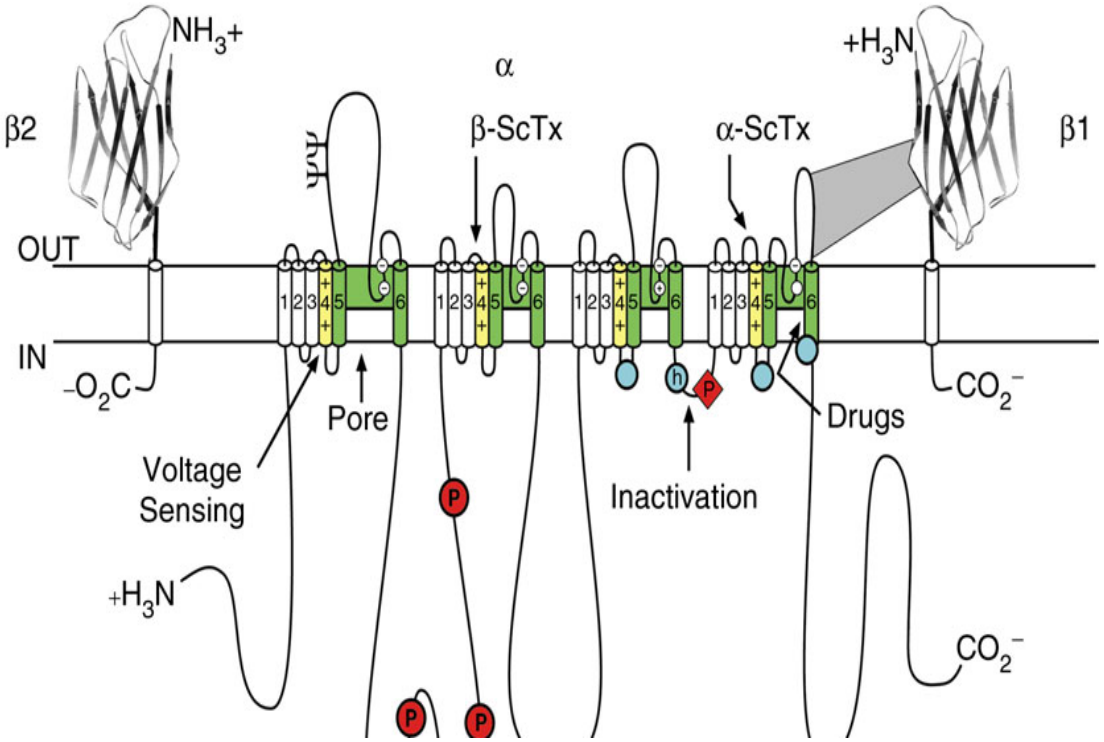

Figure 1.1 The primary structures of the subunits of the voltage-gated sodium channels (adopted from Catterall, 2012). This figure depicts the primary structure of Na_Vs with α, β1 and β2 subunits. Localization of key features of Na_Vs such as voltage-sensing, pore and inactivation gate, drug interaction sites, phosphorylation locus and scorpion toxin interactions sites are also labelled.

1.1.3 Bacterial voltage gated sodium channel (BacNa_Vs)

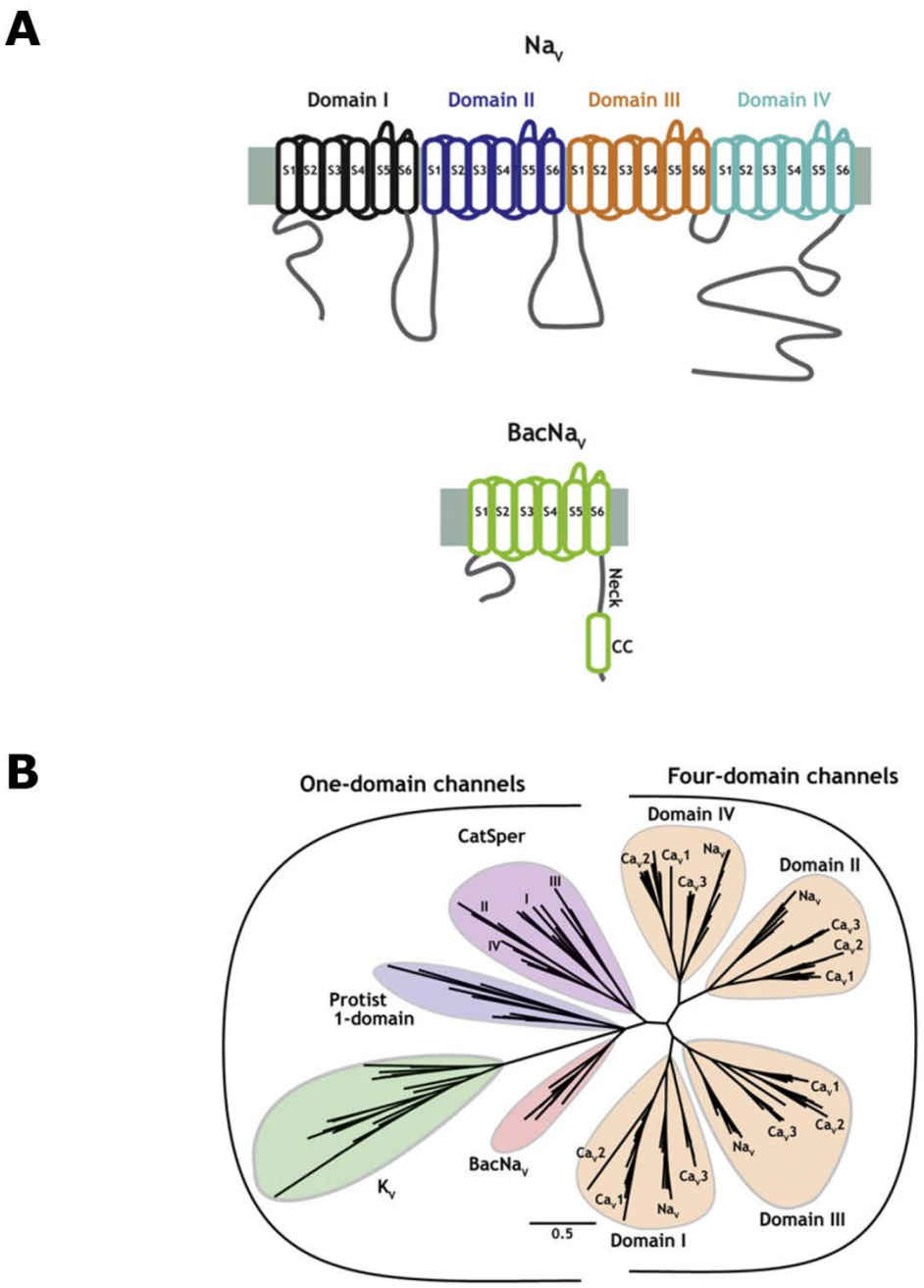

Figure 1.2 BacNa$_V$ topology and relationships to vertebrate counterparts. **A.**Topology diagram comparing eukaryotic Na$_V$ (top) and BacNa$_V$ pore-forming subunits.S1–S6 segments are labeled **(adopted from Payandeh and Minor Jr., 2015); B.**Unrooted phylogenetic tree demonstrating a comparison based on the selectivity filter sequences for BacNa$_V$s compared with K$_V$ channels, CatSper, Protist one-domain channels, and the individual domains of Na$_V$s and Ca$_V$s **(adopted from Payandeh and Minor Jr., 2015 with modifications originated from Liebeskind et al., 2013)**

In 2001, the first bacterial sodium channel homologue NaChBac has been discovered and characterized (Ren et al., 2001; Yue et al., 2002). This channel is composed of homotetramers of a single subunit mimicking each of the four domains of eukaryotic sodium channels (**Figure 1.2A**). Clade analysis suggested that the one-domain NachBac analogues are ancestors of the four-domain mammalian Na_Vs and Ca_Vs and one-domain CatSper channels found in sperm from the calcium channel family (**Figure 1.2B**) (Durell and Guy, 2001; Ren, 2011; Liebeskind et al., 2013). NachBac has been demonstrated to be sodium selective, even though the sequence of the selectivity filter (SF) has more in common with Ca_Vs. The selectivity-conferring residues in the SF of the mammalian Na_Vs are D, E, K, A, which are assumed to form a ring at equivalent positions, whereas this ring is replaced by the EEEE motif in BacNa_Vs akin to mammalian Ca_Vs. Similar to vertebrate Na_Vs, NachBac is voltage gated and inactivated, although activation, inactivation, and recovery from inactivation of NaChBac are 10–100 times slower than that of eukaryotic Na_Vs (Ren et al., 2001). Given the lack of fast inactivation mechanism, BacNa_Vs may utilize solely slow inactivation mechanisms similar to slow-inactivation in vertebrate Na_Vs (Errington et al., 2008; Chen et al., 2000; Fozzard et al., 2005). This is reminiscent of C-type inactivation, a mechanism involving the collapse of the selectivity filter (SF), in K_V channels (Cuello et al., 2010). Compared to fast inactivation, which is initiated by blocking of the intracellular inactivation gate, slow inactivation is modulated by conformational changes of the pore domain (Carboni et al., 2005; Irie et al., 2010).

NachBac is not sensitive to the sodium channel blocker TTX, but sensitive to sodium and calcium blockers, lidocaine (Lee et al., 2012) and dihydropyridine (Ren et al., 2001) derivatives.

1.1.4 Crystallized structures of BacNa_Vs

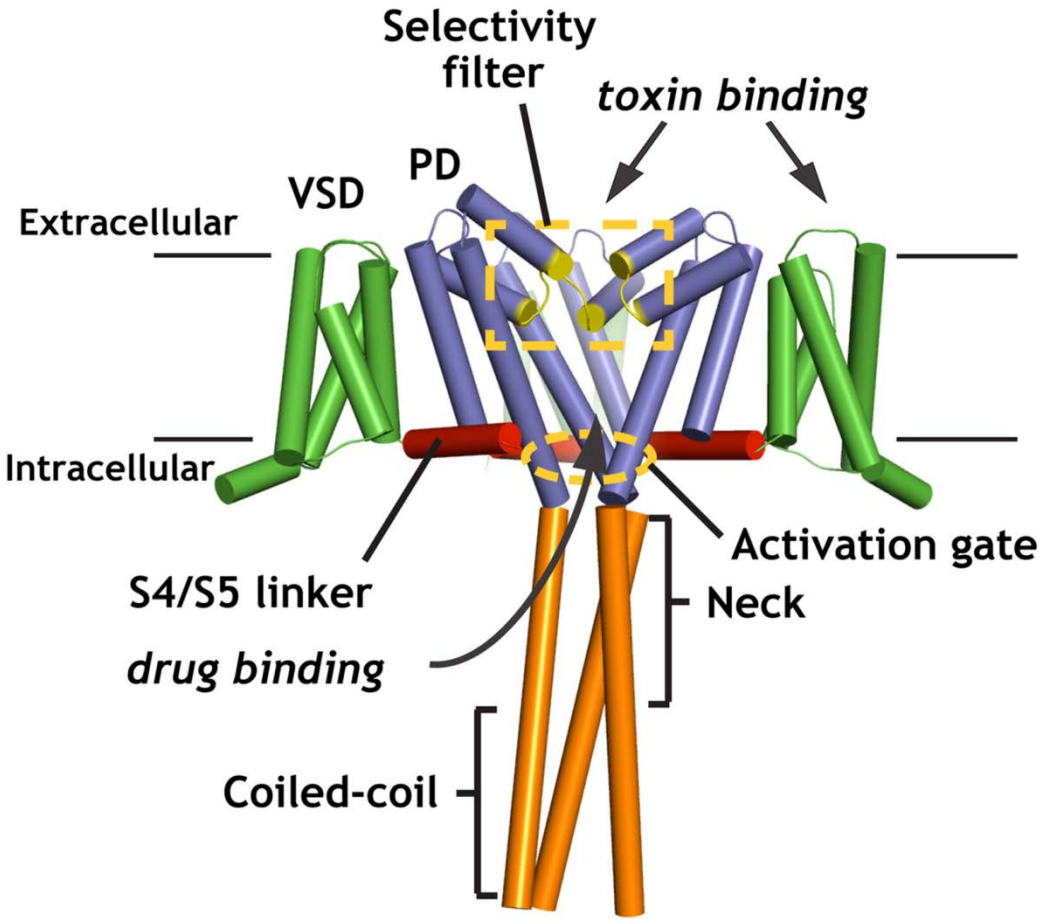

Figure 1.3 Structural assembly of bacterial voltage gated sodium channel (adopted from Payandeh and Minor Jr., 2015). Composite full-length $BacNa_V$ structure generated by aligning the Na_VAe1p structure containing the neck and coiled-coil region (PDB ID: 4LTO) onto the Na_VAb structure. (PDB ID: 3RVY)

The Nobel awarding research by the MacKinnon's lab in 1998 unveiled the first atomic structure of a bacterial (*Streptomyces lividans* (KcsA)) K^+ channel pore domain (Doyle et al., 1998). A decade later, several homotetrameric crystal structures of bacterial sodium channels of the NaChBac orthologue were successfully resolved (Payandeh et al., 2011, 2012; Zhang et al., 2012; McCusker et al., 2012; Shaya et al., 2014; Tang et al., 2014). Similar to potassium channels, $BacNa_V$ structures consist of four identical membrane-spanning repeats, each containing six transmembrane (TM) helices. Helices S1 to S4 form the voltage-sensing module, which is mainly responsible for sensing the voltage change across

the membrane and providing energetic initiation for the opening of the pore gate. Helices S5, P1 segments, the selectivity filter (SF) region, P2 segments and S6 helices form the pore module; it regulates selective sodium influx via systematic gating and inactivation mechanisms and provides interaction sites for channel blockers. Besides that, the cytoplasmic C-terminal domain (CTD) that follows the pore-lining S6 transmembrane helices has two parts: a membrane proximal charged region termed the "neck" and a unique "coiled-coil" region for $BacNa_Vs$ (**Figure 1.3**) (Tsai et al., 2013; Bagnéris et al., 2013; Shaya et al., 2014).

Despite the large evolutionary distance from vertebrate channels, $BacNa_Vs$, bearing simpler scaffolds, share many important features associated with their eukaryotic counterparts and thus have become important models for investigating the structural basis underlying mammalian Na_Vs and Ca_Vs. The following chapters review the progresses of studies on channel gating and inactivation, drug modulation as well as sodium conductance and selectivity mechanism with relevant structural and dynamic evidence respectively.

1.2 Gating and inactivation mechanisms of Na_Vs

Similar to the gating mechanism of voltage-gated potassium channels, upon depolarization, the conserved positively charged S4 TM helix of the VSD, moves toward the extracellular surface. This motion is proposed to further open the pore domain via the S4-S5 linker. Full length $BacNa_V$ structures (Payandeh et al., 2011, 2012; Zhang et al., 2012) have shown direct evidences that the VSDs remain in activated positions during long time exposure to a depolarizing potential (0 mV).

The activated state is rapidly terminated by fast-inactivation in vertebrate Na_Vs. The channel pore gate becomes impermeable mediated by four residues (IFMT motif) in the linker between repeats III and IV of the channel (West et al., 1992). When the membrane is depolarized, this motif is assumed to bind to the residues on repeats III and IV, acting as a

hinged lid to occlude the intracellular side of the channel precluding sodium ion transitions through the channel.

1.2.1 Characteristics of slow inactivation

Slow inactivation of Na_Vs regulates neuron and myocyte excitability by reducing availability of inward currents. In neurons, it is associated with the memory of previous excitation; in skeletal muscles, it ensures the normal contraction of myocytes when the K^+ concentration is elevated. In stark contrast to fast inactivation, extensively prolonged kinetics (several seconds to minutes) indicates the complexity and degeneracy of this mechanism. Therefore, it is unsurprising that multiple channel domains including both transmembrane domains and cytoplasmic loops have been implicated to be involved in this mechanism. (Silva, 2014)

In the pore domain, mutagenesis studies on $Na_V1.4$ have demonstrated that the residues with regard to slow inactivation, reside in the vicinity of the selectivity filter (SF), extracellular facing side (P-loops between S5 and S6 segments) and intracellular interface (S4-S5 linker) between cytoplasm and membrane (Silva, 2014). Moreover, negative charged residues in the SF, which are believed to provide selectivity and attraction to Na^+ ions, have been shown inaccessible during slow-inactivation (Xiong et al., 2003). Interestingly, removal of fast inactivation enhanced the slow-inactivation in both skeletal muscles (Featherstone et al., 1996) and cardiac isoforms of Na_Vs (Richmond et al., 1998). The voltage sensor domain (Silva and Goldstein, 2013) and auxiliary β subunits also facilitate slow-inactivation (Vilin et al., 1999). In addition, a large number of therapeutic agents have been shown to target slow-inactivated states including anesthetics like lidocaine (Balser et al., 1996).

The first $BacNa_V$s atomic structure has been crystallized with a mutant (I217C), which is located at the pore gate, stabilizing the crystal. While the VSD is activated, the pore gate is captured closed, thus this structure is considered to be in a “pre-open” state. Later, the crystal structure of wild

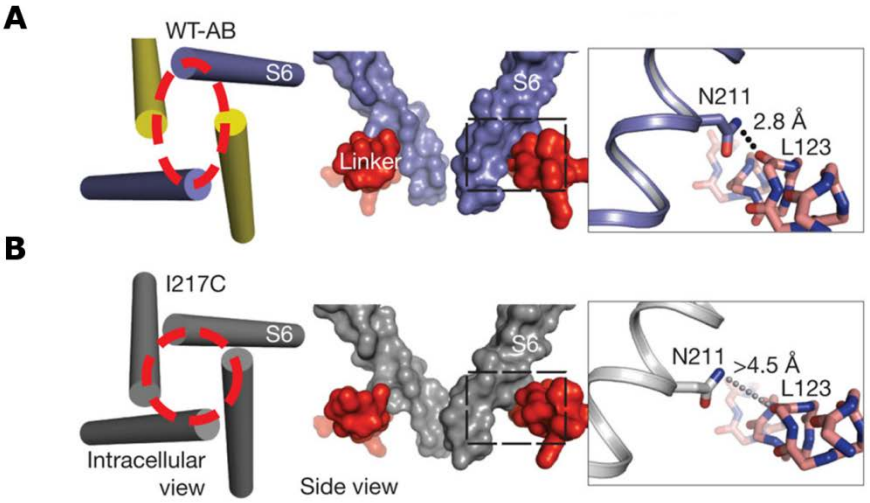

Figure 1.4 The comparison between the gate conformations of Na_VAb structures, (adopted from Payandeh et al., 2012). A. "slow-inactivated" gate structure (PDB: 4EKW), the inter-subunit hydrogen bond is formed between N211 side chain and S4-S5 linker backbone carbonyl atoms with a distance of 2.8 Å; **B.** "pre-open" gate structure (PDB: 3RVY) the inter-subunit hydrogen bond is unlikely to form between N211 and S4-S5 linker according to the distance measurement.

type Na_VAb has been resolved in a putative inactivated state; in marked contrast to the previously "pre-open" structure, the pore gate is arranged in a two-fold symmetry and non-conductive (**Figure 1.4**). Two S6 segments from diagonally opposed subunits have moved closer to the central pore axis, while the adjacent S6 segments have slide farther away, collapsing the S6 activation gate. This conformation is facilitated by two opposite inter-subunit hydrogen bonds involving the side chain of Asn211 in S6 and a backbone carbonyl in the S4-S5 linker according to electron density data (**Figure 1.4A**). Asn211 is the only universally conserved S6 residue in all Na_V channels. Mutations of the equivalent Asn residue in domains I and III of vertebrate Na_V channels, but not in domains II and IV, displayed dramatic effects on slow-inactivation (Wang and Wang, 1997). The validation of this finding with structural information pinpoints the pivotal role of this key residue in slow-inactivation, which may render channel assembly in a two-fold manner (Payandeh et al., 2012).

1.3 Small molecule modulations of Na_Vs

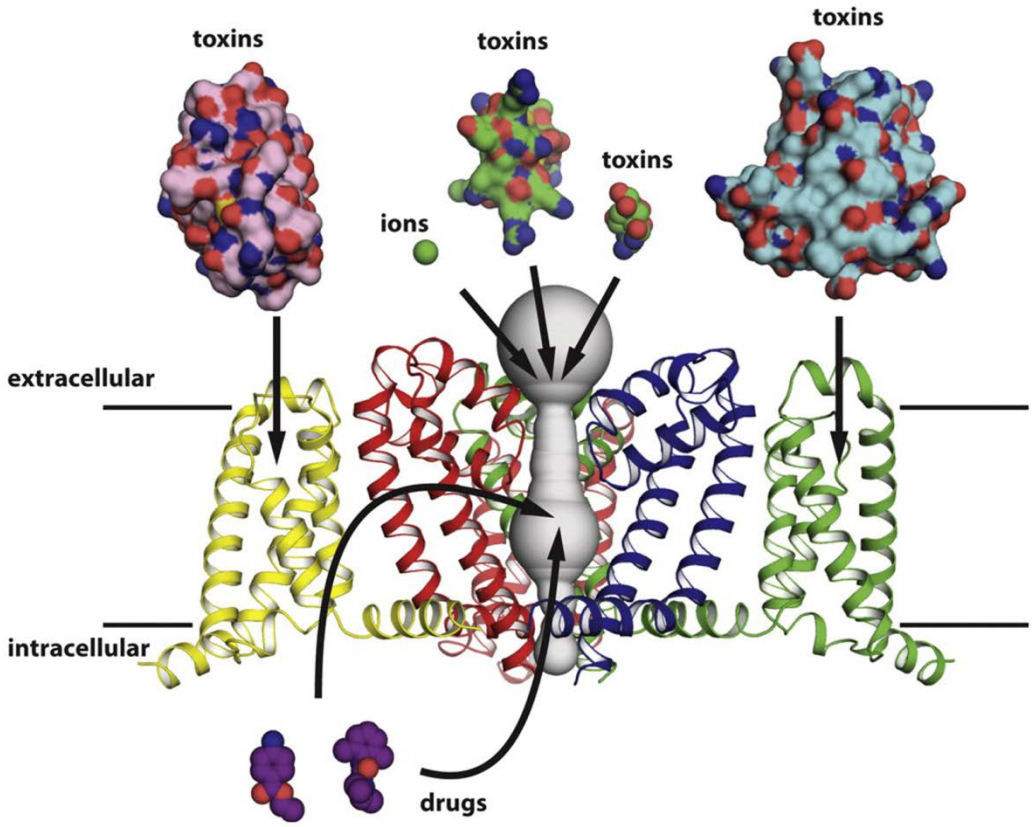

Figure 1.5 Mapping the binding sites of small molecules for eukaryotic Na_Vs to BacNa_Vs (Na_VAbs), (adopted from Payandeh and Minor Jr., 2015). Subunits are colored to represent the four non-homologous domains of eukaryotic Na_V channels. One pore domain and one voltage sensor are removed for clarity.

In line with the complex assortment of functional states of voltage-gated ion channels, molecules that affect Na_V functions have complex modes of action including pore block, open state stabilization of the pore and voltage sensor movement alteration to name a few (Payandeh and Minor Jr., 2015) (**Figure 1.5**).

1.3.1 Toxins

Given the pivotal role in cellular, especially neuronal excitability, Na_Vs become extremely vulnerable to toxic metabolites produced by venomous animals and poisonous plants.

Toxins utilize two distinct mechanisms. Pore-blocking toxins inhibit the flow of Na^+ ions by binding to the outer vestibule, such as non-peptidic

tetrotoxin (TTX) and saxitoxin and larger peptide toxins μ-conotoxin (μ-CTX). These outer vestibule blockers interact with Na_Vs with high affinities and specificities, which render them useful biophysical tools for electrophysiology studies in terms of probing the structure of the extracellular surface of Na_Vs (Goldschen-Ohm and Chanda, 2014).

In addition, gating-modifying toxins alter the gating mechanism by interacting with a region pertain to channel gating. For example, these toxins are able to pinch the voltage sensor in a particular state (Gilchrist et al., 2014), such as α- and β- scorpion toxins, enabling detailed insights into the movement of this domain (Catterall et al., 2007).

TTX is specifically binding to the DEKA motif of vertebrate Na_Vs' SF, and therefore non-sensitive to BacNa_Vs, whereas μ-conotoxin has been shown to actively interact with the conserved residues of the outer vestibule in both eukaryotic and prokaryotic Na_Vs (Chen and Chung, 2012; Korkosh et al., 2014).

1.3.2 Local anesthetics and their access pathways

Traditional Na_V channel pore blockers (also named "local anesthetics"), which reduce sodium influx during membrane depolarization, are used clinically as antiepileptic, antiarrhythmic, and analgesic drugs. These molecules are organic cations with *p*Ka values in the physiological range; thus, have both charged and neutral forms and block Na_Vs' central cavity in at least two ways (Corry et al., 2014).

It is widely accepted that the uncharged form causes channel blockade through a hydrophobic pathway defined by the membrane core and/or a proteinaceous access route when the channels are in the resting state (Hille, 1977a; b). This blockade is called "resting-state" block or "tonic" block. The affinity of this block is relatively low in the micromolar to millimolar range.

After penetration through the membrane, these compounds are protonated. They will reach their binding site located in the intracellular vestibule via the open gate region when the channel is activated. The affinity of this blockade is normally positively correlated with channel activation, therefore named “use-dependent” block (Hille, 2001).

Despite different affinities and passages, “tonic” and “use-dependent” blockers share similar binding sites, which are located in the central cavity; more specifically, in the inner vestibule of the channel aligned by pore lining residues at the lower part of the S6 segment. However, different residues in this region have been shown to contribute to “tonic” or “use-dependent” block respectively, reflecting changes in the central cavity associated with different gating states (resting, activated, inactivated) (Ragsdale et al., 1996; Li et al., 1999).

In addition, quaternary amine local anesthetics, which bear permanent charges, such as QX-314 and QX-222, are membrane-impermeable and have to enter the channel via the inner pore (Strichartz, 1973; Frazier et al., 1970). However, in several mutant Na_Vs, external access pathways (EAPs) for permanently charged local anesthetic drugs have been found (Ragsdale et al., 1994; Sunami et al., 1997).

1.3.3 Pharmacological and structural insights into local anesthetics interactions with BacNa$_V$s

BacNa$_V$s are sensitive to local anesthetics. Electrophysiological experiments demonstrated that extracellular applications of lidocaine and benzocaine (neutral) block NachBac and enhance channel inactivation (Lee et al., 2012). This indicates the existence of binding sites in BacNa$_V$s similar to eukaryotic Na$_V$s as well as a resembling hydrophobic access pathway for tonic inhibition (**Figure 1.6A**). This pathway is assumed to go through a so-called “sidewalk” or “fenestration” (Tikhonov and Zhorov, 2005; Tikhonov et al., 2006). This pathway has been found as a lateral opening window, gated by a conserved phenylalainin (F203 in Na$_V$Ab) in

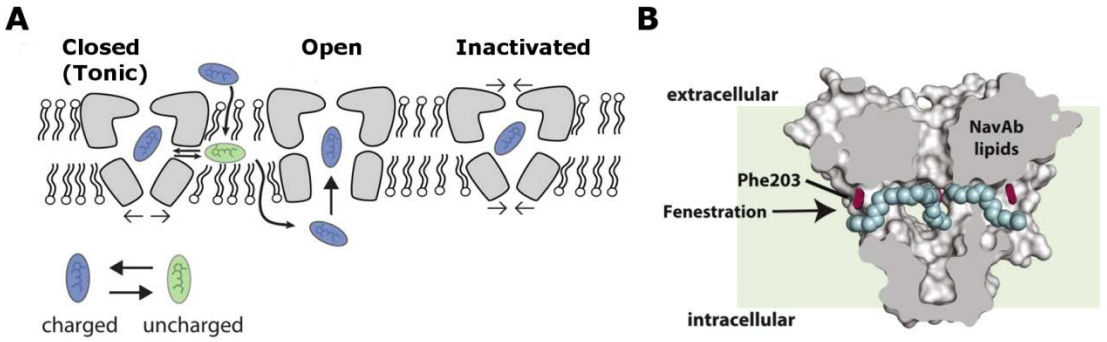

Figure 1.6 The access pathways in BacNa$_V$s for local anesthetics. A. demonstrates the open (hydrophilic) and tonic access pathways indicated by experiments with NaChBac, **(adopted from Lee et al., 2012)**; **B.** suggests the existence of the fenestration pathway for tonic inhibition of local anesthetics in bacterial Na$_V$s pore domain structure **(adopted from Payandeh and Minor Jr., 2015)**.

the hydrophobic sides of the pore domain in several crystal structures of BacNa$_V$s (Payandeh et al., 2011; Zhang et al., 2012; McCusker et al., 2012) (**Figure 1.6B**). In addition, the charged molecule, QX-314, failed to block the channel, indicating that the fenestration pathway is not accessible for quaternary amine local anesthetics in wild type BacNa$_V$s (Lee et al., 2012).

Nevertheless, residues involved in drug block are poorly conserved in BacNa$_V$s compared to eukaryotic Na$_V$s. Moreover, lidocaine has been shown to polymodally block different types of channels, such as K_{ATP}, K2P, K_V, Ca$_V$s, hERG as well as nicotinic acetylcholine and GABA receptors (Corry et al., 2014). Systematic mutagenesis studies are needed to further address structural determinants of BacNa$_V$s.

The success of co-crystallized BacNa$_V$s with brominated antagonists PI1, which also block human Na$_V$1.1, sheds lights on the interactions between drug molecules and the central cavity in atomic detail (Bagnéris et al., 2014). This finding suggests BacNa$_V$s can serve as a valuable tool for interpreting the mode of action of drugs in human Na$_V$s, and even screening and rationally designing drugs.

1.4 Mechanisms of conduction and selectivity

Generations of scientists have been fascinated by the question how different ion channels permeating specific types of ions through the pore at diffusion rates, while disfavoring other ions. Ca^{2+} and Na^{+} ions have nearly identical pauling radii (0.99 Å vs 0.95 Å), whereas Ca_Vs can choose Ca^{2+} over Na^{+} at a ratio of 1000:1 (Sather and McCleskey, 2003). K^{+} and Na^{+} share the same amount of positive charge (+1) (Sather and McCleskey, 2003); the permeability ratio, $P_K/P_{Na,}$ in Na_Vs in myelinated nerve is 1:12. (Hille, 1972)

1.4.1 Structural information of the SF in BacNa_Vs

More and more structural studies have confirmed that mammalian potassium and bacterial sodium channels share similar architectures in their pore domains (Long, 2005; Payandeh et al., 2011; Zhang et al., 2012; McCusker et al., 2012; Shaya et al., 2014). In bacterial sodium channels, four identical S5 and S6 helical repeats, bundle crossed on the same level of intracellular gate, outline the pore domain as “inverted-tepee”. From the extracellular side, the pore exhibits an outer funnel-like vestibule. In

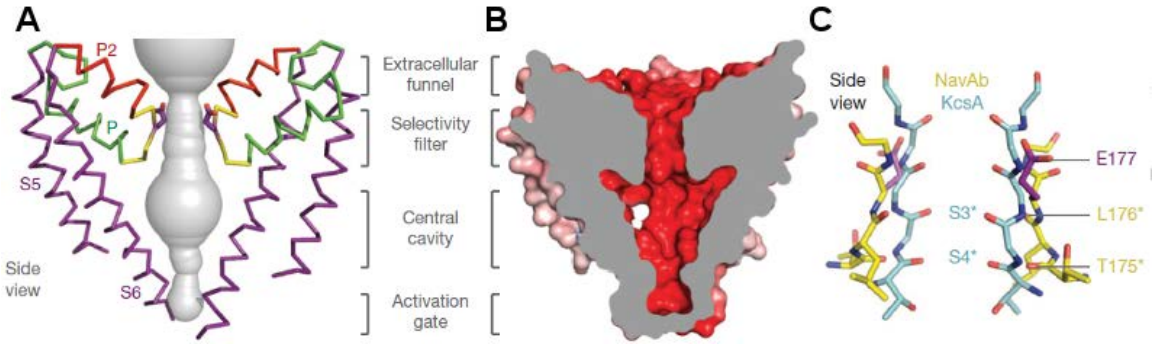

Figure 1.7 The selectivity filter of bacterial sodium channel Na_VAb (modified from Payandeh et al., 2011), two opposite subunits were shown for clarity. (A) Side view of pore domain with sticks representation, pore volume shown in grey; (B) Electrostatic potential colored from -10 to 10 kT (red to blue); (C) The comparison of the SFs between channels KcsA and Na_VAb.

the middle of the funnel, the ascending residues TLESW (in most homologues) form a tight turn preceded by the P1 helix and followed by the P2 helix (**Figure 1.7A**). These two conserved helices uphold this re-

entrant turn with hydrogen bond networks exposing backbone carbonyls of threonine (T175 in Na_VAb, **Figure 1.7C**) and Leucine (L176 in Na_VAb, **Figure 1.7C**) and side-chain carboxyls of glutamic acid (E177 in Na_VAb, **Figure 1.7C**) to the aqueous environment. This configuration lines a narrow lumen, the selectivity filter, connecting the extracellular funnel; a water-filled inner central cavity and the activation gate (**Figure 1.7B**).

1.4.2 Conduction and selectivity mechanisms in K_Vs

The conduction mechanisms of K^+ ions and selectivity between K^+ and Na^+ have been step-wisely addressed (Doyle et al., 1998; Aqvist and Luzhkov, 2000; Bernèche and Roux, 2001; Khalili-Araghi et al., 2006; Jensen et al., 2010).

Five ion-binding sites of the SF in potassium channels are aligned by backbone carbonyl oxygens of sequence TVGF(Y)G (Morais-Cabral et al., 2001) (**Figure 1.8A**). K^+ ions are encompassed by two neighboring carbonyl oxygens of four repeats located at eight vertices of each binding site. This configuration is energetically favorable to coordinate the interacting potassium ion by substituting water molecules from its first hydration shell (Gouaux and MacKinnon, 2005). During conduction, dehydrated potassium ions are sandwiched and knocked on by water molecules residing at adjacent binding sites in a single-ion profile (Morais-Cabral et al., 2001; Aqvist and Luzhkov, 2000) (**Figure 1.8C**). This picture has recently been challenged by Köpfer et al, where MD simulations and re-refinement of the crystal structures indicating the ion conductance might be facilitated by a direct Coulomb repulsion (Köpfer et al., 2014). Further electrophysiological experiments are needed to validate this finding (Hummer, 2014).

Consistent with inherent differences of physicochemical properties between K^+ and Na^+ ions, the architecture of the SF provides preferable K^+ selectivity over Na^+ and other cations (Thomas et al., 2011). Moderate dipole moment of carbonyl oxygens (~0.56), which act as coordination

ligands, as well as the right coordination number (8) of ligands and ideal ion-ligand distances (~2.7 Å) are optimally tuned for K^+ selectivity. Besides that, the thermal fluctuations of the coordination ligands may also play a role (Noskov et al., 2004). For details of K^+ ions conduction and selectivity over Na^+, please refer to the review by Furini and Domene (Furini and Domene, 2013).

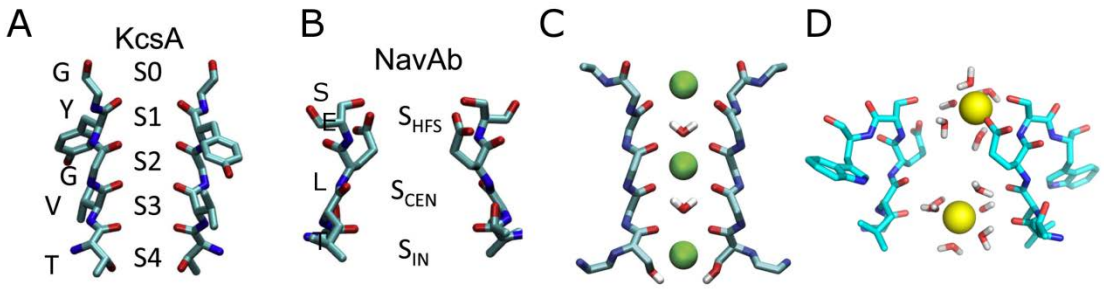

Figure 1.8 The comparison between sodium and potassium channel selectivity filter, two opposite subunits were shown for clarity. A & B. The SF site annotations and the sequences of KcsA and Na_VAb, **(modified from Furini and Domene, 2013)**; **C.** Potassium ion coordination in potassium channel SF, **(modified from Treptow and Tarek, 2006)**; **D.**Sodium ion coordination in sodium channel SF, **(modified from Ke et al, 2013)**.

1.4.3 Na^+ conduction in bacterial Na_Vs

Although the overall pore architecture of sodium and potassium channels are similar, the SF of $BacNa_Vs$ is wider and shorter than that of potassium channels (**Figure 1.7C**) with completely different sequence encoding (TLESW).

Analysis of the sodium channel pore radius indicates that a partially hydrated Na^+ ion can be accommodated at the high-field-strength (S_{HFS}) site (termed EEEE locus). One glutamic acid (E177 in Na_VAb) side chain coordinates with the sodium ion directly and neighboring glutamic acid side chains act as hydrogen bond acceptors for two in-plane water molecules. This coordination pattern renders sodium binding at this site asymmetric with respect to the pore axis. Move inwardly, the electron densities indicate four well-bound water molecules, which bridge the centrally coordinated ion with carbonyl oxygens of Threonine (S_{IN}) and

Leucine (S_{CEN}) in a fully hydrated manner (**Figure 1.8 B & D**) (Payandeh et al., 2011).

Molecular dynamics simulations (Carnevale et al., 2011) and free energy calculations (potential of mean force, PMF) (Corry and Thomas, 2011; Furini and Domene, 2012; Qiu et al., 2012; Stock et al., 2013) consensually support the interpretations from these structural studies and further provide detailed energetic insights into the sodium conduction mechanism. Na^+ ions experience no large energy barriers in the SF with optimal bi-pyramid coordination (6) of oxygen ligands. They are contributed either by water molecules from the first hydration shell of the Na^+ ion or carboxyl oxygen atoms from EEEE locus. A loosely coupled knock-on mechanism, which involves a second Na^+ ion approaching the SF, will further lower the free energy profile of the conduction to aid the diffusion of the first ion into the cavity by Coulombic repulsion (Corry and Thomas, 2011; Furini and Domene, 2012).

1.4.4 Selectivity between Na^+ and K^+ in BacNa$_V$s

Electrophysiological data for Na_VAb has shown the preference for Na^+ over K^+ is 8:1 (Payandeh et al., 2011). The key region for Na^+ and K^+ discrimination is between sites S_{HFS} and S_{CEN} suggested by free energy calculations. Compared to Na^+, K^+ ions fail to maintain an optimal geometry at this narrower region when coordinating with surrounding water molecules. Therefore, the free energy barrier at this region increases about 2~3 kcal/mol for K^+ conduction (Corry and Thomas, 2011; Furini and Domene, 2012).

1.4.5 Hypothetical mechanism of selectivity between Ca^{2+} and Na^+ in eukaryotic and prokaryotic Na$_V$s and Ca$_V$s

As discussed in chapter 1.1.3, the SF of many bacterial sodium channels contains four highly conserved glutamates (EEEE locus), which is more reminiscent of calcium channels than mammalian sodium channels,

encoded by the so-called DEKA ring (Heinemann et al., 1992; Yang et al., 1993; Sather and McCleskey, 2003; Ren, 2011).

As described before, eukaryotic Ca_Vs can choose Ca^{2+} over Na^+ at a ratio of 1000:1 (Sather and McCleskey, 2003), whereas the permeability ratio difference measured in a BacNa_Vs analogue is less prominent about $P_{Na}:P_{Ca}$ ~ 7~15 (Shaya et al., 2011). Key mutations, which introduce more negative charges in the SF of eukaryotic Na_Vs, render the sodium selective pore Ca^{2+} favorable (Heinemann et al., 1992; Yue et al., 2002; Shaya et al., 2011). Additionally, the anomalous mole fraction effect in Ca^{2+} selective channels is rather prevalent; there is substantial Na^+ current in Ca_Vs when the Ca^{2+} concentration is as low as 10 μM and the Ca^{2+} current will accentuate significantly to block Na^+ permeation when the Ca^{2+} concentration is increased (Yue et al., 2002). These observations suggest a delicate mechanism in terms of Na^+ and Ca^{2+} discrimination.

Prior to the availability of atomic structural information, theoretical models revealed different electrostatic interactions with the negative charges in the SF between Ca^{2+} and Na^+ (Corry et al., 2001); Ca^{2+} prevails in the competition to occupy site S_{HFS}, which abolishes the possibilities for the entry of other ions at the equivalent position (Hess and Tsien, 1984).

2 Aims

This thesis focuses on understanding the mechanism of ion conduction, selectivity and probes an engineered access pathway for charged molecules in bacterial and mammalian Na_V channels, respectively. Three publications are presented in chapter 4, which are relevant to these topics in understanding the detailed properties of the selectivity filter.

2.1 Distinct interactions of Na^+ and Ca^{2+} ions with the selectivity filter of the bacterial sodium channel Na_VAb (Chapter 4.1, (Ke et al., 2013))

How Na_V channels distinguish between sodium and calcium is assumed to involve subtle mechanisms as discussed in chapter 1.4.5. In this paper (Chapter 4.1), we compared spontaneous diffusions between sodium and calcium ions into the SF of the Na_VAb sodium channel (Payandeh et al., 2011) from equilibrium simulations. One-dimensional free energy profiles (PMF) have been calculated by umbrella sampling (described below in chapter 3.6.2) for both sodium and calcium ions. The energetic discrepancies between these two ion species are illustrated and discussed. This paper provides insights about different mechanisms between Na^+ and Ca^{2+} ions traversing the Na_VAb SF.

2.2 Different Inward and Outward Conduction Mechanisms in Na_VMs Suggested by Molecular Dynamics Simulations (Chapter 4.2, (Ke et al., 2014))

At the same time of our first study, scientific questions regarding the selectivity and conduction in the SF of $BacNa_Vs$ were extensively addressed including the mechanism of Na^+ coordination and the energetics in the SF (Carnevale et al., 2011; Corry and Thomas, 2011; Qiu et al., 2012; Furini and Domene, 2012), selectivities of Na^+ vs. K^+ (Corry and

Thomas, 2011; Furini and Domene, 2012; Qiu et al., 2012; Stock et al., 2013; Ulmschneider et al., 2013) and Na^+ vs. Ca^{2+} (Ke et al., 2013; Corry, 2013), ion conduction in open states of NachBac analogues by simulations with applied membrane potentials (Stock et al., 2013; Ulmschneider et al., 2013). However, the structural dynamics of the SF and the roles in ion conductance, channel gating and inactivation are still elusive. A simulation study illustrated the EEEE locus is quite dynamic (Chakrabarti et al., 2013). The side chains of the glutamic acid oscillated frequently between the outward facing and inward facing (dunking) conformations during equilibrium simulations. (Chakrabarti et al., 2013).

The pore-only $BacNa_Vs$ have been shown to reasonably reproduce the key electrophysiological properties, such as ion conductance and selectivity (Shaya et al., 2011; McCusker et al., 2012). MD simulations investigating these properties will benefit from these simplified, voltage-sensor free, structural architecture. Using a bacterial pore-only sodium channel structure resolved in the open conformation (McCusker et al., 2012), we conducted a MD study (Chapter 4.2) to further characterize the structural configurations of the EEEE locus with constant electrochemical drive by applying the CompEl method (described below in chapter 3.7). The dunked (flipped) configuration of the EEEE locus has been shown to exist only during ion outward conduction. Evidences from equilibrium simulations suggest that this structural configuration might lead to the kink of the lower part of the S6 segment, which renders channel non-conductive (Boiteux et al., 2014a). It indicates the flipping of the EEEE locus might serve as a first step in generating channel slow inactivation during depolarization.

2.3 Exploring the Structure of the Voltage-gated Na^+ Channel by an Engineered Drug Access Pathway to the Receptor Site for Local Anesthetics (Chapter 4.3, (Lukacs et al., 2014))

As introduced in Chapter 1.3, this paper (Chapter 4.3) aims to probe the potential external access pathway (EAPs) for charged local anesthetics (QX-222). A comparison of homology models based on different K^+ channel templates provides structural information of key determinant (I1575 in rNa_V1.4 channel) relevant to create this pathway (Lipkind and Fozzard, 2000; Tikhonov and Zhorov, 2005). Newer homology models based on bacterial sodium channel Na_VAb (Tikhonov and Zhorov, 2012) indicate that the W1531G mutant in the SF of rat Na_V1.4 channels, might additionally be involved in forming this pathway. To investigate this hypothesis, electrophysiology studies on selected mutants combined with molecular dynamics simulations, homology modeling and docking studies were performed.

3 Method (Theoretical Backgrounds)

3.1 Molecular Dynamics (MD) simulations

The states or dynamics of every system in the physical world are inevitably determined by their thermal motions at temperatures above absolute zero ($T > 0$ K). The branch of physics to study these thermal motions is thermodynamics. A single biomolecular system has numerous atoms to keep track of (~10^6 atoms) and meanwhile, is very small to see (~ 10^6 nm^3 in volume). In addition, a large number of key conformational changes or biological processes last several micro- or milli-seconds only, which are difficult to capture with experimental protocols. Molecular dynamics (MD) simulations utilize statistical mechanics to study the thermodynamics (predict the probability distributions of the thermal motions) of certain bio-molecular systems at the atomic level and subsequently to predict the kinetics of certain process within the bio-molecular system.

The thermodynamics of the system has been discovered to be determined by their quantum properties. The state-of-the-art solution with high accuracy and precision is based on the time-dependent Schroedinger equation. In this quantum mechanics (QM) scheme, the whole set of interactions of nuclei and electrons should be considered. Unfortunately, even the calculation for a set of several atoms at this ab-initio level is difficult to achieve using current computational power.

Alternatively, an extensively-used empirical way with lower precision is to employ molecular mechanics (MM) force field (i.e. AMBER (Cornell et al., 1995) in this thesis). In this method, the chemical properties of the electrons and nuclei are approximated at the atomic level. Interactions are parameterized as fixed values based on experimental or quantum mechanical calculations (**Figure 3.1**) which normally consist of bonded (bond, angle, dihedral (including improper dihedral)) and non-bonded terms (van-der-Waals interactions and Coulombic interactions). The overall potential energy of the system (V) is the summation of these additive terms as a function of atom positions. The neglect of tracking

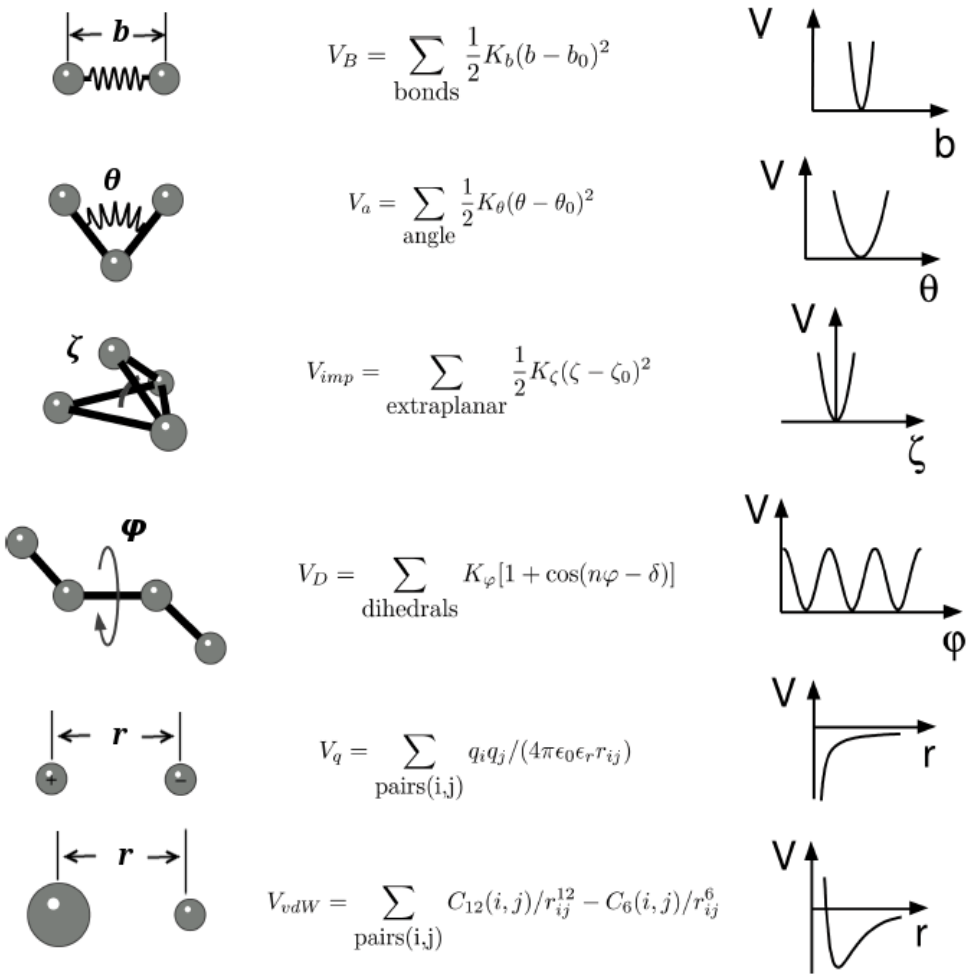

Figure 3.1. Overview of the different energy terms of a force field (modified from C. Kappel., 2011 PhD thesis, originated from Gunnar Schroeder).

electron motions gives rise to clear limitations that the classical MM simulations can only be adopted to study biological processes without chemical reactions (bond breaking and reforming); the lack of the description of polarizabilities of certain atom sets might influence the determination of free energy profiles in some biological processes. Despite that, in this thesis, MD simulations refer to MM simulations only. The program used in this thesis is GROMACS (Van Der Spoel et al., 2005; Hess et al., 2008).

When initiating the simulation ($t = t_0$), if velocities are not available, the program will randomly generate initial atomic velocities at a given absolute temperature T. The forces exerted on the particles are computed by the derivatives of the potential energies, which are calculated from the force field, with respect to the initial positions (r) at time t ($F(t) = dV/dr$)). Subsequently, the new velocities and coordinates are updated by numerically solving Newton's law of motion via certain algorithms after a discrete time step Δt. The default MD integrator in GROMACS is the leap-frog algorithm. Initially, it uses positions r at time t and velocities v at time $t - 1/2\,\Delta t$, then updates velocities (equation **1**) and positions (equation **2**) using the forces $\mathrm{F}(t)$, which are determined by the positions at time t.

$$v\left(t + \frac{1}{2}\Delta t\right) = v\left(t - \frac{1}{2}\Delta t\right) + \frac{\Delta t}{m}F(t) \tag{1}$$

$$r(t + \Delta t) = r(t) + \Delta t v\left(t + \frac{1}{2}\Delta t\right) \tag{2}$$

During simulations, periodic boundary conditions (PBC) are adopted to ensure the calculations of interactions, updates of velocities and

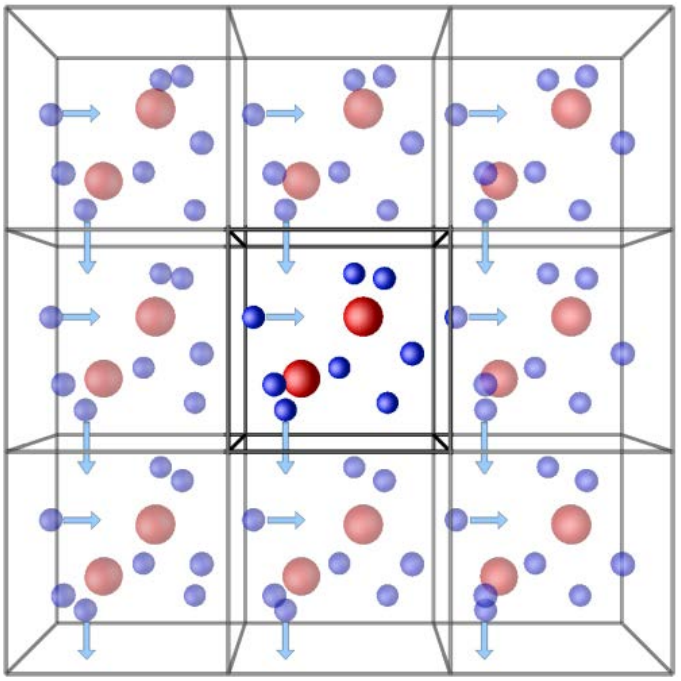

Figure 3.2 The schematic figure of periodic boundary conditions (adopted from http://isaacs.sourceforge.net/phys/pbc.html)

coordinates are continuous and subsequently avoid erroneously boundary artifacts. The simulation box is surrounded by a number of virtual copies of itself based on the box geometry (e.g. 8 copies will encompass a cubic simulation box as shown in **Figure 3.2**). This implementation enables the integrity and completeness as the simulation evolves. For example, as shown in **Figure 3.2**, if a particle leaves the box from the right hand side at time t_0, it will re-enter the simulation box from the left hand side at time $t_0 + \Delta t$ with all the interactions preserved and updated with all other particles located at the right hand side of the box.

In the simulated system, the largest available time step is limited by the high frequency and low amplitude bond stretching vibrations. After an unconstrained update from force field calculations of bond stretching vibrations with harmonic potentials, resetting bond length with holonomic constraints (i.e. LINCS in our studies (chapter 4)) (Hess et al.,

1997) are often considered a more faithful representation of the physical behavior of bond vibrations, which are almost exclusively in their vibrational ground state during MD simulations. Hereafter, the maximum time steps can be achieved as 2 fs. A further possible improvement is to remove the fastest degrees of freedom resulted from bond-angle vibrations with hydrogen atoms. Using virtual interaction sites and/or increasing the mass of the hydrogen atoms at the cost of the mass of the connected heavy atoms, will allow a minimum time step of about 4 fs with reasonable accuracy (Feenstra et al., 1999). This improvement is also adopted in our studies (chapter 4).

In classical mechanics, non-bonded interactions can be characterized as electrostatic and van der Waals (vdW) interactions. In simulations, they can be solved by summations of the two body Coulomb and Lennard-Jones (LJ) potentials respectively (**Figure 3.1**, V_q and V_{vdW}). The interactions between atom i and its first $(i+1)$ and second $(i+2)$ neighbors are excluded, because non-bonded repulsions (i.e. L-J potentials) are very strong when atoms are interacting with the first two neighbors. In addition, these interactions are already adequately modeled as bond and angle terms. For the third neighbors (1-4 interactions), both electrostatic and van der Waals interactions are calculated but scaled down by certain fudge factors varying from different force fields reproducing the correct torsion angles collectively with the dihedral potentials (proper and improper).

It is worth noting that these two calculations occupy more than 90% of the total calculation time and largely determine the free energy profile of certain biological processes of the simulations. Therefore, the accurate and efficient reproductions of these interactions are of crucial importance.

In Coulomb potential calculations, the charges distributed over each multi-atomic molecule are fixed as point partial charges, which are calculated as aforementioned, from experimental or quantum mechanical calculations. The total charge of each molecule is then summed up into

integers (elementary charges (e)). Since some electrostatic interactions cannot be neglected even at long distances, how to treat these interactions is crucial. A simple cut-off method, which neglects the long-range interactions at certain distances, leads to certain energy drifts of the system. The reaction-field method (Watts, 1974) is a good complementary to simplify long-range electrostatic interactions by assuming a constant dielectric environment beyond a cut-off $r_c$with a dielectric constant ε_{rf}. Alternatively, the particle mesh ewald (PME) method (Darden et al., 1993) is used to calculate long range electrostatic interactions beyond a cut-off, where the charges will be transformed into reciprocal space and mapped into a mesh. The cut-offs between direct space (short range calculations) and reciprocal space (long range calculations) can even be dynamically optimized to provide more efficient and accurate calculations of the Coulomb potentials by prompting the new module of Gromacs: g_tunepme (Kutzner et al., 2007) . By utilizing single instruction, multiple data (SIMD) compiling strategies of modern CPU or GPU nodes, the sampling of non-bonded interactions nowadays will be further enhanced.

The Lennard-Jones (LJ) potentials can decay very fast at remote distances. A plain cut-off at reasonable distances will introduce less energy drift during calculations. However, the LJ-PME method will offer even better sampling for lipid rich regions to reproduce better characteristics of the membrane (Wennberg et al., 2013).

In our studies (chapter 4), the vdW interactions were calculated with a cutoff of 10 Å and the long-range electrostatic interactions were calculated at 10 Å using the PME method.

3.2 Statistical ensembles in thermodynamics

For a given system, the specific microscopic state at certain time step is unpredictable. However, we can define a total statistical set in thermodynamics including every possible microscopic state of the system when certain macroscopic variables (such as temperature, volume, total

energy, etc) of the system are in statistical equilibrium (no net exchanges of these variables with the environment or sustained within the system with negligible fluctuations). After obtaining a statistically significant amount of observations, a probability distribution of each microscopic state of a given system can be delineated by certain partition functions (discussed in the following chapters **3.3** & **3.4**). Such a total set is termed statistical ensemble in thermodynamics.

According to different constraints, there are different types of ensembles as noted by Josiah Willard Gibbs, e.g. canonical ensemble, microcanonical ensemble and grand canonical ensemble (Frenkel and Smit, 2001). Here, only the canonical ensemble is briefly described.

A canonical ensemble (*NVT* ensemble) describes the system, which allows heat exchange with an infinitely large heat bath. Therefore, the absolute temperature (T) can be kept relatively fixed (isothermic). Besides, the volume (V) and total particle numbers (N) in the system should be constant.

3.3 Entropy

Entropy (S) is a macroscopic observable of the system, which indicates how the system can be arranged when it ergodically visited every possible microscopic state. In other words, how disordered the system (ensemble) is or how many microscopic states the system (ensemble) can potentially have when it is in equilibrium. Entropy is a state function and an extensive variable, therefore its changes are not relevant to the path of the process and time evolution, but it has additive property. The changes in entropy can be defined by Clausius equality $dS = dQ_{rev}/T$ for a thermodynamically reversible process, where Q_{rev} is the reversible heat transfer of the system at a given temperature (T).

In statistical mechanics, Boltzmann defines entropy as $S = k \cdot \log W$, which is more close to the definition of the entropy that it is the measure of arrangement of each possible information (microscopic state) of the

system. W can then be replaced by the summation of the probability of each microstate in which the system can occupy, and entropy can be defined as:

$$S = -k_B \sum_i P_i \ln P_i \tag{3}$$

Where P_i is the probability that the system occupies microstate i. P_i equals to n_i/N, where n_i is the occurrence of microscopic state i and N is the total number of observations. k_B denotes the Boltzmann's constant.

3.4 Partition function

In order to know all the information (as much as possible with finite observations) of a certain system, we have to estimate the entropy (equation (3)) of this system subject to two constraints. First, the sum of the probabilities of every microstate (i) equals to 1 (equation (4)); Second, the sum of the weighted energies ($P_i E_i$) of every microstate equals to the average total energy ($\langle E \rangle$: ensemble average of the total energy) of the system (equation (5)):

$$\sum_i P_i = 1 \tag{4}$$

$$\sum_i P_i E_i = \langle E \rangle \tag{5}$$

By introducing two Lagrange multipliers (α, β) into equations (4) and (5), the partition function can be solved. This paves the statistical path in correlating macroscopic observables with microscopic states. By definition, the partition function demonstrates how each microstate is partitioned among all possible microstates over the phase space when the

system is in thermal equilibrium. For a canonical ensemble, the partition function at given temperature is,

$$\mathrm{Z}_{\beta} = \sum_{i} e^{-\beta E_i} \tag{6}$$

Where one of the Lagrange multiplier β is the inverse temperature,

$$\beta = \frac{1}{k_B T} \tag{7}$$

The partition function can then be written as:

$$\mathrm{Z}_{T} = \sum_{i} e^{-E_i/k_B T} \tag{8}$$

$e^{-E_i/k_B T}$ is named as Boltzmann factor. It denotes the distribution (F_i) between any two microstates in the same ensemble depends on the energy differences of these two states at given temperature (T):

$$\frac{F_i}{F_j} \propto e^{(E_i - E_j)/k_B T} \tag{9}$$

In addition, the related properties in the system are,

$$P_i = \frac{1}{Z} e^{-E_i/k_B T} \tag{10}$$

$$\langle E \rangle = \sum_{i} P_i E_i = \frac{1}{Z} \sum_{i} E_i e^{-E_i/k_B T} = -\frac{\partial \ln Z}{\partial \beta} \tag{11}$$

$$S = -k_B \sum_i P_i \ln P_i = k_B(\ln Z + \beta\langle E\rangle) = \frac{\partial}{\partial T}(k_B T \ln Z) \quad (12)$$

The characteristic state function of the canonical ensemble is the Helmholtz free energy (A),

$$A = -k_B T \ln Z \quad (13)$$

Where A is the measure of maximum amount of useful (free) work, which can be extracted from the system when the temperature and the volume of the system are held at constant values.

3.5 *NpT* ensembles and Gibbs free energy

In wet labs, almost all experiments are carried out under constant temperatures and constant pressures. During MD simulations, in most cases, the system will be maintained complying with the same isothermal-isobaric constraints (*NpT* ensembles). Temperature can be maintained with coupling algorithms such as Berendsen (Berendsen et al., 1984), the velocity rescaling (Bussi et al., 2007) and Nosé-Hoover (Nose, S and Nose, 1984; Hoover, William G. and Hoover, 1985) algorithms. Pressure will be maintained by Berendsen and Parrinello-Rahman (Parrinello and Rahman, 1981) algorithms. In our simulations, the temperatures were maintained by the Nosé-Hoover thermostat and the pressures were kept constant by using the Parrinello-Rahman barostat (Chapter 4).

The partition function of *NpT* ensembles can be easily converted from the canonical ensemble weighted by the Boltzmann factor reflecting the work changes of the system resulting from volume changes at a given pressure. The characteristic state function of this ensemble is the Gibbs free energy (G),

$$G = -k_B T \ln Z\ (N, p, T) \tag{14}$$

The Gibbs free energy denotes the ability of the system to do the non-expansion work. In other words, how the system can evolve between two states of interest (initial and final) depends on the difference of Gibbs free energies between these two states when the system is in a thermal (metastable) equilibrium (or steady state).

3.6 Free energy calculations

In MD simulations, the calculation of free energy profile quantifies the capability of spontaneous occurrences of certain biological processes. It pinpoints the energetic mechanisms and provides direct evidence in interpreting the kinetics of these biological processes.

3.6.1 Challenges in computing free energy profiles

Theoretically, an equilibrium simulation will depict an accurate converged free energy profile of a certain process according to equation (14) when a simulation ergodically visits every possible microscopic state in a given ensemble. However, such sampling is trivial to reach in limited time scale. Rare events determining energy barriers may be inadequately sampled. In addition, during equilibration processes, the system will encounter large fluctuations resulting from the relaxation of non-optimal interactions among particles. These artifacts might generate irreversible unrealistic processes such as incorrect reaction pathways and structural changes.

Biophysicists are captivated by method development in need of enhancing the sampling to calculate free energy profiles for simulating systems of interest. The problem can be divided into two categories: I. The Potential of Mean Force (PMF) $W(\xi)$ along the reaction coordinate ξ, introduced by Kirkwood (Kirkwood, 1935); II. The free energy difference

between an initial state $(\lambda = 0)$ and a final state $(\lambda = 1)$ via several intermediate states with a set of coupling parameters $\{\lambda\}$. The gists of these two methods are consistent with the same "slow-growth (evolving)" concept. The first case can be solved via the umbrella sampling method (Torrie and Valleau, 1977), and the latter case can be tackled by direct thermodynamic integration with respect to λ, free energy perturbation (FEP) (Zwanzig, 1954), and Jarzynski's non-equilibrium method (Jarzynski, 1997).

Here, only the umbrella sampling method and its mathematical resolution, weighted histogram analysis method (WHAM) (Kumar et al., 1992) will be extensively described. Because this method has been

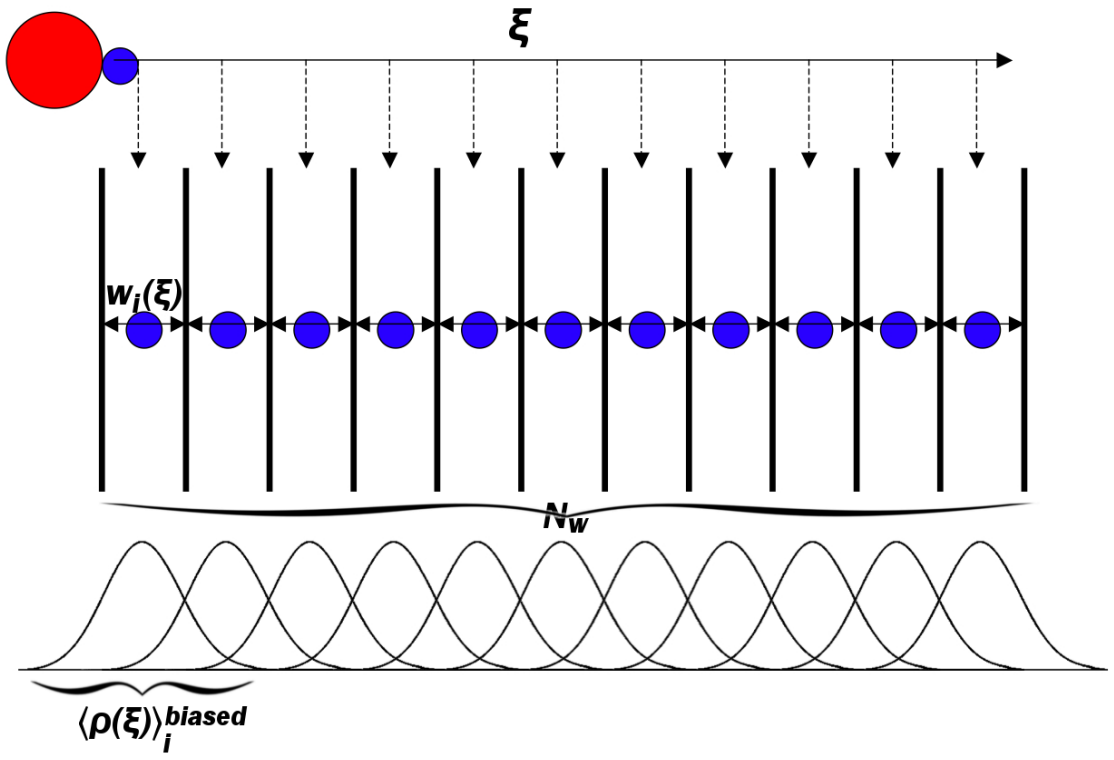

Figure 3.3 Schematic representation of umbrella sampling, (modified from Justin Lemkul's tutorial, http://www.bevanlab.biochem.vt.edu/Pages/Personal/justin/gmx-tutorials/umbrella/05_pull.html). Here the reaction coordinate ξ, the window potential $w_i(\xi)$, window number N_w and the biased distribution $\langle \rho(\xi) \rangle_i^{biased}$ are labelled.

adopted in one of the papers in this thesis (Chapter 4.1) when calculating the one-dimensional PMF to study the selectivity between Na^+ and Ca^{2+} in the SF of the bacterial sodium channel Na_VAb.

3.6.2 PMF and umbrella sampling

PMF $W(\xi)$ can be described as a comparison of the average distribution function $\langle\rho(\xi)\rangle$ to an arbitrarily chosen reference point $\langle\rho(\xi^*)\rangle$,

$$W(\xi) = W(\xi^*) - k_B T \ln\left[\frac{\langle\rho(\xi)\rangle}{\langle\rho(\xi^*)\rangle}\right] \tag{15}$$

As discussed before, it is impractical to calculate PMF or estimate $\langle\rho(\xi)\rangle$ along the whole path of a biological process from an equilibrium simulation. An alchemical technique, umbrella sampling (**Figure 3.3**), dissects the system into several individual simulations with N_w biased window potentials covering the whole reaction pathway. Using a spring constant k, each biasing umbrella window potential $w_i(\xi)$ (equation (16)) is applied to enhance the sampling in the vicinity of a chosen value ξ for ith window,

$$w_i(\xi) = -\frac{k}{2}(\xi - \xi_i)^2 \tag{16}$$

The unbiased PMF for the ith window is then,

$$W_i(\xi) = W(\xi^*) - k_B T \ln\left[\frac{\langle\rho(\xi)\rangle_i^{biased}}{\langle\rho(\xi^*)\rangle}\right] - w_i(\xi) + F_i \tag{17}$$

Where F_i is the free energy constant raised by the window potential $w_i(\xi)$,

$$e^{-F_i/k_BT} = \langle e^{-w_i(\xi)/k_BT} \rangle \tag{18}$$

3.6.3 Weighted histogram analysis method (WHAM) (Kumar et al., 1992)

The key to obtain PMF of the whole pathway is to recombine different umbrella simulations into the final estimate of $W(\xi)$. A mathmetical method, weighted histogram analysis method (WHAM) (Kumar et al., 1992) is applied. WHAM is carefully compared with previous methods to calculate PMF by umbrella sampling (Roux, 1995) and extensively discussed about its powerful application in MD simulations (Souaille and Roux, 2001). The total unbiased distribution function is the sum over ξ-dependent weighted unbiased distribution functions of each umbrella simulation,

$$\langle \rho(\xi) \rangle^{unbiased} = \sum_{i=1}^{N_w} p_i\,(\xi) \langle \rho(\xi) \rangle_i^{unbiased} \tag{19}$$

Where the unbiased distribution function $\langle \rho(\xi) \rangle_i^{unbiased}$ can then be represented by the biased distribution function weighted by the Boltzmann factor raised by umbrella (window) potential,

$$\langle \rho(\xi) \rangle_i^{unbiased} = e^{[w_i(\xi) - F_i]/k_BT} \langle \rho(\xi) \rangle_i^{biased} \tag{20}$$

$\langle \rho(\xi) \rangle_i^{biased}$ is straightforward to compute from each umbrella simulation. However, how the distribution function $\langle \rho(\xi) \rangle_i^{unbiased}$ for ith simulation partition into total distribution function $\langle \rho(\xi) \rangle^{unbiased}$, in other words, how to mathematically represent these weights $p_i(\xi)$ on the condition of the Boltzmann factor raised by umbrella potential, needs to be solved. Hereafter, the WHAM equations served as a straightforward

and computational available solution. The WHAM equations are derived from the minimization of statistical error in $\langle\rho(\xi)\rangle^{unbiased}$ estimation subject to $\sum_{i=1}^{N_w} p_i\,(\xi) = 1$ with Lagrange multipliers method. As a result,

$$\langle\rho(\xi)\rangle^{unbiased} = \sum_{i=1}^{N_w} \frac{n_i e^{-[w_i(\xi)-F_i]/k_BT}}{\sum_{i=1}^{N_w} n_i e^{-[w_i(\xi)-F_i]/k_BT}} \langle\rho(\xi)\rangle_i^{unbiased} \tag{21}$$

$$= \sum_{i=1}^{N_w} \frac{n_i}{\sum_{i=1}^{N_w} n_i e^{-[w_i(\xi)-F_i]/k_BT}} \langle\rho(\xi)\rangle_i^{biased} \tag{22}$$

$$e^{-F_i/k_BT} = \int d\xi \langle\rho(\xi)\rangle^{unbiased}\, e^{-w_i(\xi)/k_BT} \tag{23}$$

n_i denotes the data points in ith umbrella sampling. Equations (22) and (23) are WHAM equations. Equation (23) is determined from equation (18). Hereafter, the unknown variables F_i and $\langle\rho(\xi)\rangle^{unbiased}$ can be solved self-consistently (**Figure 3.4**) with these two WHAM equations. For N_w umbrella simulations, there are a set of constants $\{F_i^i\}$. The iteration begins with of a set of arbitrarily choosen $\{F_i^0\}$, then the estimation of $\langle\rho(\xi)\rangle^{unbiased}$is obtained from equation (22). The estimation of $\langle\rho(\xi)\rangle^{unbiased}$ is used on the right hand side of equation (23) to compute a new set of $\{F_i^1\}$. The iteration circle continues until convergence of the process ($\{F_i^i\}$ can give rise to optimal estimate to $\langle\rho(\xi)\rangle^{unbiased}$ and vice versa).

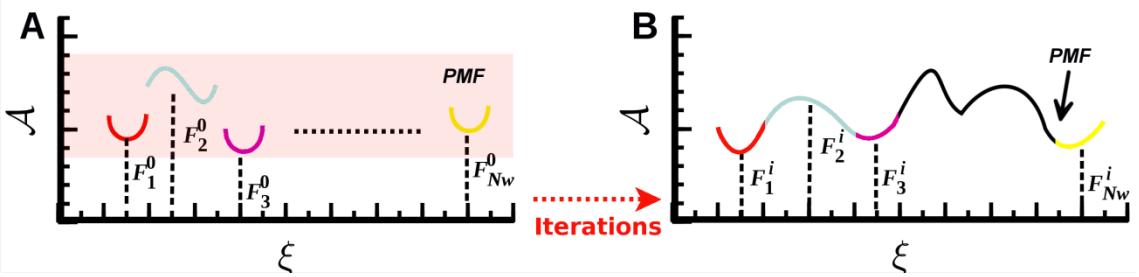

Figure 3.4 The schematic description of how PMF ($\langle\rho(\xi)\rangle^{unbiased}$) is derived by WHAM equations self-consistently.

In Gromacs, a free WHAM tool named after g_wham has been introduced (Hub et al., 2010), it estimates not only the PMF values and also provides several bootstrapping resampling strategies to estimate the errors of the calculated PMF values.

3.7 Simulations with transmembrane potential

The physiological functions of ion channels are dominated by transmembrane potentials. As introduced before (chapter **1.1.2 & 1.2**), variations of the membrane potentials during an action potential, due to unequal distributions of ion concentrations, initiate complicated structural changes correlating several ion channel states (closed, open, inactivated (fast and slow), deactivated) as well as transiently conducting ions (Hille, 2001). Therefore, it is of great importance to model transmembrane potentials, which resemble physiological scenarios or experimental conditions.

In practice, during simulations, how applied transmembrane potential (V_m) influences the local electrostatic potential across the membrane; what is the biophysical significance of a transmembrane potential has been studied and reviewed in detail by Benoit Roux (Roux, 1997, 2008). The potential energy of a thermal equilibrium system without an applied membrane potential is U_{total}. The intrinsic electrostatic interaction contributions of the total potential energy U_{elec} are calculated by summation of Coulomb interactions as described by the force filed

(**Figure 3.1**, V_q) or can be approximately represented by the potential solely generated from a reaction field U_{rf} when considering that the charge distribution of the system is roughly homogeneous. After applying the membrane potential (V), the total potential energy becomes $U_{total} = U + U_{mem}$, U_{mem} denoting the contributions resulted from the applied transmembrane potential. U_{mem} will further be divided into two parts:

$$U_{mem} = \frac{1}{2}CV^2 + Q_d V \tag{24}$$

C is the capacitance of the system, Q_d is the displacement charge (effective charge raised by applied potential V). Q_d is dependent on the charge movement coupled with a dimensionless function $\emptyset_{mp}(z)$ representing the fraction of the membrane potential at position z.

$$Q_d = \sum_i q_i \emptyset_{mp}(z_i) \tag{25}$$

$\emptyset_{mp}(z)$ is solved by a modified Poisson-Boltzmann (PB) theory (Roux, 2008) (**Figure 3.5B**). Although in reality, it is much more complicated, $\emptyset_{mp}(z)$ indicates, in a simplified representation, the fraction of the membrane thickness (Roux, 1997):

$$\emptyset_{mp}(z) = \frac{z_i + L_Z/2}{L_Z} \tag{26}$$

Therefore, $\emptyset_{mp}(z)$ is referred to "electric distance". **Figure 3.5C** illustrates how different applied electric fields influence the electrostatic potentials across the membrane.

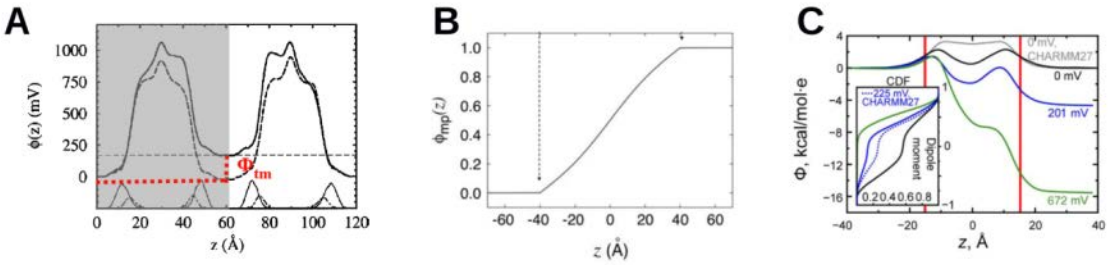

Figure 3.5 The characteristics of the electrostatic potential during simulations with applied membrane potential. A, illustrates the transmembrane potential changes from a simulation with 0mv applied potential (dashed) to a simulation with 170mv (solid) **(modified from Sachs et al.,2004)**, the single bilayer region which can be compared directly with Figure B and C is shaded with grey color; **B,** illustrates, ideally, the fraction of the membrane potential experienced by charge atoms along the simulation box has linear relationship with membrane (the length of the box along the z axis) **(adopted from Roux, 2008)**; **C,** demonstrates the resultant local electrostatic potential profile variations upon different magnitudes of transmembrane potentials **(adopted from Jensen et al., 2013).**

Following these ideas, two main methodologies have been introduced. First, a constant external electric field $\vec{E}$, is applied perpendicular to the membrane plane (Suenaga et al., 1998; Zhong et al., 1998; Tieleman et al., 2001; Crozier et al., 2001). In principle, this gives rise to an electromotive force potential (electric potential) $V = L_z \times \vec{E}$ (L_z denotes the simulations box length in the direction of $\vec{E}$), mimicking the testing potentials of patch clamping methods across the infinite planar bilayer with small fluctuation. However, the inevitable artifacts due to the periodic boundary conditions of the simulation box failed to render accurate transmembrane potentials as intended (Sachs et al., 2004; Delemotte et al., 2008). Later, a more physical setup according to charge imbalances across the membrane by applying a second bilayer has been proposed (Sachs et al., 2004). This method is able to simulate a realistic membrane potential. The 1-D time-averaged electrostatic potential $\emptyset(z)$, which reflects the combination effect of both intrinsic electrostatic interactions and applied membrane potential, can be numerically solved by double integration of the Possion equation with respect to equilibrium charge distributions at position z perpendicular to the membrane. This requires $\emptyset(0) = \emptyset(L) = 0$ as boundary conditions (Sachs et al., 2004). (**Figure 3.5A**).

$$\emptyset(z) = -\frac{1}{\varepsilon_0}\sum_i q_i\left[\int_0^z (z-u)\rho_i(u)\,du - \frac{z}{L}\int_0^L (L-u)\rho_i(u)du\right] \quad (27)$$

Where $\varepsilon_0$is the permittivity constant, q_i is the charge on atom i, $\rho_i$is the density of atom i, L is the box length along the z direction and u is a dummy variable which does not influence the result.

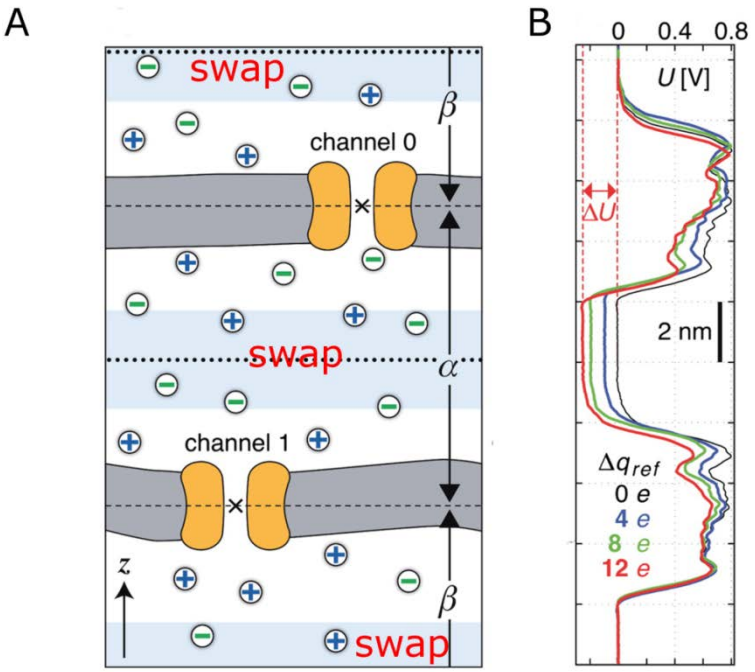

Figure 3.6 The representation of the computational electrophysiology scheme (double bilayer setup) (modified from Kutzner, et al., 2011). A. The schematic representation of this setup, the ion/water exchange region are labeled as "swap"; **B.** An exemplar electrostatic profile of the simulations with different charge imbalances, the transmembrane potentials are denoted as $\Delta \boldsymbol{U}$.

In 2011, a new simulation scheme based on the above described double bilayer setup in gromacs: Computational Electrophysiology (CompEL) was published (Kutzner et al., 2011) . This method is able to study ion conductance in ion channels or transporters. In this study, the charge imbalance across the double-membrane configuration, as used before (Sachs et al., 2004), generates an internal electric field. Moreover, Kutzner et al., developed a particle interchange method, which exchanges

ion/water pairs between buffer regions in both compartments to maintain a given concentration gradient and/or charge imbalance across two membranes (**Figure 3.6A**). Therefore, this scheme enables to achieve a constant electrochemical drive during simulations and generates configurations according to Boltzmann probability in line with a grand canonical ensemble (open equilibrium) as highlighted by Roux (Roux, 2008, 2011).

Ion conductance G for ion species i with charge q_i (as elementary charge e) in each interval Δt is calculated by:

$$G = \frac{\sum_i n_i q_i}{\Delta t \Delta U} \tag{28}$$

This method is utilized and discussed in the second paper of this thesis (Chapter **4.2**).

4 Results

4.1 Distinct interactions of Na^+ and Ca^{2+} ions with the selectivity filter of the bacterial sodium channel Na_VAb

Song Ke, Eva-Maria Zangerl, Anna Stary-Weinzinger

Biochemical and Biophysical Research Communications

430 (2013) 1272–1276

Biochemical and Biophysical Research Communications 430 (2013) 1272–1276

Contents lists available at SciVerse ScienceDirect

Biochemical and Biophysical Research Communications

journal homepage: www.elsevier.com/locate/ybbrc

Distinct interactions of Na^+ and Ca^{2+} ions with the selectivity filter of the bacterial sodium channel Na_VAb

Song Ke, Eva-Maria Zangerl, Anna Stary-Weinzinger *

Department of Pharmacology and Toxicology, University of Vienna, Althanstrasse 14, UZA 2, A-1090 Vienna, Austria

ARTICLE INFO

Article history:
Received 5 December 2012
Available online 19 December 2012

Keywords:
Bacterial sodium channel
Ca^{2+} selectivity
Free energy profile
Ion binding sites
Molecular dynamics simulation

ABSTRACT

Rapid and selective ion transport is essential for the generation and regulation of electrical signaling pathways in living organisms. In this study, we use molecular dynamics simulations and free energy calculations to investigate how the bacterial sodium channel Na_VAb (*Arcobacter butzleri*) differentiates between Na^+ and Ca^{2+} ions. Multiple nanosecond molecular dynamics simulations revealed distinct binding patterns for these two cations in the selectivity filter and suggested a high affinity calcium binding site formed by backbone atoms of residues Leu-176 and Thr-175 (S_{CEN}) in the sodium channel selectivity filter.

1. Introduction

Na^+ flux is vital for initiating action potentials in the membranes of most electrically excitable cells [1]. Recent homotetrameric crystal structures of bacterial Na_V channels [2–5] provide new possibilities for investigating the molecular basis of ion selectivity and transport in these channels. The mechanisms of how these channels discriminate between different ion types are poorly understood. Recent molecular dynamics investigations [6,7] provide insights into Na^+ versus K^+ selectivity; however Ca^{2+} discrimination was not analyzed in atomistic detail so far. In this study, we investigate how bacterial sodium channels discriminate between Na^+ and Ca^{2+}, a process essential for biological function.

Na_V channels are composed of four membrane spanning subunits, containing six helices per subunit. The pore module consists of helices S5, P1 segments, a selectivity filter (SF) region, P2 segments and S6 helices, lining the inner pore cavity. Remarkably, the SF of many bacterial sodium channels contains four highly conserved glutamates (EEEE locus), which is more reminiscent of calcium channels than mammalian sodium channels [8–11]. Despite this high sequence similarity, bacterial Na_V channels distinguish between sodium and calcium ions with permeability ratios P_{Ca}/P_{Na} of 0.08–0.15 [12,13]. The three dimensional architecture of this motif is revealed by X-ray structures of bacterial Na_V channels from three different species [2–5]. How these unusual sodium channels discriminate between different ion types and how ions permeate the pore are not well understood yet.

In this study, we performed molecular dynamics (MD) simulations and single ion potential of mean force (PMF) calculations to investigate Ca^{2+} interactions with the bacterial sodium channel Na_VAb.

2. Materials and methods

2.1. Molecular dynamics simulations

MD simulations were performed with Gromacs version 4.5.4 [14]. The coordinates of Na_VAb (PDB Entry: 3RVY; resolution: 2.7 Å) with a closed pore gate were used in all simulations [2]. Cysteine residues at position 217 were mutated back to isoleucine to obtain the wild-type structure of Na_VAb, and all charged residues were treated keeping their charge states at physiological pH 7.4. Simulations were carried out with the AMBER99sb [15] all atom force field in dioleoylphospathidylcholine (DOPC) lipids [16] with the TIP3P water model [17].

All covalent bonds were constrained using the LINCS algorithm [18], allowing for an integration time step of 2 fs. A 10 Å cutoff was adopted for calculating short-range electrostatic interactions and the Particle Mesh Ewald [19] summation was used for calculating long-range electrostatic interactions. The corrected Lennard-Jones parameters for the amber forcefield [20] were implemented in this

Abbreviations: Na_VAb, bacterial sodium channel (*Arcobacter butzleri*); Na_VRh, bacterial sodium channel (*Rickettsiales* sp. *HIMB114*); MD simulation, molecular dynamics simulation; PMF, potential of mean force; SF, selectivity filter; DOPC, dioleoylphospathidylcholine; PDB, protein data bank; RMSD, root-mean-square deviation.

* Corresponding author. Fax: +43 1 4277 9553.
E-mail addresses: song.ke@univie.ac.at (S. Ke), a0509032@unet.univie.ac.at (E.-M. Zangerl), anna.stary@univie.ac.at (A. Stary-Weinzinger).

0006-291X/$ - see front matter © 2012 Elsevier Inc. All rights reserved.
http://dx.doi.org/10.1016/j.bbrc.2012.12.055

study and the vdW interactions were calculated with a cutoff of 10 Å. The Nose–Hoover thermostat [21,22] and the semi-isotropic Parrinello-Rahman barostat algorithm [23] was used to maintain simulation temperature and pressure constantly at 310 K and 1 bar, respectively. Prior to MD simulations, 3000 conjugate gradient energy-minimization steps were performed, followed by 5 ns equilibration in order to fully solvate mobile water and lipids around a protein restrained with a force constant of 1000 kJ/mol/nm^2 on all heavy atoms.

2.2. PMF

One ion PMF calculations were performed by umbrella sampling [24]. Prior to this simulation, a test ion was pulled with a force constant of 2090 kJ/mol/nm^2 (5 kcal/mol/Å^2) along the filter, from a heavily restrained (force constant: 10,000 kJ/mol/nm^2) reference ion (placed ~15 Å away on top of the extracellular side of the filter) [25]. This procedure resulted in 20 windows to explore the ion conductance route along the filter (total length ~10 Å, as shown in Fig 1B inset) at 0.5 Å intervals. The test ion was initially held fixed for a 100 ps equilibration, followed by a 2 ns PMF simulations with the first 0.5 ns removed for equilibration [7]. In each umbrella sampling simulation, the probing ion was restrained harmonically with a force constant of 4180 kJ/mol/nm^2 (10 kcal/mol/Å^2) along the z-axis. A 4.18 kJ/mol/nm^2 (0.01 kcal/mol/Å^2) force constant was exerted on the Cα atoms of the protein as a center of mass restraint during simulations, except for the SF residues (residues 174–183) [7]. The free energy profile was calculated with the g_wham tool implemented in Gromacs. Error analysis was performed calculating 200 bootstrap iterations [26].

3. Results and discussions

Two 100 ns MD simulations with 100 mM NaCl and 100 mM $CaCl_2$ concentrations each were performed. A third simulation with either NaCl or $CaCl_2$ was extended to 150 ns for analysis. To get further insight into the different behavior of Na^+ and Ca^{2+} ions in the

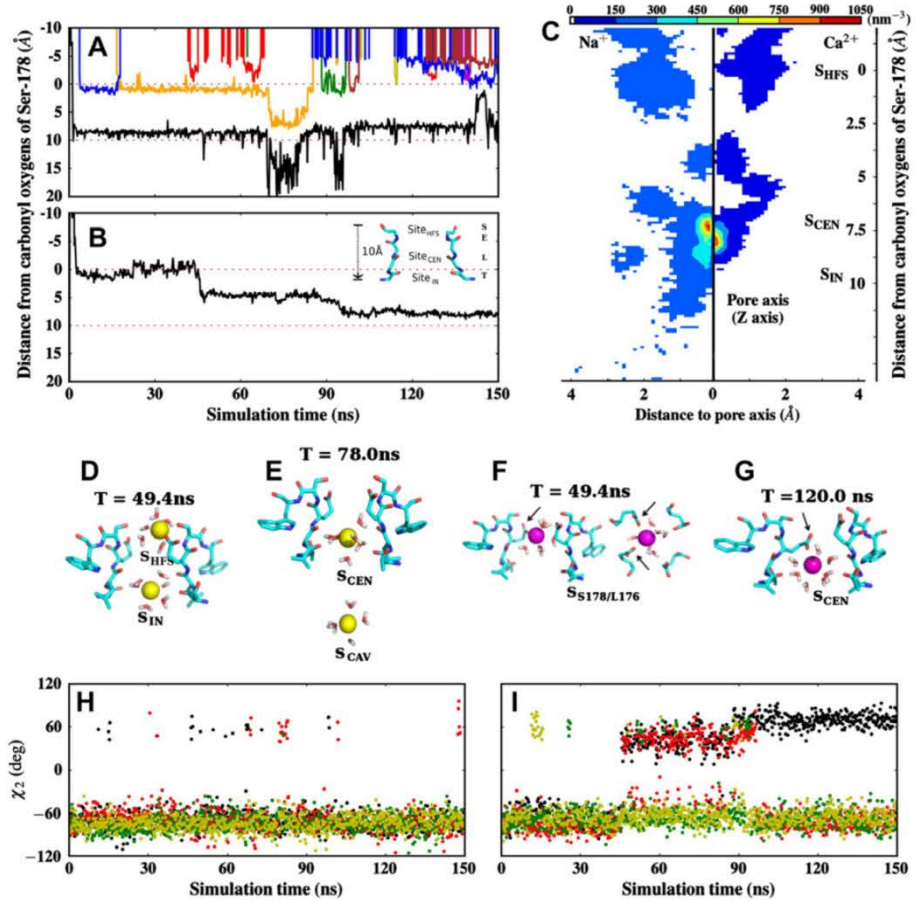

Fig. 1. Na^+ and Ca^{2+} binding patterns inside the Na_VAb SF. (A) Binding patterns of Na^+ ions as a function of time (snapshots from every 200 ps), the y-axis depicts the distances along the pore axis (z-axis) to the entrance of the SF (carbonyl oxygen atoms of Ser-178) from the extracellular solution; two red dotted lines highlight the entrance and the exit of the SF (backbone nitrogen atom of Thr-175); the inset shows the binding sites suggested by Payandeh et al. [2]. (B) Binding pattern of Ca^{2+} as a function of time (snapshots from every 200 ps). (C) Ion distribution maps of Na^+ s and Ca^{2+} inside the selectivity filter (snapshots from every 10 ps). (D) Filter snapshot of Na^+ ions at 49.4 ns; the Na^+ ions are shown as yellow spheres. (E) Filter snapshot depicting Na^+ ion positions at 78.0 ns. (F) Ca^{2+} snapshots (side and top view) taken at 49.4 ns, with Ca^{2+} shown in magenta; the black arrows indicate the side chain conformational change of Glu-177. (G) Filter snapshot taken at 120.0 ns. (H) Analysis of the χ_2 angle of Glu-177 as of function of time for NaCl (snapshots from every 200 ps); Side chains of the different subunits are colored black, red, yellow and green respectively. (I) Changes of Glu-177 χ_2 angles induced by Ca^{2+} binding as of function of time (snapshots from every 200 ps).

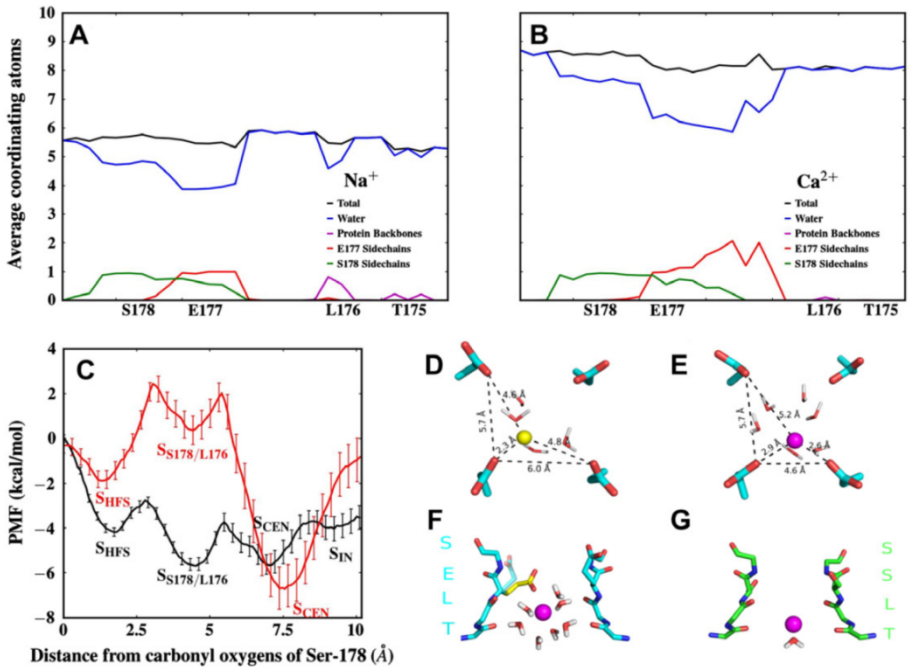

Fig. 2. Ion coordination and PMF comparison between Na^+ and Ca^{2+}. Oxygen atoms closer than 2.8 Å (Na^+) or 3.0 Å (Ca^{2+}) were considered coordinating atoms [35]. (A) Average oxygen coordination numbers for Na^+: the total coordination number is depicted in black; water oxygens are depicted as blue lines, protein backbone oxygens are shown in magenta, Glu-177 side chain are colored red and Ser-178 side chain are shown as green lines (windows of all umbrella-sampling runs were taken for analysis, taking snapshots every 15 ps). (B) Average coordination oxygen atoms numbers for Ca^{2+} colored similar as in Fig. 2A. (C). Single-ion free energy profile of Na^+ (black) and Ca^{2+} (red); The energy minima of Na^+ in site S_{HFS}, $S_{S178/L176}$, S_{CEN} and S_{IN} are shown (annotations taken from Payandeh et al. [2]); The energy minima for Ca^{2+} in sites S_{HFS}, $S_{S178/L176}$, and S_{CEN} are colored in red. (D) Snapshot capturing the transition of Na^+ from site S_{HFS} to site $S_{S178/L176}$ with distances between Na^+ (yellow sphere) and adjacent carboxyl oxygens from Glu-177 and Glu-177- Glu-177 distances labeled. (E) Snapshot capturing the transition barrier of Ca^{2+} (magenta sphere) from site S_{HFS} to site $S_{S178/L176}$. (F) Snapshot of Ca^{2+} at site $S_{CEN;}$ the conformational change of Glu-177 side chain is shown in yellow; the cyan shadow indicates the original conformation of this side chain. (G) The crystal structure of Na_VRh revealing a similar Ca^{2+} binding site in the SF [4].

SF, one-ion free energy profiles were calculated along the filter, see Fig. 1 B inset. The binding sites are annotated S_{HFS}, S_{IN} and S_{CEN} in line with Payandeh et al. [2].

3.1. Na^+ and Ca^{2+} binding patterns in the SF

In all six MD simulations the RMSD of the backbone atoms of the SF was below 1.0 Å, indicating stability of the filter. Fig. 1A and B reveal differences in the dynamics of Na^+ and Ca^{2+} binding to the SF of Na_VAb. In agreement with recent MD simulations [27,28], sodium ions can move into the SF from the extracellular bulk water within 5 ns (Fig. 1A). Two Na^+ ions spontaneously accommodated the two favorable sites S_{HFS} and S_{IN} in a hydrated manner (Fig. 1A and D) [6,7]. Occasionally, a sodium ion was observed to spontaneously move into the cavity and back up to site S_{IN} of the SF (Fig. 1A and E). Since the intracellular gate of this crystal structure is closed, no ion conducting event was observed. Similar to sodium, a calcium ion entered the SF from the extracellular bulk water within 5 ns (Fig 1B). However, the Ca^{2+} ion occupied site S_{HFS} for ~40 ns. After 45 ns, Ca^{2+} migrated into a new site formed by backbone nitrogen atoms of residues Ser-178 and Leu-176 (site $S_{S178/L176}$) above site S_{CEN} (Fig. 1B and F). After ~95 ns, calcium moved into site S_{CEN} where it remained for the rest of the simulation (Fig. 1B, C and G). In contrast to simulations with NaCl, in all three simulations with $CaCl_2$, only one Ca^{2+} ion was found to bind to the SF.

3.2. SF dynamics – influence of ion type

Analysis of the trajectory revealed that, in contrast to Na^+ where the filter remained rigid, Ca^{2+} ions induced changes of the Glu-177 side chain (see Fig. 1H and I). After ~45 ns, the χ_2 angles of two adjacent Glu-177 side chains changed from −70° to 45°. These changes facilitate collective Ca^{2+} coordination from two neighboring Glu side chains at site $S_{S178/L176}$ (Fig. 1F and Fig. 2B). After this intermediate state (started from 90 ns), one of the side chains flipped back to its native conformation as observed in the crystal structure, whereas the conformation of the second glutamate changed even further to ~70° (Fig. 1I) when coordinating a Ca^{2+} ion at site S_{CEN} (Fig. 1G). These filter changes enabled more favorable electrostatic interactions with Ca^{2+}.

3.3. Free energy differences

To investigate possible differences in free energy profiles of these two ion species, we performed PMF calculations (Fig. 2C). Since only one calcium ion was observed to occupy the SF in repeated simulations, we calculated one-ion PMFs. The free energy profile of sodium shows four local minima: at site S_{HFS}, site $S_{S178/L176}$, site S_{CEN}, and site S_{IN}. These calculations revealed that Na^+ has no energy barrier higher than 2.1 kcal/mol, suggesting that sodium ions can easily pass the filter. These values are in close agreement with previous studies [6,7,28]. PMF calculations with calcium revealed an energy barrier of approximately ~4.3 kcal/mol

compared to ~1.4 kcal/mol for Na^+. This relatively high barrier is located between sites S_{HFS} and $S_{S178/L176}$ (Fig. 2C), indicating that Ca^{2+} discrimination might occur in this region of the SF. Further analyses of the structural snapshots suggested that this region of the SF does not provide an ideal geometry for calcium ions. Distance measurements between coordinating glutamate oxygens and Ca^{2+}, revealed a less favorable, asymmetric coordination pattern compared to sodium (See Fig. 2D and E). A similar mechanism, albeit at a slightly different site in the SF was proposed by Corry and Thomas for Na^+ versus K^+ discrimination [7]. This energy barrier might be part of the reason why Ca^{2+} movement to site S_{CEN} (Fig. 1B) was rather slow (after ~90 ns versus after ~5 ns for Na^+). The lowest energy well for Ca^{2+} is approximately at site S_{CEN}. Further, PMF calculations revealed that there is a large energy barrier (~5 kcal/mol) for calcium ions after site S_{CEN}, which might prevent movement into the cavity. Remarkably, the high affinity binding site at site S_{CEN} (Fig. 2F) agrees well with the X-ray data by Zhang et al. [4] on the related Na_VRh channel, showing a Ca^{2+} ion bound at site L179/T178 (Fig. 2G).

3.4. Comparison of Na^+ and Ca^{2+} ion coordination

Next, we compared ion solvation patterns for Na^+ and Ca^{2+} in the Na_VAb SF. The nature of the atoms coordinating either a single Na^+ ion or a single Ca^{2+} ion at different positions along the permeation pore are shown in Fig. 2A and B. In accordance with previous simulations on Na^+ permeation, Na^+ ions can bind inside the SF with the entire or part of the inner hydration shell intact [6,7,27,28]. In site S_{HFS}, two of the water molecules from the hydration shell were substituted by side chain oxygen atoms of Glu-177 and Ser-178; at site S_{CEN}, one of the coordinating water molecules was replaced by a carbonyl oxygen atom of Leu-176 (Fig. 2A).

Hydration patterns for Ca^{2+} are shown in Fig 2B. In contrast to sodium, where only one glutamate participates in ion coordination, the conformational changes of the Glu-177 side chains allowed Ca^{2+} coordination with two glutamate side chain oxygen atoms. The pivotal role of the flipped Glu-177 side chain(s) is shown in Fig. 1F, G and I and Fig. 2B. Further, these side chain changes rendered the coordination by Leu-176 backbone oxygen atoms less likely. As a result, the Ca^{2+} distribution was restricted to the center of the pore axis (Fig. 1C, right).

Summarizing, our studies revealed clear differences for Na^+ versus Ca^{2+} behavior in the Na_VAb SF. MD simulations highlight the importance of electrostatic interactions to discriminate between Na^+ and Ca^{2+} in bacterial sodium channels. This is consistent with previous theoretical studies [29–34] of Ca^{2+} and Na^+ channels, which suggested that ion discrimination is primarily governed by electrostatic interactions in the EEEE locus. Interestingly, the association times for Ca^{2+} were rather slower compared to Na^+, which might be explained by a lack of a "loose" knock-on mechanism, shown to be important for Na^+ conductance by recent MD studies [6,7]. In none of our three $CaCl_2$ simulations more than one Ca^{2+} entered the SF. It should be stressed that longer simulation times might be needed to further validate this observation. Future investigations combining NaCl and $CaCl_2$ will be necessary to reveal the role of multi-ion interactions (e.g. Na^+–Ca^{2+} interactions) within the SF.

Acknowledgments

We thank Tobias Linder for helpful discussions and critical reading of the manuscript. This work was supported by The Austrian Science Fund (Grant W1232). The computational results presented have been achieved using the Vienna Scientific Cluster (VSC).

References

[1] W.A. Catterall, From ionic currents to molecular review mechanisms: the structure and function of voltage-gated sodium channels, Neuron 26 (2000) 13–25.
[2] J. Payandeh, T. Scheuer, N. Zheng, W.A. Catterall, The crystal structure of a voltage-gated sodium channel, Nature 475 (2011) 353–358.
[3] J. Payandeh, T.M.G. El-Din, T. Scheuer, N. Zheng, W.A. Catterall, Crystal structure of a voltage-gated sodium channel in two potentially inactivated states, Nature 486 (2012) 135–139.
[4] X. Zhang, W. Ren, P. DeCaen, C. Yan, X. Tao, L. Tang, et al., Crystal structure of an orthologue of the NaChBac voltage-gated sodium channel, Nature 486 (2012) 130–134.
[5] E.C. McCusker, C. Bagnéris, C.E. Naylor, A.R. Cole, N. D'Avanzo, C.G. Nichols, et al., Structure of a bacterial voltage-gated sodium channel pore reveals mechanisms of opening and closing, Nat. Commun. 3 (2012) 1102.
[6] S. Furini, C. Domene, On conduction in a bacterial sodium channel, PLoS Comput. Biol. 8 (2012) e1002476.
[7] B. Corry, M. Thomas, Mechanism of ion permeation and selectivity in a voltage gated sodium channel, J. Am. Chem. Soc. 134 (2011) 1840–1846.
[8] W.A. Sather, E.W. McCleskey, Permeation and selectivity in calcium channels, Annu. Rev. Physiol. 65 (2003) 133–159.
[9] R. Dejian, Sodium leak channels in neuronal excitability and rhythmic behaviors, Neuron 72 (2011) 899–911.
[10] J. Yang, P.T. Elllnor, W.A. Sather, J.I.F. Zhang, R.W. Tsien, Molecular determinants of Ca^{2+} selectivity and ion permeation in L-type Ca^{2+} channels, Nature 366 (1993) 158–161.
[11] S.H. Heinemann, H. Terlau, W. Stühmer, K. Imoto, S. Numa, Calcium channel characteristics conferred on the sodium channel by single mutations, Nature 356 (1992) 441–443.
[12] L. Yue, B. Navarro, D. Ren, A. Ramos, D.E. Clapham, The cation selectivity filter of the bacterial sodium channel, NaChBac, J. Gen. Physiol. 120 (2002) 845–853.
[13] D. Shaya, M. Kreir, R.A. Robbins, S. Wong, J. Hammon, A. Brüggemann, et al., Voltage-gated sodium channel (Na_V) protein dissection creates a set of functional pore-only proteins, Proc. Nat. Acad. Sci. 108 (2011) 12313.
[14] B. Hess, C. Kutzner, D. Van Der Spoel, E. Lindahl, GROMACS 4: algorithms for highly efficient, load-balanced, and scalable molecular simulation, J. Chem. Theory Comput. 4 (2008) 435–447.
[15] V. Hornak, R. Abel, A. Okur, B. Strockbine, A. Roitberg, C. Simmerling, Comparison of multiple Amber force fields and development of improved protein backbone parameters, Proteins 65 (2006) 712–725.
[16] S.W.I. Siu, R. Vácha, P. Jungwirth, R.A. Böckmann, Biomolecular simulations of membranes: physical properties from different force fields, J. Chem. Phys. 128 (2008) 125103.
[17] W.L. Jorgensen, J. Chandrasekhar, J.D. Madura, R.W. Impey, M.L. Klein, Comparison of simple potential functions for simulating liquid water, J. Chem. Phys. 79 (1983) 926–935.
[18] B. Hess, H. Bekker, H.J.C. Berendsen, J.G.E.M. Fraaije, LINCS: a linear constraint solver for molecular simulations, J. Comput. Chem. 18 (1997) 1463–1472.
[19] T. Darden, D. York, L. Pedersen, Particle Mesh Ewald: an N log (N) method for Ewald sums in large systems, J. Chem. Phys. 98 (1993). 10089-10089.
[20] I.S. Joung, T.E. Cheatham III, Determination of alkali and halide monovalent ion parameters for use in explicitly solvated biomolecular simulations, J. Phys. Chem. B 112 (2008) 9020–9041.
[21] S. Nose, A unified formulation of the constant temperature molecular-dynamics methods, J. Chem. Phys. 81 (1984) 511–519.
[22] W.G. Hoover, Canonical dynamics: equilibrium phase-space distributions, Phys. Rev. A 31 (1985) 1695–1697.
[23] R. Martoňák, A. Laio, M. Parrinello, Predicting crystal structures: the Parrinello-Rahman method revisited, Phys. Rev. Lett. 90 (2003) 75503.
[24] G.M. Torrie, J.P. Valleau, Monte Carlo free energy estimates using non-Boltzmann sampling: application to the sub-critical Lennard-Jones fluid, Chem. Phys. Lett. 28 (1974) 578–581.
[25] J.A. Lemkul, D.R. Bevan, Assessing the stability of Alzheimer's amyloid protofibrils using molecular dynamics, J. Phys. Chem. B 114 (2010) 1652–1660.
[26] J.S. Hub, B.L. de Groot, D. van der Spoel, G_wham—a free weighted histogram analysis implementation including robust error and autocorrelation estimates, J. Chem. Theory Comput. 6 (2010) 3713–3720.
[27] V. Carnevale, W. Treptow, M.L. Klein, Sodium ion binding sites and hydration in the lumen of a bacterial ion channel from molecular dynamics simulations, J. Phys. Chem. Lett. 2 (2011) 2504–2508.
[28] H. Qiu, R. Shen, W. Guo, Ion solvation and structural stability in a sodium channel investigated by molecular dynamics calculations, Biochim. Biophys. Acta (BBA) – Biomembr. 2012 (1818) 2529–2535.
[29] D. Boda, D.D. Busath, D. Henderson, S. Sokolowski, Monte Carlo simulations of the mechanism for channel selectivity: the competition between volume exclusion and charge neutrality, J. Phys. Chem. B 104 (2000) 8903–8910.
[30] D. Boda, D.D. Busath, B. Eisenberg, D. Henderson, W. Nonner, Monte Carlo simulations of ion selectivity in a biological Na channel: charge–space competition, Phys. Chem. Chem. Phys. 4 (2002) 5154–5160.
[31] D. Boda, T. Varga, D. Henderson, D.D. Busath, W. Nonner, D. Gillespie, et al., Monte Carlo simulation study of a system with a dielectric

boundary: application to calcium channel selectivity, Mol. Simul. 30 (2004) 89–96.
[32] B. Corry, S.H. Chung, Mechanisms of valence selectivity in biological ion channels, Cell. Mol. Life Sci. 63 (2006) 301–315.
[33] T. Dudev, C. Lim, Why voltage-gated Ca^{2+} and bacterial Na^{+} channels with the same EEEE motif in their selectivity filters confer opposite metal selectivity, Phys. Chem. Chem. Phys. 14 (2012) 12451–12456.
[34] T. Dudev, C. Lim, Competition among Ca^{2+}, Mg^{2+}, and Na^{+} for model ion channel selectivity filters: determinants of ion selectivity, J. Phys. Chem. B 116 (2012) 10703–10714.
[35] S. Koneshan, J.C. Rasaiah, R.M. Lynden-Bell, S.H. Lee, Solvent structure, dynamics, and ion mobility in aqueous solutions at 25 °C, J. Phys. Chem. B 102 (1998) 4193–4204.

4.2 Different Inward and Outward Conduction Mechanisms in Na_VMs Suggested by Molecular Dynamics Simulations

Song Ke, E. N. Timin, Anna Stary-Weinzinger

PLoS Computational Biology

2014 Jul 31;10(7):e1003746

OPEN ACCESS Freely available online

PLOS | COMPUTATIONAL BIOLOGY

Different Inward and Outward Conduction Mechanisms in Na_VMs Suggested by Molecular Dynamics Simulations

Song Ke, E. N. Timin, Anna Stary-Weinzinger*

Department of Pharmacology and Toxicology, University of Vienna, Vienna, Austria

Abstract

Rapid and selective ion transport is essential for the generation and regulation of electrical signaling pathways in living organisms. Here, we use molecular dynamics (MD) simulations with an applied membrane potential to investigate the ion flux of bacterial sodium channel Na_VMs. 5.9 μs simulations with 500 mM NaCl suggest different mechanisms for inward and outward flux. The predicted inward conductance rate of ~27±3 pS, agrees with experiment. The estimated outward conductance rate is 15±3 pS, which is considerably lower. Comparing inward and outward flux, the mean ion dwell time in the selectivity filter (SF) is prolonged from 13.5±0.6 ns to 20.1±1.1 ns. Analysis of the Na^+ distribution revealed distinct patterns for influx and efflux events. In 32.0±5.9% of the simulation time, the E53 side chains adopted a flipped conformation during outward conduction, whereas this conformational change was rarely observed (2.7±0.5%) during influx. Further, simulations with dihedral restraints revealed that influx is less affected by the E53 conformational flexibility. In contrast, during outward conduction, our simulations indicate that the flipped E53 conformation provides direct coordination for Na^+. The free energy profile (potential of mean force calculations) indicates that this conformational change lowers the putative barriers between sites S_{CEN} and S_{HFS} during outward conduction. We hypothesize that during an action potential, the increased Na^+ outward transition propensities at depolarizing potentials might increase the probability of E53 conformational changes in the SF. Subsequently, this might be a first step towards initiating slow inactivation.

Citation: Ke S, Timin EN, Stary-Weinzinger A (2014) Different Inward and Outward Conduction Mechanisms in Na_VMs Suggested by Molecular Dynamics Simulations. PLoS Comput Biol 10(7): e1003746. doi:10.1371/journal.pcbi.1003746

Editor: Emad Tajkhorshid, University of Illinois, United States of America

Received December 17, 2013; **Accepted** June 13, 2014; **Published** July 31, 2014

Funding: This work was supported by The Austrian Science Fund (FWF) Project W1232. The funders had no role in study design, data collection and analysis, decision to publish, or preparation of the manuscript.

Competing Interests: The authors have declared that no competing interests exist.

* Email: anna.stary@univie.ac.at

Introduction

Na^+ flux through voltage gated sodium channels (Na_V) is crucial for initiating action potentials in the membranes of electrically excitable cells. They mediate a variety of biological functions such as muscle contraction, propagation of nerve impulses, release of hormones and many more [1]. As a consequence, mutations in Na_V channels lead to a variety of channelopathies, such as congenital epilepsy, cardiac arrhythmias or chronic pain [2,3].

Recently, homotetrameric crystal structures of several bacterial Na_V channels were successfully resolved [4–10], providing a tremendous opportunity to investigate the structure and function of these channels on the atomistic level. They are composed of four membrane spanning subunits and contain six transmembrane (TM) helices per subunit. Helices S1 to S4 form the voltage sensing module. Helices S5, P1 segments, the selectivity filter (SF) region, P2 segments and S6 helices, lining the inner pore cavity, form the pore module. The SF of most bacterial channels contains the amino acid sequence TLESW. The four glutamic acid side chains [11] form a high field strength binding site (HFS) [12] which is essential for ion selectivity. In eukaryotic sodium channels, this site consists of the amino acids motif DEKA.

The molecular mechanisms underlying ion conduction and selectivity in Na_V are beginning to emerge. Computational methods, particularly molecular dynamics (MD) simulations are extensively adopted to address these questions [13–23].

As reviewed recently [24], sodium ions were illustrated to spontaneously traverse the SF into the cavity with energy barriers between ~2–5 kcal/mol. Compared to potassium coordination in K_V channels, sodium ions partially or fully preserve their first hydration shells [13,15–17,20,22]. A loosely coupled knock-on mechanism with an average ion occupancy around two in the SF was predicted during ion conduction [14,15,21,22]. The incoming ion repulses the present ion out of the SF. The wide radius (≥9 Å) of the SF enables double occupancy of ions at the same level [20,21]. Further, Na^+ vs. K^+ [15,16,20,20–22] and Na^+ vs. Ca^{2+} [17,20] discrimination studies were carried out. These studies revealed higher energy barriers in the SF for K^+ and Ca^{2+} compared to Na^+. Subsequently, non-equilibrium simulations were performed to investigate conduction under applied membrane potentials and to study kinetics [21,22]. The estimated inward conductance rate successfully reproduced electrophysiology data [22].

A recent study by Chakrabarti et al. [23], suggested that conformational changes at the EEEE motif (corresponding to E177 in Na_VAb) might play an important role in ion conduction. However, this observation was not reported in other simulations, except for simulations using Ca^{2+} as a charge carrier [17]. In K^+ channels, subtle structural changes in the SF, involving rotations around a highly conserved glycine residue result in different non-conductive conformations [25,26]. This regulation of ion flow by conformational changes of the selectivity filter is termed C-type inactivation.

Author Summary

Voltage gated sodium channels are essential components of living cell membranes. They regulate the cell potential by facilitating permeation of ions across the membrane. In the past decades, studies revealed that the bacterial selectivity filter (SF) exhibits a constricted architecture lined with electronegative carboxyl oxygens of four glutamic acid side chains (EEEE motif), which repulse anions but attract Na^+ ions. Crystal structures enable the investigation of structural dynamics with computational methods. Ion selectivity and conduction mechanisms between Na^+, K^+ and Ca^{2+} are progressively elucidated by molecular dynamics simulations and free energy calculations. The structural dynamics of the protein, especially the flexibility of SF and its fundamental role in kinetics underpinning ion selectivity, conduction and channel gating are less well understood. To shed light on this question, we use computational simulations to simulate ion conduction with membrane potentials. Our results suggest different dynamical behaviors of the EEEE locus and distinct ion distribution patterns in the SF with respect to permeating directionalities. These findings indicate a novel mechanism in differentiating reciprocal transitions of ion flow, preventing large sodium efflux during action potential initiation and may further suggest that increased flipping propensities at depolarizing potentials, might initially trigger channel slow inactivation.

It is not clear to which extend structural changes at the EEEE locus in Na_v channels are crucial for conductance and inactivation in Na_v channels.

To investigate these issues, we conducted MD simulations using the open conformation of the bacterial sodium channel homologue Na_VMs (Magnetococcus sp. (strain MC-1)) [7] pore domain focusing on the structural changes of the SF during inward and outward conduction.

Results

Single channel conductance

The four-fold symmetrical structure of Na_VMs (pdb identifier: 4F4L) was generated using chain A (splayed outward by 25° rotation about its Ψ-bond at position T84), which creates an open pore with a diameter of ~14 Å [7]. As described by Ulmschneider et al. [22], a harmonic restraint was exerted on the S5 and S6 TM helices to keep the gate in the open conformation throughout simulations. This structure was then embedded into a POPC lipid patch and duplicated in the Z direction (pore axis). A constant charge imbalance of four elementary charges (4 *e*) across each lipid bilayer between the central electrolyte bath and the two outer ones was maintained during simulation (supplementary movie S1) [27].

Four times 500 ns double-patch MD simulations with 500 mM NaCl were performed, with the first 100 ns treated as equilibration. Figure 1 shows the cumulative ion conducting events from MD simulations with depolarized and hyperpolarized membrane potentials of ΔV: 565±126 mV (Figure 2A). The estimated sodium current in the inward direction is γ = 27±3 pS. This value agrees with previously observed single channel conductance measurements (γ~33 pS) [22]. Our double bilayer simulations enabled us to further estimate outward conduction, which amounts to γ = 15±3 pS. Interestingly, this process is distinguishably slower than inward ion flux ($P<0.01$, $N=4$).

Ion distribution patterns and kinetics

To explore the underlying differences between inward and outward ion permeation, we plotted the ion probability density map across the pore region from all four simulations. Several favorable ion-interacting sites (S_{EX}, S_{HFS}, S_{CEN} and S_{IN}) from periplasm to cytoplasm were assigned as proposed previously by Payandeh et al. [4]. The ion-interacting sites across the SF were determined by measuring the axial distance (Z axis) along certain atoms from −5.00 to 10.25 Å as shown in Figure 3. Side chain oxygens of S54 from all four chains were taken as the origin (Z = 0.0 Å) of the SF. Additionally, in two previous studies, a site with an energy barrier (~2 kcal/mol) distinguishing between site S_{HFS} and S_{CEN} was identified [17,22]. In this study, we refer to this site as "S_{BAR}", indicating this barrier ($2.75 \leq Z < 4.75$ Å).

During influx (Figure 4A and B), short-lived Na^+ binding at site S_{EX} was observed (2.6±0.5 ns) in an asymmetrical manner. S_{HFS} is the dominant site with the highest ion density. At this site, ions tended to be directly coordinated with side chain oxygens of E53 and S54 in an off-axis manner. Additionally, a less densely populated configuration was observed in the center of this site consistent with previous studies [21,24]. Moving inward from site S_{HFS}, ions further translocated transiently via site S_{BAR} (1.5±0.3 ns) to site S_{CEN} (3.4±0.3 ns). Subsequently, ions reciprocally traversed between sites S_{CEN} and S_{IN}. These results are in good agreement with previous simulation studies [14,15,17,21,22].

Our simulations revealed a distinct ion distribution pattern for efflux compared to influx as shown in Figure 4C and D. After entering into site S_{IN} from the cytosol, ions mainly populated sites S_{CEN} and S_{BAR} with extended dwell times compared to inward conduction, (S_{CEN}: 11.9±1.1 ns vs. 3.4±0.3 ns; S_{BAR}: 8.2±0.9 ns vs. 1.5±0.3 ns) suggesting a putative barrier for efflux between sites S_{BAR} and S_{HFS}. Additionally, during efflux, Na^+ ions tended to traverse in an on-axis manner through the filter.

Structural dynamics of glutamic acid

Conformational isomerization of the E53 side chains has been reported previously [17,23]. Generally, the glutamic acid side chain might adopt two main conformations (Figure 5A and B): inward-facing (χ_2 angle ~60°, flipped) and outward-facing (χ_2 angle ~290°, non-flipped). In our simulations, during influx, flipping events were observed only in 2.7±0.5% of the simulation time, thus the E53 side chain mainly adopted a non-flipped conformation. In contrast, during efflux 32.0±5.9% flipping events were observed (P value = 0.015, see Figure 5C). A more detailed investigation of this flipping events revealed that 80% of these changes occurred in only one of the four glutamic acid side chains ("one-flip") (Figure 5D).

To investigate the influence of the presence of Na^+ ions on E53 side chain dynamics, three repeated simulations without ions in the SF ("no salt") were performed. Irrespective of the directionality of the applied potentials, the flip probability is less than 0.6% in all simulations (Figure 5C). This indicates, that a depolarizing potential per se does not significantly influence the number of E53 flipping events. This suggests that the combination of local positive charge carried by outward Na^+ flux in the SF especially at sites S_{HFS} and S_{BAR} and the outward attracting membrane potential might collectively induce the rotation of the χ_2 angle from ~290° to ~60°.

Ionic binding modes and conduction mechanism during inward conduction

A detailed investigation of the ionic binding modes and their relations to free energy profiles enabled us to describe mechanisms

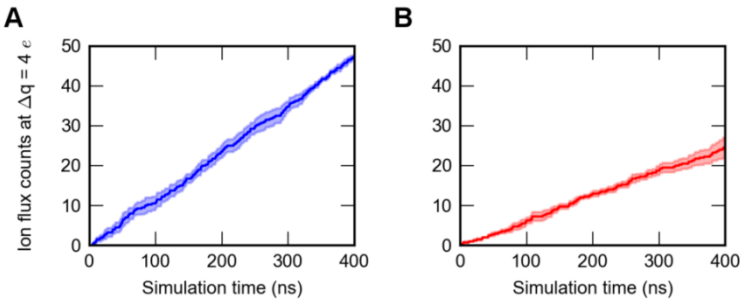

Figure 1. Ion flux in double bilayer simulations without dihedral restraints on E53 (n = 4). A) Average ion flux count of inward conduction through the SF over time (color: blue). B) Average ion flux count of outward conduction through the SF over time (color: red). Error estimations shown in the figure are S.E.M.
doi:10.1371/journal.pcbi.1003746.g001

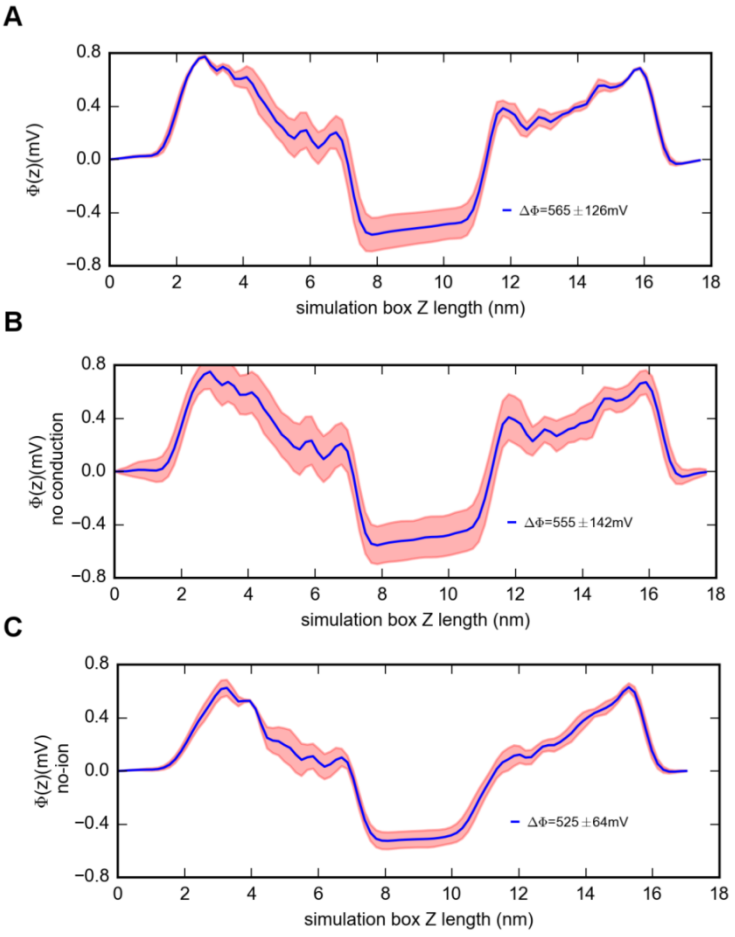

Figure 2. Transmembrane voltages comparison. A) Electrostatic potential across the simulation box calculated from the simulations without dihedral restraints on E53. B) Electrostatic potential across the simulation box calculated from the snapshots (t>5 ns) extracted from the simulation in Figure 2A without ion conduction events in neither inward nor outward directions. C) Electrostatic potential across the simulation box calculated from the "no salt" simulations. (Error estimations shown in the figure are S.D.).
doi:10.1371/journal.pcbi.1003746.g002

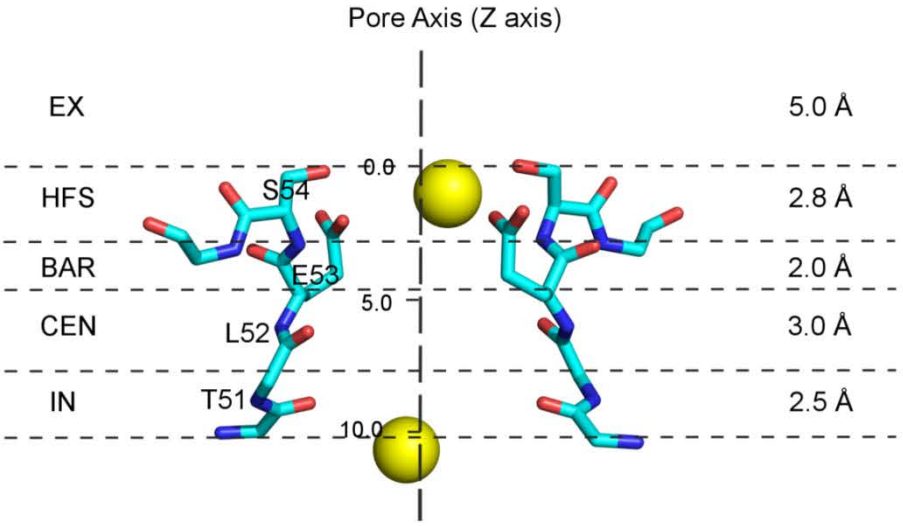

Figure 3. Annotations of the SF ion interacting site. SF backbone atoms are shown as blue sticks, E53 and S54 side chain atoms are also shown to determine the site S_{HFS} (only two opposite subunits are shown for clarity). In addition, sodium ions are depicted with yellow spheres. Sites S_{EX} ($-5.00 \leq Z < 0.00$ Å), S_{HFS} ($0.00 \leq Z < 2.75$ Å), S_{BAR} ($2.75 \leq Z < 4.75$ Å), site S_{CEN} ($4.75 \leq Z < 7.75$ Å) and site S_{IN} ($7.75 \leq Z < 10.25$ Å) and the length of each site were annotated at the lateral sides of the figure.
doi:10.1371/journal.pcbi.1003746.g003

regarding different conducting directionalities (Figure 6 and 7). During inward conduction, the largest barrier in the SF occurs between sites S_{HFS} and S_{BAR} which amounts to 2.1 kcal/mol (Figure 6B). At site S_{HFS}, the probe ions (yellow) mainly distributed in an off-axis manner, the first coupling Na^+ ions (blue) may occupy site $S_{CEN\ (IN)}$, and there existed a second binding site for coupling ions at site S_{EX} (Figure 6A, II). Subsequently, the probe ions distributed in the middle of channel axis when traversing the short lived site S_{BAR}, with the other two coupling ions populating sites S_{EX} and $S_{IN\ (CAV)}$ respectively (Figure 6A, III). The probe ions then occupied site S_{CEN} in both on-axis and off-axis manners, other coupling ions in the SF were distributed mainly at sites S_{IN} and S_{EX}. Only a few coupled ions occupied sites S_{HFS} and S_{BAR} (Figure 6A, IV).

In these ionic binding modes, under hyperpolarized potential, the coupling ions in the SF generally demonstrated a loosely coupled knock-on mechanism with only a few of them present in the adjacent binding sites to the probe ions (Figure 6A, II–IV). This is in agreement with a study by [21,22], where it was shown that during inward conduction the ions displayed a combination of mono-ionic and multi-ionic mechanism with an overall occupancy of 1.8 ions in the pore region.

The flipping probability analysis indicates that the conformational changes of the E53 side chains play a minor role for ion inward conduction as shown in Figure 6A, II′–IV′.

Ionic binding modes and conduction mechanism during outward conduction

Compared to inward permeation, the maximum energy barrier during outward conduction amounted to 2.3 kcal/mol between sites S_{BAR} and S_{HFS}. It is interesting that the free energy difference between sites S_{CEN} and S_{HFS} is 2.2 kcal/mol, which is close to the largest energy barrier (Figure 7B). In addition, the ionic binding modes demonstrate a distinct conduction mechanism compared to Na^+ influx. Traversing outward from the cavity, ions at site S_{IN} were tightly coupled with ions at site S_{BAR} (Figure 7A, III and V) corresponding to two energy wells in Figure 7B, III and V). When probe ions located at site S_{CEN}, the coupling ions distributed in the upper part of the cavity (Figure 7A, IV) which corresponds to the energy well at site S_{CEN} (Figure 7B, IV). Generally, the translocation of probe ions from the cytoplasm to site S_{BAR} is readily stepwise by a tight knock-off mechanism without significant energy barriers. At all three energy wells (Figure 7B III–V) the E53 side chains maintained non-flipped conformations.

When probe ions faced the energy barrier at site S_{BAR}, a delicate tightly-coupled "knock-off" conducting mechanism occurred. Initially, E53 started to flip and one of the carboxyl oxygens started to coordinate the probe ions (Figure 7A, III′ and S5, B). Compared to ions located in the close energy wells (Figure 7A, III), the probe ions were meanwhile expulsed by the outward movements of approaching coupling ions at site S_{IN} (Figure 7A, III′). If this knock-off mechanism was successful, the probe ions would then migrate to site S_{HFS}, as a result, the coupling ions would move outward to site S_{CEN} simultaneous (Figure 7A, II′ and IV′). At this time, two carboxyl oxygens of the flipped E53 side chain tended to coordinate with the probe ions and coupling ions respectively (Figure 7A, II′ and IV′ and S5, B). Afterwards, ions left site S_{HFS} promptly ($t = 2.6$ ns) into the periplasm via site S_{EX}.

If the attempt to overcome the barrier failed, the aforementioned mechanism was easily reversed, the probe ions and coupling ions occupied the two stable energy wells at sites S_{BAR} with the coupling ions at site S_{IN} (Figure 7A, III and V) and site S_{CEN} with the coupling ions in the cavity (Figure 7A, IV) again. That is the reason why ions stayed longer in sites S_{BAR} and S_{CEN}.

One the one hand, larger Pi values (flip inducing probability of number of probe ions, see methods for details) values of sites S_{BAR}, S_{CEN} and S_{HFS} indicated the flipped conformations of E53 were crucial (Pi>90%) in overcoming the dual energy barriers between S_{CEN}, S_{BAR} and S_{HFS}. On the other hand, smaller Pt values

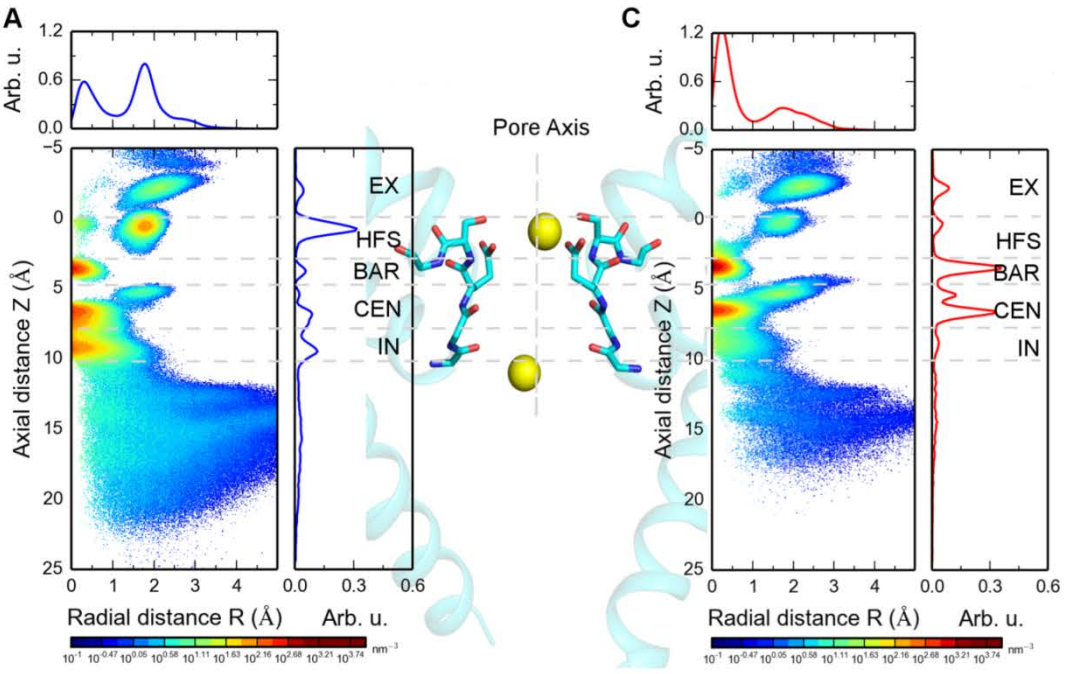

B

Sites	Mean_time(ns)	Length (Å)
EX	2.6±0.5	5.0
HFS	5.6±0.5	2.8
BAR	1.5±0.3	2.0
CEN	3.4±0.3	3.0
IN	6.4±0.5	2.5
CAV	9.4±0.6	14.8
SF	**13.5±0.6**	**15.3**
PORE	**18.7±0.8**	**30.0**

D

Sites	Mean_time(ns)	Length (Å)
EX	3.1±0.7	5.0
HFS	2.6±0.6	2.8
BAR	8.2±0.9	2.0
CEN	11.9±1.1	3.0
IN	8.3±1.1	2.5
CAV	6.4±1.0	14.8
SF	**20.1±1.1**	**15.3**
PORE	**23.1±1.2**	**30.0**

Figure 4. Ion distribution probability density map. A) Ion distribution of inward simulations labeled with respective interacting sites [4], lower left: 2-D (axial and radial distribution) density; lower right: 1-D axial distribution along the pore axis; upper left: 1-D radial distribution from the center of the pore axis. B) Inward dwell time in respective interacting sites (158 ion conduction events from four simulations were taken for analysis). C) Ion distribution of outward simulations labeled with respective interacting sites [4], lower left: 2-D (axial and radial distribution) density; lower right: 1-D axial distribution along the pore axis; upper left: 1-D radial distribution from the center of pore axis. D) Outward dwell time in respective interacting sites (79 ion conduction events from four simulations were taken for analysis).
doi:10.1371/journal.pcbi.1003746.g004

(flipping time probability for all probe ions, see methods for details) values indicated that the flipping events were easily reversible. Because of these flipping events, the major ion distribution for outward conduction is limited to the center of the channel axis during translocation within the SF.

E53 conformation determines efflux rate

To further explore the correlation between flux directionality and E53 conformation, we performed two sets of inward and outward conduction simulations (four times 300 ns) with dihedral restraints to maintain "non-flip" and "one-flip" configurations during sampling. The influx rate was independent of the E53 conformations as shown in Figure 8A. This observation disagrees with recent data from Chakrabarti et al. [23] on the Na_VAb channel. The outward conduction with "one-flip" simulation displayed an increased efflux rate compared to simulations without dihedral restraints on E53, where the flipping events would be reversible when conducting ions (Figures S1, S2, S3, S4). Interestingly, if E53 was restrained to a "non-flip" configuration, sodium ions translocation slowed down (Figure 8B). These results suggest a clear influence of filter dynamics on the efflux rate.

Comparison of the free energy profiles from outward simulations of these three types of configurations revealed that the largest energy barrier of the "non-flip" simulations is increased from 2.3 kcal/mol (non-restraint) to 3.4 kcal/mol (Figure 9A and C). The lowest energy well at site S_{BAR} was also replaced by site S_{CEN}. The energy profile of "one-flip" simulations indicated that the energy barrier between sites S_{CEN} and S_{HFS} was diminished,

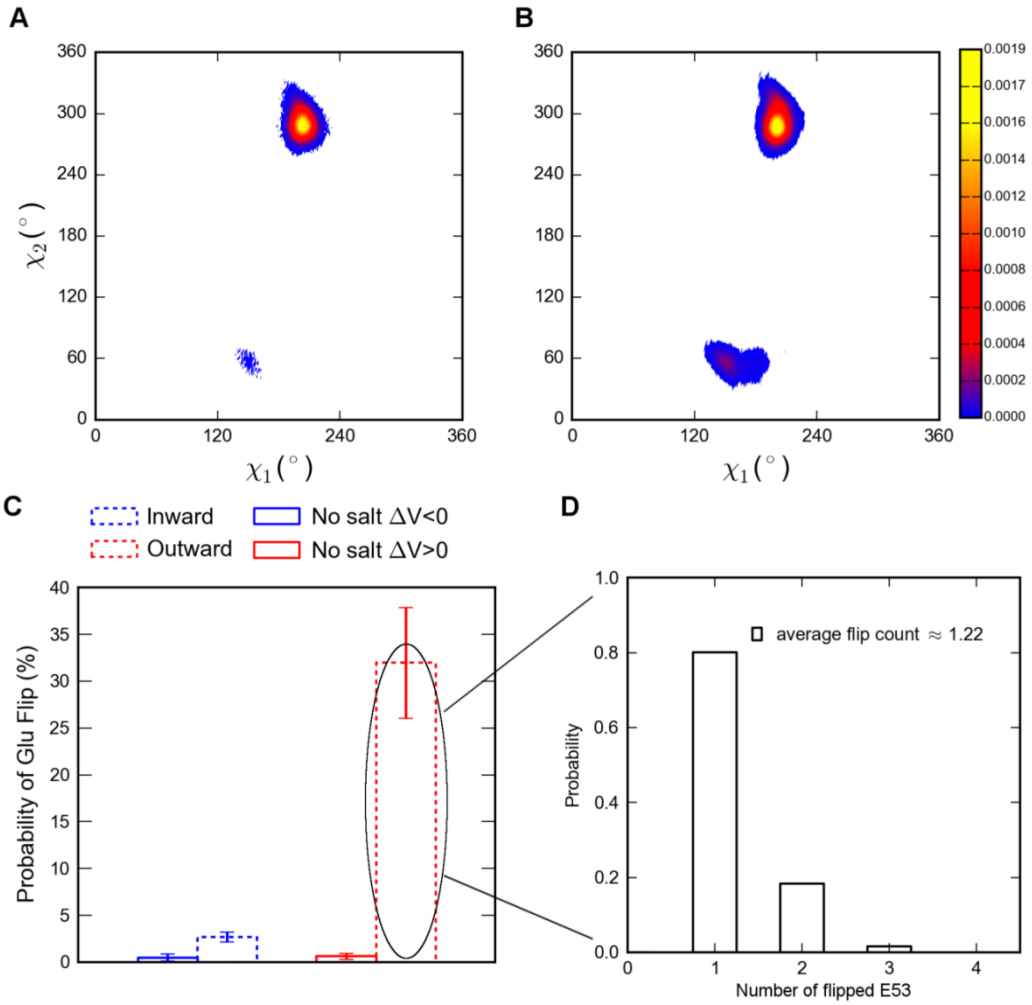

Figure 5. E53 conformational changes. A) χ_1-χ_2 angle distribution of the inward conductance simulations. B) χ_1-χ_2 angle distribution of the outward conductance simulations. C) The probability of flipping events of E53 side chains, the inward conduction is depicted as blue dotted histogram. The outward conduction is depicted as red dotted histogram (a flip is defined when at least one out of four subunits was shifted to flipping state in an analyzing window over time from four simulations); Control simulations with ions not in the SF ("no salt") at hyperpolarized and depolarized membrane potentials are depicted as blue and red solid histograms, respectively. Error estimations shown in the figure are S.E.M. D) The distribution of E53 flipping numbers from all flipping events during outward conduction.
doi:10.1371/journal.pcbi.1003746.g005

although the original energy barrier increased slightly by 0.3 kcal/mol (Figure 9A and B). Therefore, the outward conduction would be more straightforward without reversible backward translocation compared to the simulations without the dihedral restraints from a kinetic point of view.

Discussion

The mechanism of ion conduction and selectivity of bacterial voltage gated sodium channels is gradually emerging. The inverted tepee shape architecture of the SF lined with TLESW sequence enables sodium influx at the diffusion rate. The glutamic acid side chains are responsible for recruiting Na^+ ions from the outer vestibule. Ions will then translocate via sites S_{HFS}, S_{BAR}, S_{CEN} and S_{IN} spontaneously to complete a conduction event [21–23]. Details of conduction are only partially understood. Large conformational changes of the glutamic acid side chains were described recently [23]. However, its role for conduction is still under discussion [24].

To gain further insights into these questions, we performed MD simulations to compare the different binding patterns and characterize the structural dynamics of glutamic acids during ion permeation. Double bilayer simulations with the open Na_VMs structure enabled us to investigate influx and efflux separately. The calculated inward conductance rate is in good agreement with a previously reported experiment and computational data [22]. The

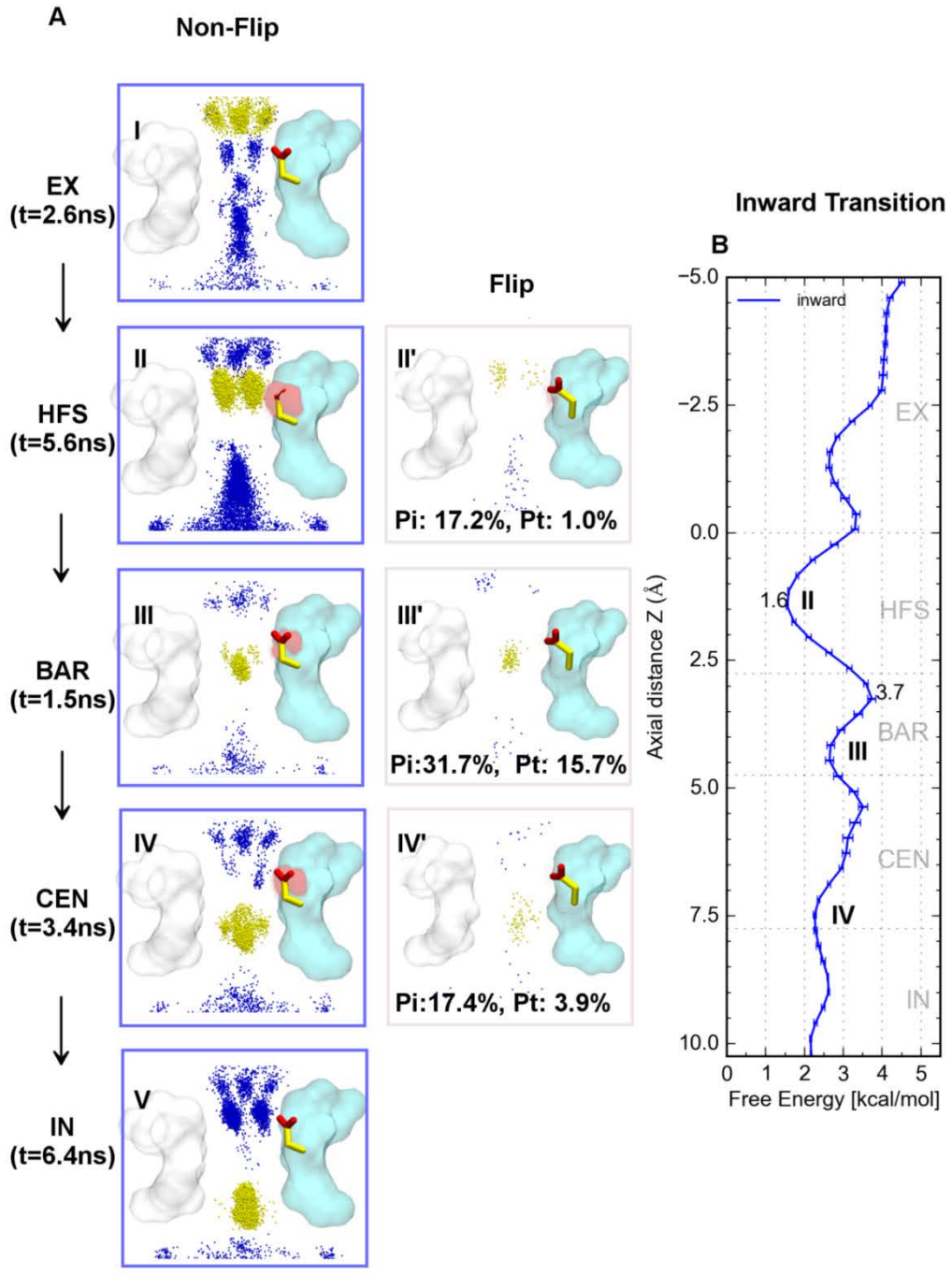

Figure 6. Inward ionic binding modes and PMF. A) Overlay of the conformational space of the probe ions (yellow), coupling sodium ions (blue) and E53 carboxyl oxygen distributions (transparent spheres with different intensity) for different ionic binding modes at different interaction sites. A snapshot of a typical E53 sidechain conformation is shown as stick representation (red, carboxyl oxygens; yellow, sidechain carbons), I–V are non-flip binding modes and II′–IV′ are flipping binding modes for sites S_{HFS}, S_{BAR} and S_{CEN}. Arrows indicate the direction of ion conduction; B) 1-D PMF of inward conduction in SF region, the largest free energy barrier is labeled by a terminal peak and well, corresponding positions of typical binding modes on the energy profile are labeled. Error estimations shown in the figure are S.E.M.
doi:10.1371/journal.pcbi.1003746.g006

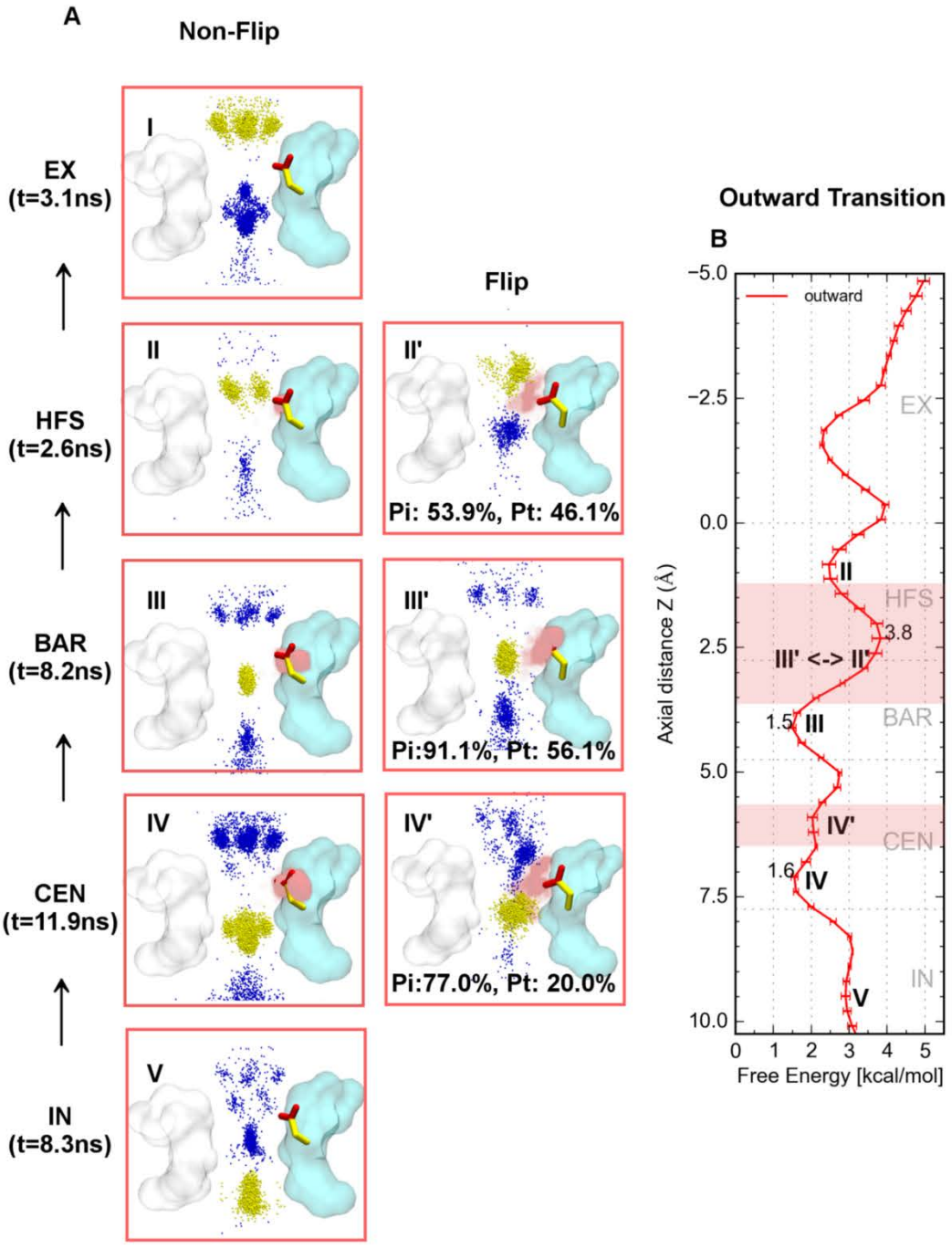

Figure 7. Outward ionic binding modes and PMF. A) Overlay of the conformational space of the probe ions (yellow), coupling sodium ions (blue) and E53 carboxyl oxygen distributions (transparent spheres with different intensity) for different ionic binding modes at different interaction sites. A snapshot of a typical E53 sidechain conformation is shown as stick representation (red, carboxyl oxygens; yellow, sidechain carbons), I–V are non-flip binding modes and II′–IV′ are flipping binding modes for sites S_{HFS}, S_{BAR} and S_{CEN}. Arrows indicate the direction of ion conduction; B) 1-D PMF of outward conduction in SF region, the largest free energy barriers are labeled by terminal peaks and wells, corresponding positions of typical binding modes on the energy profile are labeled. Error estimations shown in the figure are S.E.M.
doi:10.1371/journal.pcbi.1003746.g007

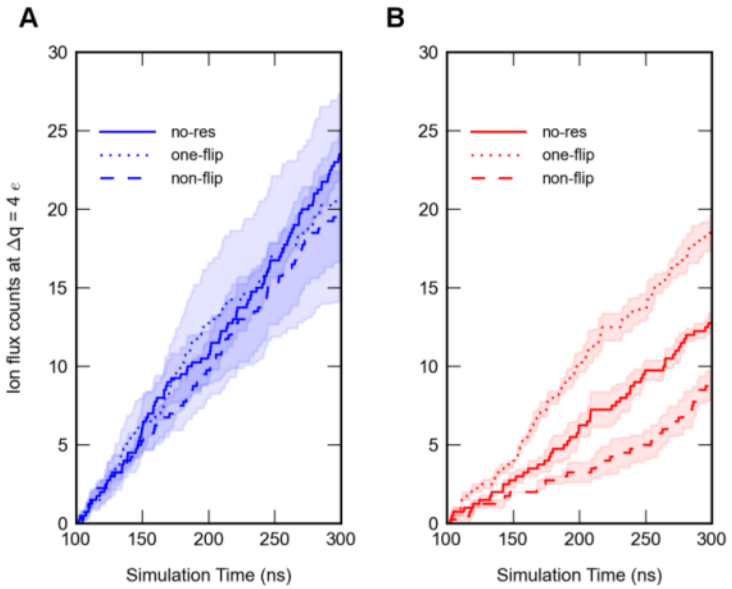

Figure 8. Influences of different flipping states at $\Delta q = 4e$ (n = 4). A) Average ion flux counts through the SF over time of inward conduction (color: blue). The simulations without restraints of E53 are depicted as solid line, the ones with the "one-flip" restraints are shown as dotted line and the ones with the "non-flip" restraints are shown as dashed line. B) Average ion flux count through the SF over time of outward conduction (color: red). Error estimations shown in the figure are S.E.M.
doi:10.1371/journal.pcbi.1003746.g008

estimated outward conductance rate obtained from MD simulations is predicted to be markedly lower than inward permeation (15±3 pS vs 27±3 pS, Figure 1). Ion translocation between sites S_{BAR} and S_{HFS} is substantially prolonged (8.2±0.9 ns vs 1.5±0.3 ns, Figure 4) during Na^+ efflux. From the energetic point of view, this would imply a potential barrier. This agrees with previous two-ion free energy calculation studies, revealing a higher energy barrier in this region for outward current compared to inward conduction (ΔG: 4.6 kcal/mol vs 0.4 kcal/mol, Stock et al. [21]; ΔG: 3.5±0.5 kcal/mol and 2.4±0.3 kcal/mol, Furini and Domene [15]). In our studies, this barrier is also higher for outward conduction (ΔG: 2.3 kcal/mol vs. 2.1 kcal/mol).

In agreement with previous studies [21,22] during inward conduction, our simulations revealed that ion translocations in the SF generally involve a loosely coupled knock on mechanism with an average ion occupancy of 1.8 (Figure 6).

A possible outward conduction mechanism was described by Stock et al., [21] using a "fully activated-open" Na_VAb channel structure [28]. They have found a third ion denoted k, directly coupling with the probe ions triggering outward conduction by a "nudging" collision effect. Similar results were obtained in our study, which shows that the coupling ions directly couple with the probe ions by a tight "knock-off" mechanism. Moreover, our simulations further elucidated that this "knock-off" mechanism is highly dependent on the conformational isomerization of the glutamic acid side chains in the SF. In other words, to overcome the energy barriers of outward conduction, at least one of the glutamic acid side chains has to be flipped to an inward facing conformation (Figure 7).

A recent simulation study under ~0 mV membrane potential with a closed gate Na_VAb structure suggested that Na^+ in- and outward movement involves variable configurations of multiple glutamic acid side chains giving rise to non-simple degenerated ion binding modes [23]. Remarkably, detailed investigations of the structural dynamics of E53 in our study revealed distinct isomerization patterns between forward and backward translocations respectively. When the ion moved into the SF from the outer vestibule under hyperpolarized membrane potential, the E53 remained mostly in the non-flipped conformation. In contrast, during outward conduction, the flipping occurrence increased significantly with a typical "one-flip" configuration (Figure 5C and D) when coordinating ions occupied the SF (Figure 7). In our simulations, the depolarized and hyperpolarized membrane potentials of approximately ΔV: 565 mV enabled the detailed investigation of ion permeation directionalities. This was not possible in previous simulations at ~0 mV [23]. The conductive, open gate structure used in this study may also reduce the repulsive effect which could have been induced by ions present in the cavity in previous simulations with a closed gate [23]. In addition, different forcefields used in these two studies may also play a substantial role for these discrepancies. As reported by Cordomi et al [29]), compared to the combination of OPLS-AA protein with Berger lipids parameters, combining Amber99sb protein and Berger lipids gives more accurate free energies of solvation in water and water to cyclohexane transfer with respect to experimental data for glutamic acid side chains. This may explain the reduced flexibility of the glutamic acid side chain dynamics observed in our study. Further, the force field discrepancies might explain the contrasting results for the "no salt" simulations in these two studies. In the study by Chacrabarti et al [23], the E side chains are more favorable to form flipped conformations even in the "no salt" conformation. This is in contrast to our simulations, where flipping events occurred rarely (Figure 5C) in the "no salt" simulations.

While the inward flow exhibited indistinguishable flux rates irrespective of the E53 conformation (Figure 8A), efflux displayed

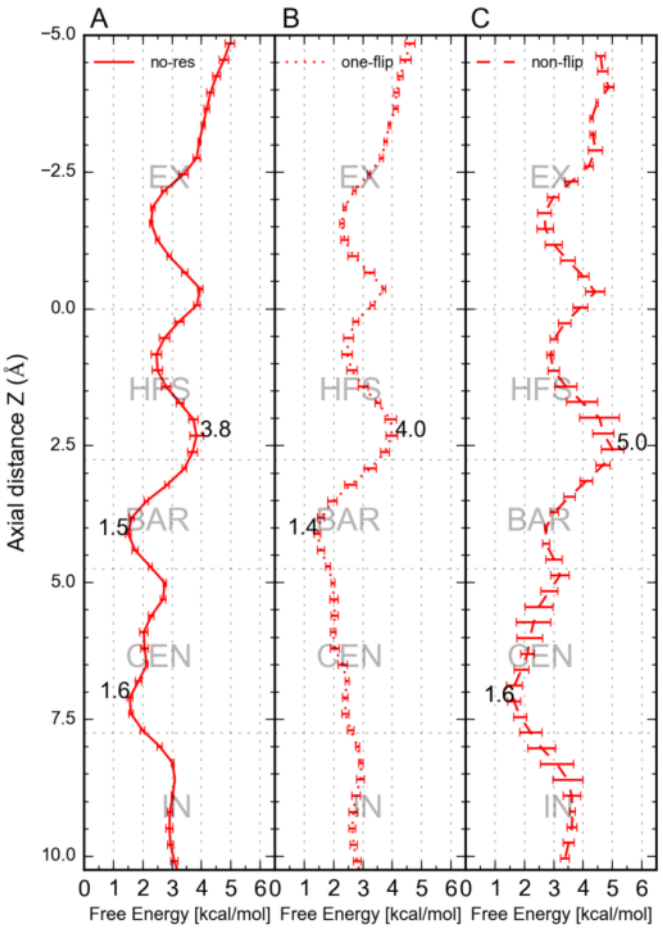

Figure 9. PMF comparison for outward conduction. A) PMF of the simulations without restraints of E53 is depicted as solid line. (B) PMF of the simulations with "one-flip" restraints. C) PMF of the simulations with "non-flip" restraints. The largest free energy barriers in each figure are labeled by terminal peaks and wells. Error estimations shown in the figure are S.E.M.
doi:10.1371/journal.pcbi.1003746.g009

different rates depending on the configurations of the E53 side chain. The highest efflux rate was observed in our "one-flip" simulations and the lowest rate with all four glutamic acid side chains restrained to an outward-facing conformation (Figure 8B). PMF calculations further confirmed that the energy barrier for outward conduction increased from 2.3 kcal/mol to 3.4 kcal/mol when the flipping conformation is prohibited (Figure 9C). That indicates that this flipping conformation provides direct coordination for Na^+ ions, which lowers the energy barrier and aids outward conduction.

A simulation study published [30] after the submission of this manuscript, indicates that the SF dynamics, especially the side chain conformational changes of the EEEE locus in the SF, may lead to the conformational changes of the cavity lining helix on the μs timescale, subsequently initiating slow inactivation in Na_V channels. We hypothesize that the E53 dynamics under depolarizing potentials uncovered in this study provide further insights into slow inactivation, especially the fast slow inactivation for prokaryotic species during action potentials. When the membrane potential depolarizes, the probability of Na^+ outward transitions increases. As a result, the inactivation probability of the channel is increased probably due to a series of conformational changes starting from the EEEE locus in the SF.

A general limitation of current force fields is that the simulated linear current–voltage regime can only be achieved at higher membrane potentials compared to experimental conditions, resulting from the large electrostatic barriers in the transmembrane region [31,32]. It should be noted that the computational electrophysiology simulations in this study were not done at constant membrane potentials (565±126 mV). This may result from the movement of the ions inside the channels and the fluctuation of the ions in the aqueous compartments (Figure 2A and B). However, a single ion permeation event under physiological conditions will also exist as a non-equilibrium process. Thus, to which extent, current simulation methods resemble ion channels' electrophysiology needs to be further validated. In addition, inaccuracies in the interaction parameters (from the forcefield) between ions and surrounding atoms could also

influence the conduction rates [33]. Thus, further structural and computational studies (including optimized strategies for ion interaction with surrounding atoms and polarizable force fields with different lipid species) will be required to further investigate the conformational changes of the SF under different electrochemical drives and the influence of different protonation states of the EEEE locus. In addition, experimental validation is essential to further uncover the structural determinants and the importance of the protonation states of the EEEE locus on ion conductance and selectivity.

Summarizing, our simulations, using applied membrane potentials, reveal different conduction mechanisms for ion inward and outward transitions respectively. An inward facing conformation (flip) of one glutamic acid side chain in the SF would reduce the energy barrier for ion outward transition by providing direct coordination with interacting Na^+ ions. This local change can provide insights into the slow inactivation of Na_V channels as suggested by Boiteux et al [30] during an action potential, when the membrane potential is depolarized.

Methods

MD simulations

The coordinates of Na_VMs (PDB Entry: 4F4L; Resolution: 3.49 Å) [7] with a conductive pore gate were used. The symmetric tetrameric structure consists of residues 8 to 94. All charged residues were treated keeping their charge states at physiological pH 7.4. In order to investigate ion conductance under two opposite membrane potentials, we used the computational electrophysiology method developed by Kutzner et al. [27] with a double-bilayer scheme. Each bilayer leaflet consists of 242 1-palmitoyl-2-oleoyl-sn-glycero-3-phosphocholine (POPC) lipids encompassing the protein structure, solvated with 500 mM NaCl solution. The system was then duplicated in the Z direction (pore axis). The virtual-site model was adopted for hydrogen atoms [34].

MD simulations were performed with Gromacs version 4.5.5-dev [35,36]. Simulations were carried out with the AMBER99sb [37] all atom force field, POPC lipids parameter were taken from Berger et al. [29,38] with the TIP3P water model [39]. All covalent bonds were constrained using the LINCS algorithm [40], allowing for an integration time step of 4 fs with virtual sites. A 10 Å cutoff was adopted for calculating short-range electrostatic interactions and the Particle Mesh Ewald [41] summation was used for calculating long-range electrostatic interactions. The corrected monovalent ion Lennard-Jones parameters for the amber forcefield [42] were implemented in this study and the vdW interactions were calculated with a cutoff of 10 Å. The Nose-Hoover thermostat [43,44] and the semi-isotropic Parrinello-Rahman barostat algorithm [45] was used to maintain simulation temperature and pressure constantly at 300 K and 1 bar, respectively.

Prior to MD simulations, 3000 conjugate gradient energy-minimization steps were performed, followed by 5 ns equilibration in order to fully solvate mobile water and lipids around the restrained protein with a force constant of 1000 kJ/mol/nm^2 on all heavy atoms. Hereafter, an equal number of Na^+ ions and a net difference of 4 e of Cl^- across each lipid bilayer between the central electrolyte bath and the two outer ones were sustained during the simulation by a swapping mechanism [27]. In this scheme, a new form of Poisson equation [46] was adopted to derive the potential profile as a function of system length (z). The well-defined transmembrane voltage across each lipid patch was directly assessed by twice integration of this sustained charge density differences between the central electrolyte bath and the two outer ones [27]. In our simulations, depolarized and hyperpolarized membrane potentials were calculated as $\Delta V = 565 \pm 126$ mV (Figure 2). Harmonic restraints (1 kcal/mol/Å^2) were exerted on the α-carbon atoms of the TM helices (S5 and S6) throughout the simulations to maintain the open configuration in the absence of the voltage-sensing domain as suggested by Ulmschneider et al. [22]. Four times 500 ns MD simulations were performed; the first 100 ns were treated as equilibration. Simulation trajectories were saved every 100 ps; as a result, 4000 snapshots (analyzing windows) were recorded for analyzing data. Three repeated 500 ns simulations (400 ns were adopted for analysis) with only ions neutralizing the system and no ions in the SF ("no salt") were performed as control to investigate the influence of the membrane potential on the E53 side chain dynamics. In this setup, only ions used to generate the charge imbalance and neutralize the net charge were kept. Further, four repeated 300 ns simulation (200 ns were adopted for analysis) for "non-flip" and "one-flip" configurations respectively were carried out, where the dihedral restraints were applied on the χ_2 dihedral of E53 for all four subunits with a force constant of 500 kcal/mol/rad^2. This allows dynamic ranges of $56 \pm 10^\circ$ for "one-flip" configuration and $288 \pm 10^\circ$ for "non-flip" configuration of the χ_2 angle.

Ionic binding modes

The total number of ions (i) which completed their conduction in the SF were analyzed (i = 158, from four inward simulations; and i = 79 from four outward simulations). All snapshots of the probe ions (yellow) and coupling ions in the SF (blue) were rendered for five different interaction sites (S_{EX}, S_{HFS}, S_{BAR}, S_{CEN} and S_{IN}). For sites S_{HFS}, S_{BAR} and S_{CEN}, the side chain isomerization states were separated into flipped and non-flipped categories and analyzed. For flipped ones, all four protein chains and the relative ion positions were aligned to chain A to achieve a better representation of the ionic binding patterns. Two probability parameters Pi and Pt were calculated to characterize the influence of E53 dynamics on ion conduction for these three sites. Pi = (Fi/i)*100%, where Fi denotes the number of ions which generated at least one E53 flipping event during their permeation through each site. Pt = Ft/Tt*100%, where Ft denotes the number of snapshots where E53 flipped when the probe ions traversed each site and Tt denotes the total number of snapshots when the probe ions traversed each site.

Potential of mean force (PMF)

The 1-D potential of mean force profile of the ions under membrane potentials were calculated by taking the logarithm of the Na^+ probability distribution along the channel axis (z) in the SF region, according to $G(z) = -k_BT \ln [p(R_i)]$, where k_B is the Boltzmann constant, T is the temperature, and $p(R_i)$ is the probability distribution of the probe ions. 100 bins were used to achieve a bin width of 0.15 Å depicting the details of the profile. Error bars are S.E.M. from four different simulations.

Supporting Information

Figure S1 Cumulative ion flux counts with flip counts as a function of time from simulation 1 without dihedral restrains of E53. A) & C) Ion flux counts through the SF and flipping counts of E53 over 400 ns trajectory of inward simulation (color: blue). B) & D) Ion flux counts through the SF and flipping counts of E53 in over 400 ns trajectory of outward simulation (color: red).
(TIFF)

Figure S2 Cumulative ion flux counts with flip counts as a function of time from simulation 2 without dihedral restrains of E53. A) & C) Ion flux counts through the SF and flipping counts of E53 over 400 ns trajectory of inward simulation (color: blue). B) & D) Ion flux counts through the SF and flipping counts of E53 in over 400 ns trajectory of outward simulation (color: red).
(TIFF)

Figure S3 Cumulative ion flux counts with flip counts as a function of time from simulation 3 without dihedral restrains of E53. A) & C) Ion flux counts through the SF and flipping counts of E53 over 400 ns trajectory of inward simulation (color: blue). B) & D) Ion flux counts through the SF and flipping counts of E53 in over 400 ns trajectory of outward simulation (color: red).
(TIFF)

Figure S4 Cumulative ion flux counts with flip counts as a function of time from simulation 4 without dihedral restrains of E53. A) & C) Ion flux counts through the SF and flipping counts of E53 over 400 ns trajectory of inward simulation (color: blue). B) & D) Ion flux counts through the SF and flipping counts of E53 in over 400 ns trajectory of outward simulation (color: red).
(TIFF)

Figure S5 Hydration shell of the simulations without dihedral restrains of E53. (A) Oxygen coordination numbers in the first hydration shell for inward sodium conduction (Oxygen atoms closer than 3.0 Å to Na^+ were considered coordinating atoms): the total coordination number is depicted in grey; water oxygens are depicted as blue lines. Protein backbone oxygens are shown in green. E53 side chain oxygens are colored red. B) Coordination oxygen atoms numbers for outward sodium conduction.
(TIFF)

Movie S1 The movie shows the double bilayer simulation scheme (400 ns).
(MP4)

Movie S2 A ''flipped'' trajectory clip showing one example conduction event from an outward simulation. Two opposite subunits are shown as cyan sticks for clarity. The E53 side chains are highlighted in yellow. Sodium ions are shown in yellow, except for Na^+ ions in the SF, which are colored in different colors. The water molecules within 3 Å of these ions are represented as sticks to depict the hydration shell.
(MP4)

Acknowledgments

We thank Tobias Linder and Eva-Maria Zangerl for helpful discussions and critical reading of the manuscript. The computational results presented have been achieved using the Vienna Scientific Cluster (VSC).

Author Contributions

Conceived and designed the experiments: SK ASW. Performed the experiments: SK. Analyzed the data: SK ENT ASW. Contributed reagents/materials/analysis tools: ENT. Wrote the paper: SK ASW.

References

1. Hille B (2001) Ion channels of excitable membranes. Sinauer. 814 p.
2. George AL (2005) Inherited disorders of voltage-gated sodium channels. J Clin Invest 115: 1990–1999. doi:10.1172/JCI25505.
3. Catterall WA (2010) Ion Channel Voltage Sensors: Structure, Function, and Pathophysiology. Neuron 67: 915–928. doi:10.1016/j.neuron.2010.08.021.
4. Payandeh J, Scheuer T, Zheng N, Catterall WA (2011) The crystal structure of a voltage-gated sodium channel. Nature 475: 353–358. doi:10.1038/nature10238.
5. Zhang X, Ren W, DeCaen P, Yan C, Tao X, et al. (2012) Crystal structure of an orthologue of the NaChBac voltage-gated sodium channel. Nature 486: 130–134. doi:10.1038/nature11054.
6. Payandeh J, El-Din TMG, Scheuer T, Zheng N, Catterall WA (2012) Crystal structure of a voltage-gated sodium channel in two potentially inactivated states. Nature 486: 135–139. doi:10.1038/nature11077.
7. McCusker EC, Bagnéris C, Naylor CE, Cole AR, D'Avanzo N, et al. (2012) Structure of a bacterial voltage-gated sodium channel pore reveals mechanisms of opening and closing. Nat Commun 3: 1102. doi:10.1038/ncomms2077.
8. Bagnéris C, DeCaen PG, Hall BA, Naylor CE, Clapham DE, et al. (2013) Role of the C-terminal domain in the structure and function of tetrameric sodium channels. Nat Commun 4. Available: http://www.nature.com/ncomms/2013/130919/ncomms3465/full/ncomms3465.html. Accessed 13 December 2013.
9. Shaya D, Findeisen F, Abderemane-Ali F, Arrigoni C, Wong S, et al. (2014) Structure of a Prokaryotic Sodium Channel Pore Reveals Essential Gating Elements and an Outer Ion Binding Site Common to Eukaryotic Channels. J Mol Biol 426: 467–483. doi:10.1016/j.jmb.2013.10.010.
10. Tang L, Gamal El-Din TM, Payandeh J, Martinez GQ, Heard TM, et al. (2014) Structural basis for Ca2+ selectivity of a voltage-gated calcium channel. Nature 505: 56–61. doi:10.1038/nature12775.
11. Yue L, Navarro B, Ren D, Ramos A, Clapham DE (2002) The cation selectivity filter of the bacterial sodium channel, NaChBac. J Gen Physiol 120: 845–853.
12. Eisenman G, Horn R (1983) Ionic selectivity revisited: The role of kinetic and equilibrium processes in ion permeation through channels. J Membr Biol 76: 197–225. doi:10.1007/BF01870364.
13. Carnevale V, Treptow W, Klein ML (2011) Sodium Ion Binding Sites and Hydration in the Lumen of a Bacterial Ion Channel from Molecular Dynamics Simulations. J Phys Chem Lett 2: 2504–2508. doi:10.1021/jz2011379.
14. Corry B, Thomas M (2011) Mechanism of Ion Permeation and Selectivity in a Voltage Gated Sodium Channel. J Am Chem Soc 134: 1840–1846. doi:10.1021/ja210020h.
15. Furini S, Domene C (2012) On Conduction in a Bacterial Sodium Channel. PLoS Comput Biol 8: e1002476. doi:10.1371/journal.pcbi.1002476.
16. Qiu H, Shen R, Guo W (2012) Ion solvation and structural stability in a sodium channel investigated by molecular dynamics calculations. Biochim Biophys Acta BBA - Biomembr 1818: 2529–2535. doi:10.1016/j.bbamem.2012.06.003.
17. Ke S, Zangerl E-M, Stary-Weinzinger A (2013) Distinct interactions of Na+ and Ca2+ ions with the selectivity filter of the bacterial sodium channel NaVAb. Biochem Biophys Res Commun 430: 1272–1276. doi:10.1016/j.bbrc.2012.12.055.
18. Zhang X, Xia M, Li Y, Liu H, Jiang X, et al. (2013) Analysis of the selectivity filter of the voltage-gated sodium channel NavRh. Cell Res 23: 409–422. doi:10.1038/cr.2012.173.
19. Xia M, Liu H, Li Y, Yan N, Gong H (2013) The Mechanism of Na+/K+ Selectivity in Mammalian Voltage-Gated Sodium Channels Based on Molecular Dynamics Simulation. Biophys J 104: 2401–2409. doi:10.1016/j.bpj.2013.04.035.
20. Corry B (2013) Na(+)/Ca(2+) selectivity in the bacterial voltage-gated sodium channel NavAb. PeerJ 1: e16. doi:10.7717/peerj.16.
21. Stock L, Delemotte L, Carnevale V, Treptow W, Klein ML (2013) Conduction in a Biological Sodium Selective Channel. J Phys Chem B 117: 3782–3789. doi:10.1021/jp401403b.
22. Ulmschneider MB, Bagnéris C, McCusker EC, DeCaen PG, Delling M, et al. (2013) Molecular dynamics of ion transport through the open conformation of a bacterial voltage-gated sodium channel. Proc Natl Acad Sci: 201214667. doi:10.1073/pnas.1214667110. [epub ahead of print]
23. Chakrabarti N, Ing C, Payandeh J, Zheng N, Catterall WA, et al. (2013) Catalysis of Na+ permeation in the bacterial sodium channel NaVAb. Proc Natl Acad Sci: 201309452. doi:10.1073/pnas.1309452110. [epub ahead of print]
24. Furini S, Domene C (2013) K+ and Na+ Conduction in Selective and Nonselective Ion Channels Via Molecular Dynamics Simulations. Biophys J 105: 1737–1745. doi:10.1016/j.bpj.2013.08.049.
25. Bernèche S, Roux B (2005) A Gate in the Selectivity Filter of Potassium Channels. Structure 13: 591–600. doi:10.1016/j.str.2004.12.019.
26. Cuello LG, Jogini V, Cortes DM, Perozo E (2010) Structural mechanism of C-type inactivation in K+ channels. Nature 466: 203–208.
27. Kutzner C, Grubmüller H, de Groot BL, Zachariae U (2011) Computational Electrophysiology: The Molecular Dynamics of Ion Channel Permeation and Selectivity in Atomistic Detail. Biophys J 101: 809–817.
28. Amaral C, Carnevale V, Klein ML, Treptow W (2012) Exploring conformational states of the bacterial voltage-gated sodium channel NavAb via molecular dynamics simulations. Proc Natl Acad Sci 109: 21336–21341. doi:10.1073/pnas.1218087109.

29. Cordomí A, Caltabiano G, Pardo L (2012) Membrane Protein Simulations Using AMBER Force Field and Berger Lipid Parameters. J Chem Theory Comput 8: 948–958. doi:10.1021/ct200491c.
30. Boiteux C, Vorobyov I, Allen TW (2014) Ion conduction and conformational flexibility of a bacterial voltage-gated sodium channel. Proc Natl Acad Sci 111: 3454–3459. doi:10.1073/pnas.1320907111.
31. Bockmann RA, Hac A, Heimburg T, Grubmuller H (2003) Effect of Sodium Chloride on a Lipid Bilayer. Biophys J 85: 1647–1655.
32. Jensen MØ, Jogini V, Eastwood MP, Shaw DE (2013) Atomic-level simulation of current–voltage relationships in single-file ion channels. J Gen Physiol 141: 619–632. doi:10.1085/jgp.201210820.
33. Luo Y, Roux B (2010) Simulation of Osmotic Pressure in Concentrated Aqueous Salt Solutions. J Phys Chem Lett 1: 183–189. doi:10.1021/jz900079w.
34. Feenstra KA, Hess B, Berendsen HJC (1999) Improving efficiency of large time-scale molecular dynamics simulations of hydrogen-rich systems. J Comput Chem 20: 786–798. doi:10.1002/(SICI)1096-987X(199906)20:8<786::AID-JCC5>3.0.CO;2-B.
35. Hess B, Kutzner C, Van Der Spoel D, Lindahl E (2008) GROMACS 4: Algorithms for highly efficient, load-balanced, and scalable molecular simulation. J Chem Theory Comput 4: 435–447.
36. Van Der Spoel D, Lindahl E, Hess B, Groenhof G, Mark AE, et al. (2005) GROMACS: fast, flexible, and free. J Comput Chem 26: 1701.
37. Hornak V, Abel R, Okur A, Strockbine B, Roitberg A, et al. (2006) Comparison of multiple Amber force fields and development of improved protein backbone parameters. Proteins 65: 712–725. doi:10.1002/prot.21123.
38. Berger O, Edholm O, Jahnig F (1997) Molecular dynamics simulations of a fluid bilayer of dipalmitoylphosphatidylcholine at full hydration, constant pressure, and constant temperature. Biophys J 72: 2002–2013.
39. Jorgensen WL, Chandrasekhar J, Madura JD, Impey RW, Klein ML (1983) Comparison of simple potential functions for simulating liquid water. J Chem Phys 79: 926–935. doi:10.1063/1.445869.
40. Hess B, Bekker H, Berendsen HJC, Fraaije JGEM (1997) LINCS: A linear constraint solver for molecular simulations. J Comput Chem 18: 1463–1472. doi:10.1002/(SICI)1096-987X(199709)18:12<1463::AID-JCC4>3.0.CO;2-H.
41. Darden T, York D, Pedersen L (1993) Particle mesh Ewald: An N log (N) method for Ewald sums in large systems. J Chem Phys 98: 10089–10089.
42. Joung IS, Cheatham III TE (2008) Determination of alkali and halide monovalent ion parameters for use in explicitly solvated biomolecular simulations. J Phys Chem B 112: 9020–9041.
43. Nose S, Nose S (1984) A unified formulation of the constant temperature molecular-dynamics methods. J Chem Phys 81: 511–519. doi:10.1063/1.447334.
44. Hoover, William G., Hoover WG (1985) Canonical dynamics: Equilibrium phase-space distributions. Phys Rev A 31: 1695–1697. doi:10.1103/PhysRevA.31.1695.
45. Martoňák R, Laio A, Parrinello M (2003) Predicting crystal structures: The Parrinello-Rahman method revisited. Phys Rev Lett 90: 75503.
46. Sachs JN, Crozier PS, Woolf TB (2004) Atomistic simulations of biologically realistic transmembrane potential gradients. J Chem Phys 121: 10847–10851. doi:10.1063/1.1826056.

Figure S1

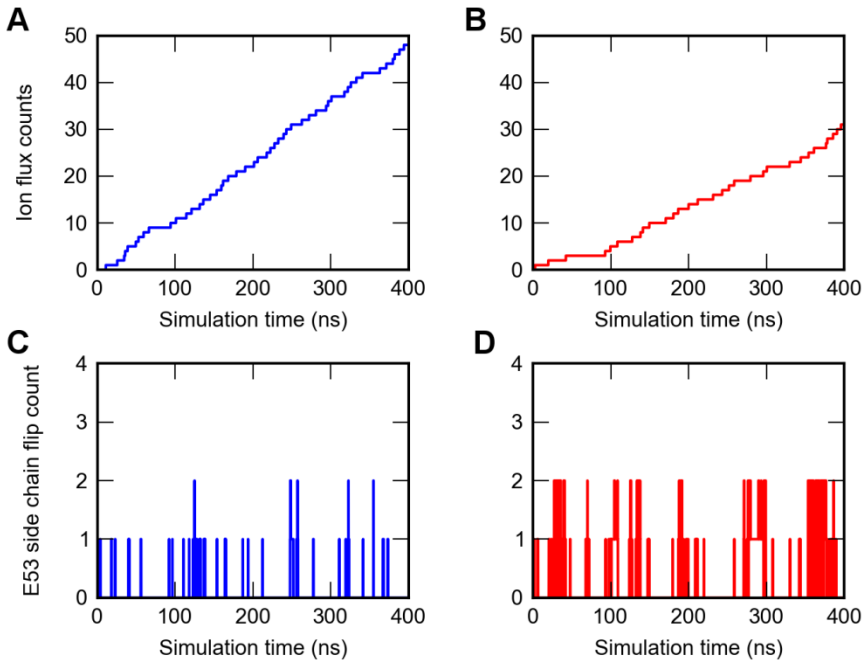
A
B
C
D
Ion flux counts
E53 side chain flip count
Simulation time (ns)
Simulation time (ns)
Simulation time (ns)
Simulation time (ns)
0
10
20
30
40
50
0
1
2
3
4
0
100
200
300
400

Figure S2

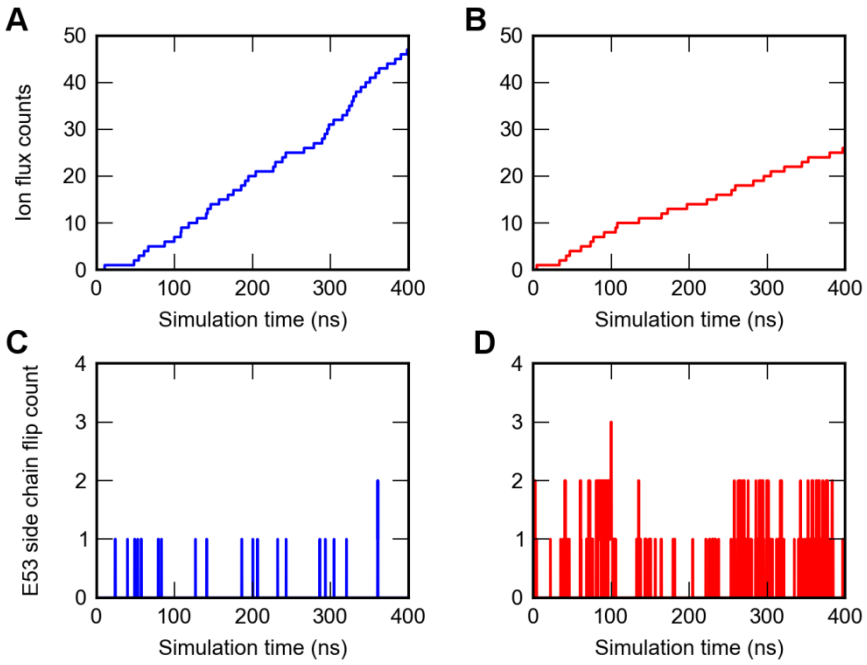
A
B
C
D
Ion flux counts
E53 side chain flip count
Simulation time (ns)
Simulation time (ns)
Simulation time (ns)
Simulation time (ns)
0
10
20
30
40
50
0
1
2
3
4
0
100
200
300
400

Figure S3

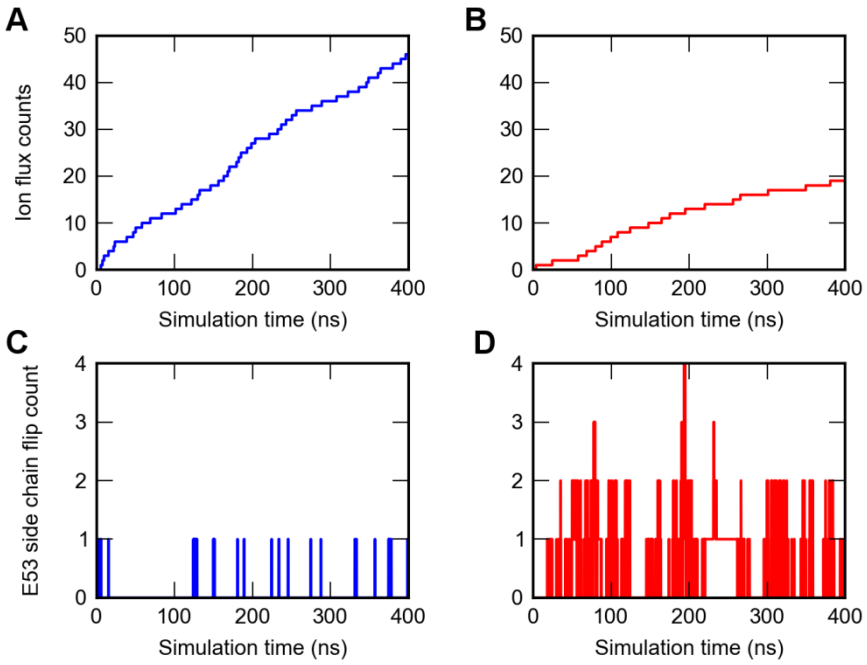
A
B
C
D
Ion flux counts
E53 side chain flip count
Simulation time (ns)
Simulation time (ns)
Simulation time (ns)
Simulation time (ns)
0
10
20
30
40
50
0
1
2
3
4
0
100
200
300
400

Figure S4

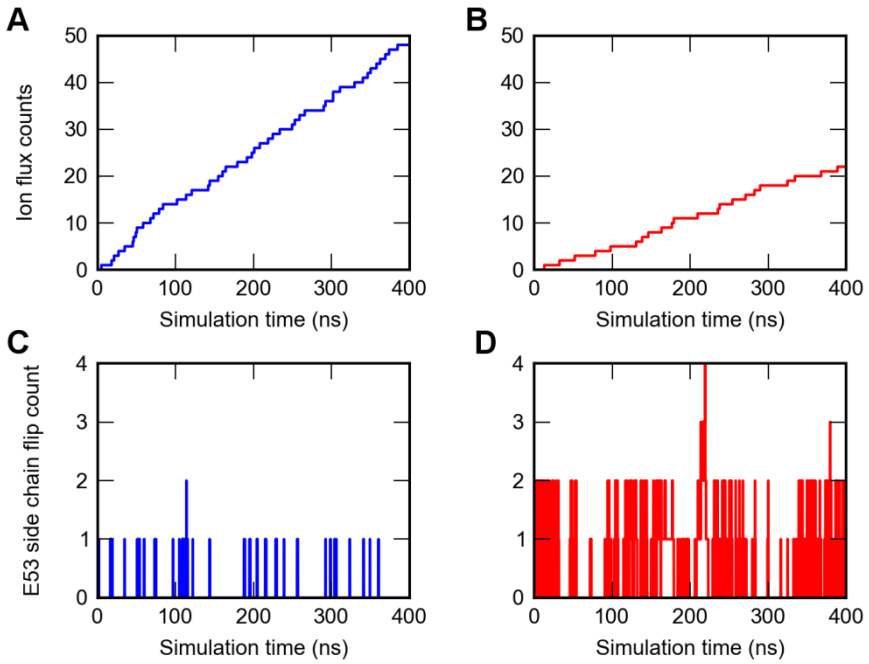
A
B
C
D
Ion flux counts
E53 side chain flip count
Simulation time (ns)
Simulation time (ns)
Simulation time (ns)
Simulation time (ns)
0
10
20
30
40
50
0
1
2
3
4
0
100
200
300
400

Figure S5

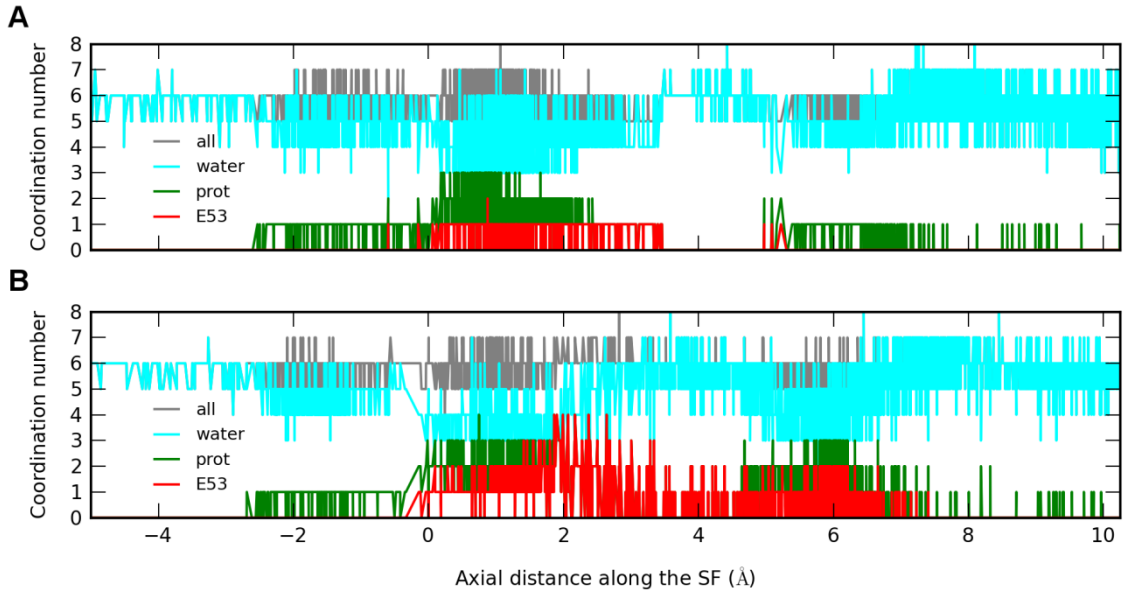

Movie S1 & S2:

http://journals.plos.org/ploscompbiol/article?id=10.1371/journal.pcbi.1003746#s5

4.3 Exploring the Structure of the Voltage-gated Na^+ Channel by an Engineered Drug Access Pathway to the Receptor Site for Local Anesthetics

Peter Lukacs, Vaibhavkumar S. Gawali, Rene Cervenka, Song Ke, Xaver Koenig, Lena Rubi, Touran Zarrab,Karlheinz Hilber, Anna Stary-Weinzinger, and Hannes Todt

The Journal of Biological Chemistry

2014, 289:21770-21781

THE JOURNAL OF BIOLOGICAL CHEMISTRY VOL. 289, NO. 31, pp. 21770–21781, August 1, 2014

Exploring the Structure of the Voltage-gated Na^+ Channel by an Engineered Drug Access Pathway to the Receptor Site for Local Anesthetics*

Received for publication, April 28, 2014, and in revised form, June 17, 2014 Published, JBC Papers in Press, June 19, 2014, DOI 10.1074/jbc.M113.541763

Peter Lukacs[‡], Vaibhavkumar S. Gawali[‡], Rene Cervenka[‡], Song Ke[§], Xaver Koenig[‡], Lena Rubi[‡], Touran Zarrabi[‡], Karlheinz Hilber[‡], Anna Stary-Weinzinger[§], and Hannes Todt[‡1]

From the [‡]Department of Neurophysiology and Neuropharmacology, Center for Physiology and Pharmacology, Medical University of Vienna, 1090 Vienna, Austria and [§]Department of Pharmacology and Toxicology, University of Vienna, Althanstrasse 14, UZA 2, A-1090 Vienna, Austria

Background: Currently the structure of eukaryotic voltage-gated Na^+ channels (VGSCs) is predicted from available prokaryotic VGSC crystals.
Results: In a mammalian VGSC, the predicted position of a multifunctional tryptophan in the external vestibule enabled design of a second conduction pathway.
Conclusion: External parts of pro- and eukaryotic VGSCs are structurally similar.
Significance: Engineered external drug access pathways may allow development of novel VGSC modulators.

Despite the availability of several crystal structures of bacterial voltage-gated Na^+ channels, the structure of eukaryotic Na^+ channels is still undefined. We used predictions from available homology models and crystal structures to modulate an external access pathway for the membrane-impermeant local anesthetic derivative QX-222 into the internal vestibule of the mammalian $rNa_V1.4$ channel. Potassium channel-based homology models predict amino acid Ile-1575 in domain IV segment 6 to be in close proximity to Lys-1237 of the domain III pore-loop selectivity filter. The mutation K1237E has been shown previously to increase the diameter of the selectivity filter. We found that an access pathway for external QX-222 created by mutations of Ile-1575 was abolished by the additional mutation K1237E, supporting the notion of a close spatial relationship between sites 1237 and 1575. Crystal structures of bacterial voltage-gated Na^+ channels predict that the side chain of $rNa_V1.4$ Trp-1531 of the domain IV pore-loop projects into the space between domain IV segment 6 and domain III pore-loop and, therefore, should obstruct the putative external access pathway. Indeed, mutations W1531A and W1531G allowed for exceptionally rapid access of QX-222. In addition, W1531G created a second nonselective ion-conducting pore, bypassing the outer vestibule but probably merging into the internal vestibule, allowing for control by the activation gate. These data suggest a strong structural similarity between bacterial and eukaryotic voltage-gated Na^+ channels.

Voltage-gated Na^+ channels (VGSCs)[2] are membrane proteins responsible for initiation of action potentials in nerve, skeletal muscle, and heart. In terms of structure, these proteins are believed to be formed by four homologous domains (DI–DIV), each of them containing six transmembrane helical segments. The first four segments form the voltage sensor. Segment 5 (S5), segment 6 (S6), and the pore-loop (P-loop) between them give rise to the ion-conducting pore. P-loops form an inverted conelike structure referred to as the outer vestibule that contains the selectivity filter. Although these structural features can be found in the recently published crystal structures of several bacterial VGSCs (1–4), the structure of eukaryotic VGSC remains unknown. Unlike the eukaryotic VGSCs, the bacterial channels are homotetramers, which is especially important when structural considerations regarding the region of the selectivity filter are concerned. The eukaryotic selectivity filter is composed of four different amino acids, each contributed by one of the P-loops of domains I–IV ("DEKA motif"; 5–8). By contrast, in the bacterial VGSCs, each monomer contributes the same amino acid to the selectivity filter. In this work, we explored the applicability of the available bacterial VGSC structures for predicting routes of drug access in a region close to the selectivity filter of the mammalian $rNa_V1.4$ channel. Specifically, we examined the modulation of an external access pathway (EAP) for local anesthetic drugs to their binding site in the internal vestibule. Local anesthetic drugs containing a tertiary amino group are considered to reach this binding site either via the membrane or via the inner channel pore (9). Conversely, quaternary amine local anesthetics are membrane-impermeant and have to enter the channel via the inner pore (10, 11). However, in the native cardiac channel (12, 13) and in several mutant VGSCs, EAPs for permanently charged local anesthetic drugs have been found (14–19). These EAPs have provided insights into the three-dimensional arrangement of the channel protein (20).

* This study was supported by Austrian Science Fund (FWF) Grants P210006-B11 and W1232-B11.
[1] To whom correspondence should be addressed. Tel.: 431-40160-31250; Fax: 431-40160-931300; E-mail: hannes.todt@meduniwien.ac.at.
[2] The abbreviations used are: VGSC, voltage-gated Na^+ channel; DI–DIV, domains I–IV; P-loop, pore-loop; IIIP, domain III P-loop; S5, segment 5; S6, segment 6; EAP, external access pathway; TTX, tetrodotoxin; IVS6, domain IV S6; TMA, tetramethylammonium; TEA, tetraethylammonium; MD, molecular dynamics; rNa_V, rat Na_V; hNa_V, human Na_V.

In the first part of this study, we explored an EAP created by a mutation of Ile-1575 in $rNa_V1.4$ (18), originally reported in $rNa_V1.2$ (I1760A; Ref. 14). In the first structural homology models of the mammalian VGSC developed by Lipkind and Fozzard (21) and Tikhonov and Zhorov (22), Ile-1575 of the domain IV S6 (IVS6) is located immediately lateral from the amino acid Lys-1237 of the domain III P-loop (IIIP), which is part of the selectivity filter of the channel (Fig. 1, *A* and *B*). The mutation K1237E has been shown to increase the diameter of the selectivity filter, perhaps by a lateral "swing out" of the IIIP (23–25). If the EAP is located between the IIIP and the IVS6, then the lateral movement of Glu-1237 may obstruct the access for QX-222. Here we refer to this idea as the swing out hypothesis.

Fig. 1 shows a comparison of the selectivity filter region predicted by the homology models based on the crystal structures of the bacterial K^+ channels KcsA (Fig. 1*A* and Ref. 21) and MthK (Fig. 1*B* and Ref. 22), the recently published crystal structure of Na_VRh (Fig. 1*C* and Ref. 4), and a revised homology model (26) based on the structure of the bacterial VGSC Na_VAb (Fig. 1*D* and Ref. 1). Interestingly, with the K^+ channel-based models, the side chains of Lys-1237 of the domain III selectivity filter (*green*) and of Ile-1575 of the IVS6 (*yellow*) are in close proximity to each other (Fig. 1, *A* and *B*). Conversely, in the Na_VAb-based model, Lys-1237 and Ile-1575 are separated by a tryptophan side chain of the domain IV P-loop (homologous to Trp-1531 in rNav1.4; Fig. 1, *C* and *D*, *cyan*). This difference from the earlier K^+ channel-based models is due to the fact that in all bacterial VGSCs crystallized so far (1, 3, 4) the side chain of this tryptophan is directed toward the space between the S6 helix and the pore helix of the previous repeat (Fig. 1, *C* and *D*). Hence, if the EAP is located at the region between the domain III selectivity filter and the IVS6, then the VGSC-based crystal structures predict that Trp-1531 may obstruct this access pathway. We will refer to this idea as the "Trp-lock" hypothesis. We found that predictions based on the two mentioned hypotheses are consistent with our experimental data. Furthermore, we used a homology model based upon the recently published structure of Na_VRh to define the molecular localization of the experimentally explored EAP.

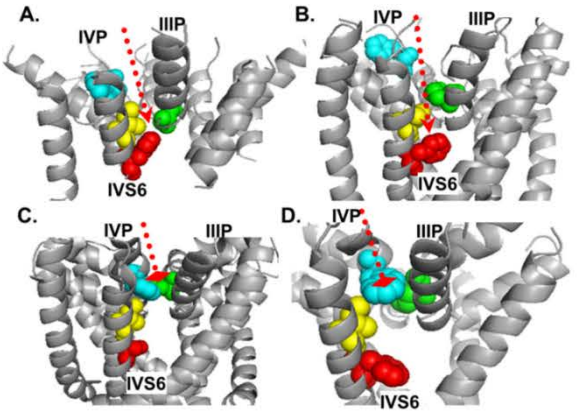

FIGURE 1. **Structure of the external access pathway.** The proposed molecular arrangement of crucial amino acids involved in access and binding of QX-222 is shown. *A* and *B*, homology models by Lipkind and Fozzard (21) and Tikhonov and Zhorov (22), respectively, based on bacterial K^+ channels KcsA and MthK. Amino acids Lys-1237 (*green*), Trp-1531 (*cyan*), Ile-1575 (*yellow*), and Phe-1575 (*red*) of $rNa_V1.4$ are homologous to the positions Ser-180, Trp-182, Ile-204, and Ser-208 in Na_VRh. S5 segments are omitted in *A* and *D* as they were not included in the published models (22, 26). A potential EAP between the IIIP and the IVS6 can be identified (*red dotted arrow*). The EAP is lined by amino acids Lys-1237 (*green*), Ile-1575 (*yellow*), and Trp-1531 (*cyan*). Phe-1579 (*red*) in the internal vestibule is the major determinant of binding of local anesthetic drugs. *C*, Na_VRh crystal structure (4). The side chain of residue Trp-182 (*cyan*) has a different orientation than the homologous side chain (Trp-1531) in $rNa_V1.4$ as shown in *A* and *B*. Trp-182 is inserted between the selectivity filter of the previous domain (Ser-180; *green*) and S6 of the same domain (Ile-204; *yellow*). Although not shown here, a similar conformational arrangement is present in the crystal structures of Na_VAb and Na_VMS (1, 3). Consequently, in Na_VRh, the side chain of Trp-182 is expected to obstruct the access of QX-222 to the internal vestibule. *D*, revised homology model by Tikhonov and Zhorov (26). The position of the side chain of Trp-1531 in $Na_V1.4$ is similar to that of its homologue Trp-182 in Na_VRh, thus obstructing the potential EAP.

EXPERIMENTAL PROCEDURES

Site-directed Mutagenesis—Detailed methods for the mutagenesis have been published previously (16, 27, 28).

Transfection Procedure—tsA201 cells were grown in Dulbecco's modified Eagle's medium supplemented with 10% fetal bovine serum and 20 units/ml penicillin, and 20 units/ml streptomycin (Invitrogen). Cells were maintained at 37 °C in a humid atmosphere containing 5% CO_2. Mixture of plasmids coding 1.5 μg of $rNa_V1.4$ α subunit, 0.2 μg of VGSC β1 subunit, and 0.02 μg of enhanced GFP were transiently transfected into tsA201 cells in a 35-mm dish (Nunc, Roskilde, Denmark) using TurboFect transfection reagent (Thermo Fisher Scientific Baltics UAB, Vilnius, Lithuania) according to the manufacturer's instructions. 16 h later, cells were dissociated from the dish surface by treatment with a 0.25% trypsin solution (Invitrogen) for ~2 min, pelleted, resuspended in growth medium, and allowed to settle to the bottom of the recording chamber. Prior to recording, the growth medium was removed and changed to bath solution.

Whole-cell Patch Clamp Recording—Experiments were performed using the whole-cell patch clamp recording technique. Na^+ currents were recorded using an Axopatch 700B patch clamp amplifier (Molecular Devices, Sunnyvale, CA). Pipettes were formed from aluminosilicate glass (AF150-100-10, Science Products, Hofheim, Germany) with a P-97 horizontal puller (Sutter Instruments, Novato, CA) and had resistances between 1.5 and 2.5 megaohms when filled with the intracellular pipette solution consisting of 105 mM CsF, 10 mM NaCl, 10 mM EGTA, 10 mM HEPES. The pH was set to 7.3 with CsOH. For the experiments shown in Fig. 9*A*, Cs^+ was replaced by equimolar concentrations of tetramethylammonium (TMA) or tetraethylammonium (TEA). The bath solution consisted of 140 mM NaCl, 2.5 mM KCl, 1 mM $CaCl_2$, 1 mM $MgCl_2$, 10 mM HEPES. The pH was set to 7.4 with NaOH. For the experiments shown in Fig. 9*B*, Na^+ was replaced by equimolar concentrations of K^+, NH_4^+, and Cs^+.

Voltage clamp protocols and data acquisition were performed with pCLAMP 10.2 software (Molecular Devices) through a 16-bit analog-digital/digital-analog interface (Digidata 1440A, Molecular Devices). Data were low pass-filtered at 10 kHz (−3 db) and digitized at 100 kHz. In some experiments, QX-222 (Alomone Labs, Jerusalem, Israel) and/or tetrodotoxin (TTX; Latoxan, Valance, France) was dissolved in the intracel-

lular or extracellular solution. Drugs dissolved in the extracellular solution were applied via an OCTAFLOW drug application device (ALA Scientific Instruments Inc., Farmingdale, NY). This superfusion system permits a complete exchange of the solutions surrounding the cells under investigation within 100 ms (29). Recording was begun about 5 min after whole-cell access was attained to minimize time-dependent shifts in gating.

Voltage Clamp Protocols—Na^+ currents were elicited by 20-ms pulses to −10 mV at a rate of 2 Hz from a holding potential of −120 mV if not stated otherwise.

To assess recovery from intracellular QX-222 block, pipettes were filled with 500 μM QX-222 dissolved in the intracellular pipette solution. After break-in, cells were held at potential of −140 mV to keep channels in a closed state. After a minimum of 10 min of equilibration, a train of pulses (20-ms pulses to −10 mV at 10 Hz) was applied for 5 s to allow binding of QX-222 upon repetitive opening of the channels. Varying time intervals at a holding potential of −140 mV allowed for subsequent recovery of current amplitude. A final pulse to −10 mV tested for the residual current. Current-voltage relationships were determined by 20-ms voltage steps to various potentials between −80 and +50 mV from a holding potential of −140 mV.

Steady-state Inactivation Curves—From a holding potential of −140 mV, inactivation was induced by 50-ms-long prepulses to various potentials from −140 to 0 mV. The current available after the prepulse was tested by a 20-ms test pulse to 0 mV immediately after the prepulse. Plots of current availability as a function of prepulse potential were fitted with Equation 5.

Current-voltage relationships were recorded at a holding potential −140 mV. Currents were elicited by 20-ms-long voltage steps to various potentials from −80 to +50 mV. The currents were normalized to the respective maximum value. The data points were fitted with Equation 3 to calculate the respective reversal potential.

Data Evaluation—The time course of Na^+ current block was fitted with a single exponential function (Equation 1).

$$y = 1 - A \times (1 - \exp(-t/\tau_1)) \quad \text{(Eq. 1)}$$

where y is the normalized peak inward current, τ_1 is the time constant of block development, A is the fractional block amplitude, and t is the time from start of QX-222 perfusion. The time course of Na^+ current unblock was fitted with Equation 2.

$$y = (1 - A) + B \times (1 - \exp(-t/\tau_2)) \quad \text{(Eq. 2)}$$

where τ_2 is the unblock time constant and B is the fractional amplitude of recovery from QX-222 block with other parameters as stated above.

Current-voltage relationships were fitted with a function (Equation 3),

$$G_{max} \times (V - V_{rev}) \times (1 - (1/(1 + \exp((V - V_{0.5})/k)))) \quad \text{(Eq. 3)}$$

where V is the step potential, G_{max} is the maximum conductance, $V_{0.5}$ is the voltage at which half-maximum activation occurred, V_{rev} is the reversal potential, and k is the slope factor.

The time course of recovery from intracellular block was fitted with a double exponential function (Equation 4).

$$y = -A_1 \times (1 - \exp(-t/\tau_1)) - A_2 \times (1 - \exp(-t/\tau_2)) + C \quad \text{(Eq. 4)}$$

where y is the normalized peak inward current, t is the recovery time, τ_1 and τ_2 are the time constants of distinct components of recovery, A_1 and A_2 are the respective amplitudes, and C is the final level of recovery.

Steady-state inactivation data were fitted with a Boltzmann function (Equation 5),

$$y = 1/(1 + \exp((V - V_{1/2})/k)) \quad \text{(Eq. 5)}$$

where V is the voltage of the conditioning prepulse, $V_{1/2}$ is the voltage at which half-maximum inactivation occurred, and k is the slope factor. Curve fitting was performed using GraphPad Prism 6 (GraphPad Software, Inc., La Jolla, CA).

Statistics—Data are expressed as means ± S.E. Statistical comparisons were made using the two-tailed unpaired Student's t tests or one-way unpaired analysis of variance with Tukey's post hoc test for comparison of more than two groups. A p value <0.05 was considered as being significant. In figures and tables, the levels of significance are indicated in the following manner: *, $p < 0.05$; **, $p < 0.01$; ***, $p < 0.001$.

Structural Modeling, Molecular Dynamics (MD) Simulations, and Docking—The coordinates of the bacterial VGSC analog Na_VRh (Ref. 4; α proteobacterium HIMB114; Protein Data Bank code 4DXW; resolution, 3.05 Å) with an inactivated pore gate were used.

MD Simulations—100-ns MD simulation were performed with Gromacs (version 4.5.5-dev; Ref. 30) with 250 mM NaCl solution. All charged residues were treated to keep their charge states at physiological pH 7.4. Simulations were carried out with the AMBER99sb (31) all-atom force field. 1-Palmitoyl-2-oleoylphosphatidylcholine (lipids parameters were derived from Berger *et al.* (32) and Cordomi *et al.* (33)), and the TIP3P water model was applied (34). The simulation setups were described before (35).

The simulations were performed in wild-type and mutant Na_VRh channels. Mutant Na_VRh channels were generated in the following manner: to mimic $rNa_V1.4$ W1531G, the homologous residue of chain D, Trp-182, was mutated to a glycine. Furthermore, in Na_VRh, the amino acid homologous to Ser-1528 in rNav1.4 is Leu-179, which might impose a stronger steric hindrance for permeation of QX-222 through the potential EAP than a serine. Therefore, in the mutant Na_VRh, we also introduced the mutation L179S. The mutants were generated by PyMOL (36).

Pathway Visualization—To visualize the dimensions of the putative pathway formed by W182G/L179S mutant compared with wild-type Na_VRh, we used the program HOLE (37). The center of mass coordinates of backbone nitrogen of Gln-175 and backbone oxygen of W182G (chain D) were selected to define the entrance of the EAP. The center of mass coordinates of four equivalent positions at the gate from four subunits

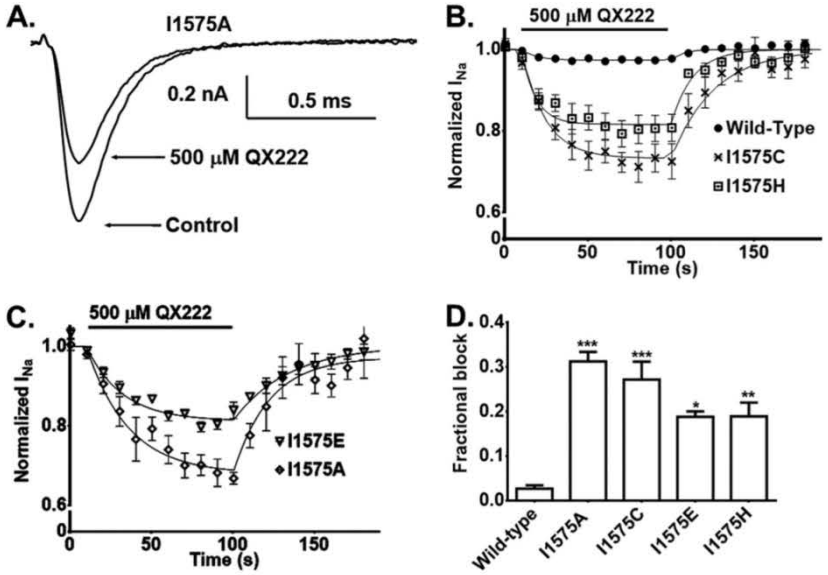

FIGURE 2. **External block by QX-222 is favored by replacement of Ile-1575 with amino acids of small size or with hydrophilic properties.** Sodium currents were evoked by depolarizing pulses at a frequency of 2 Hz (see "Experimental Procedures"). Connecting lines are fits of Equation 1 and Equation 2 to the development and the recovery from block, respectively. *A*, typical current trace under drug-free conditions and 90 s after start of superfusion with 500 μM extracellular QX-222. *B* and *C*, time course of peak inward currents during external application of QX-222. Data points represent mean values normalized to the respective maximum peak inward current (see Table 1 for details). For clarity, only values of every 20th pulse are shown. *D*, fraction of blocked currents during steady state in the tested constructs. All tested mutants at position Ile-1575 were more sensitive to block of QX-222 than wild type. *Asterisks* denote levels of significance compared with wild type (*, $p < 0.05$; **, $p < 0.01$; ***, $p < 0.001$). *Error bars* represent S.E.

(L212) were selected to determine the exit of the EAP. Then, the vector (CVECT in HOLE; Ref. 37) representing the EAP was calculated by these two coordinates. A central point (CPOINT in HOLE; Ref. 37) in EAP was defined by the center of mass coordinates of backbone oxygen of positions 179 and 204.

Model Building—In MD simulations of the mutant Na_VRh, we observed water influx behind the selectivity filter in the region previously occupied by the tryptophan side chain. Thus, we adopted a snapshot (when this region was solvated with the maximum number of water molecules) from MD as a starting point for modeling rat $Na_V1.4$ channel. Chains C and D were replaced with rat $Na_V1.4$ sequences of domains III and IV. In the model, the EAP was again visualized using the program HOLE.

Docking of QX-222—The QX-222 three-dimensional structure was taken from the PubChem home page. Docking along the EAP in the $rNa_V1.4$ model containing the mutation W1531G was performed with the program GOLD v5.2 (Cambridge Crystallographic Data Centre, Cambridge, UK) using the GOLD scoring function as described before (38). In docking, we selected two arbitrary spheres (radius, 6 Å) covering the EAP as visualized by HOLE (axial length, ~9 Å). All side chains within the spheres were treated as flexible. Within these spheres, 30 docking poses were generated.

RESULTS

Mutations at Site 1575 Open an EAP for QX-222—Using the *Xenopus laevis* expression system, replacement of Ile-1575 by alanine, cysteine, and glutamate has been shown previously to open an EAP for QX-222 (18). Our first aim was to recapitulate these studies using a mammalian expression system. Furthermore, we examined the effect of engineering a positively charged histidine to this site. As shown in Fig. 2, all tested amino acid replacements at site 1575 allowed for external access of QX-222. I1575A and I1575C produced the greatest amount of fractional block, whereas introduction of charged amino acids at this site was associated with less block (Fig. 2; $p < 0.05$ compared with I1575A).

In all constructs, block development was slow with time constants ranging from ~12 to ~27 s (Table 1). Thus, both charged and uncharged amino acids engineered to site 1575 open an access pathway for QX-222; however, access is very slow, suggesting the presence of a substantial energy barrier or steric hindrance for drug access.

Drug Access via Site 1575 Leads to the Internal Vestibule—The data in Fig. 2 suggest that mutations at site 1575 create an EAP for local anesthetics. Alternatively, mutations at this position may allow for current inhibition by external QX-222 by generating an external drug binding site. A phenylalanine in the middle of the IVS6 (Phe-1579; Fig. 1, *red*) is a major part of the internal binding site of both amphiphilic and permanently charged local anesthetics (14–16). To test whether external block by QX-222 in the mutants at site 1575 is also mediated by this phenylalanine, we generated the double mutant I1575E/F1579A. As shown in Fig. 3*A*, this construct was insensitive to external block by QX-222. This suggests that mutations at site 1575 create an access pathway to the local anesthetic binding site rather than generating a new external binding site.

TABLE 1

Fractional block, block time, and unblock time constants

Fractional block and block time constants were calculated by fitting of Equation 1 to the time course of reduction of normalized peak inward currents following the start of superfusion with QX-222. The unblock time constant was calculated by fitting of Equation 2 to the time course of increase of normalized peak inward currents following the end of superfusion with QX-222.

							−90 mV	
	I1575A ($n = 4$)	I1575C ($n = 7$)	I1575H ($n = 8$)	I1575E ($n = 4$)	W1531A ($n = 6$)	W1531G ($n = 8$)	W1531A ($n = 3$)	W1531G ($n = 4$)
Fractional block	0.31 ± 0.02	0.27 ± 0.04	0.19 ± 0.03	0.18 ± 0.01	0.18 ± 0.03	0.15 ± 0.02	0.65 ± 0.02	0.31 ± 0.03
Block time constant (s)	26.7 ± 1.6	15.2 ± 0.9	11.5 ± 0.9	22.0 ± 1.0	2.9 ± 0.4[a]	1.7 ± 0.3[a]	3.6 ± 0.1	1.1 ± 0.2
Unblock time constant (s)	22.0 ± 1.6	18.1 ± 1.2	6.2 ± 0.6	33.0 ± 2.1	5.0 ± 0.5[a]	1.6 ± 0.3[a]	10.0 ± 0.4	1.5 ± 0.2

[a] $p < 0.05$ compared with respective data from I1575A.

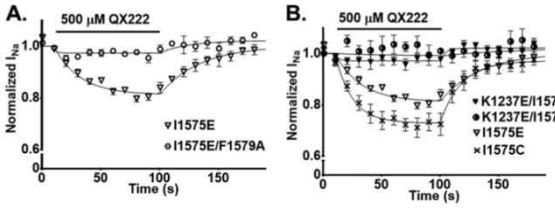

FIGURE 3. **The binding site for external QX-222 is in the internal vestibule.** Modulation of the EAP by an additional mutation in the selectivity filter and by mutations of Trp-1531 is shown. The stimulation protocol and depiction are the same as in Fig. 2*B*. *A*, residue Phe-1579 is considered a major determinant of binding of local anesthetics to the internal vestibule. Here we show that the external block by QX-222 in I1575E is abolished by the additional mutation F1579A. In the double mutant I1575E/F1579A channel, QX-222 block was reduced to the wild-type level (by 0.03 ± 0.01 ($n = 4$) *versus* by 0.18 ± 0.01 ($n = 5$) in I1575E; $p < 0.01$). *B*, the mutation K1237E caused a loss of selectivity for Na^+ ions and allowed for permeation of large organic cations, perhaps by a lateral swing out of the P-loop in domain III. This hypothesis is supported by the fact that block by QX-222 via the EAP in the mutants I1575E/C was abolished by the additional mutation K1237E. The fractional block was 0.03 ± 0.05 ($n = 7$) and 0.18 ± 0.01 ($n = 4$) in K1237E/I1575E and I1575E, respectively, and 0.01 ± 0.02 ($n = 5$) and 0.27 ± 0.04 ($n = 7$) in K1237E/I1575C and I1575C, respectively. Differences between the single S6 and double mutants were significant ($p \leq 0.005$). *Error bars* represent S.E.

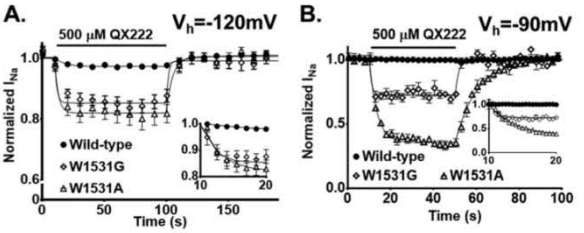

FIGURE 4. **As predicted by the Na_VAb crystal structure, mutations at site 1531 open an external access pathway with a higher access speed (*A* and *B*).** *A*, fractional block levels at steady state were significantly higher compared with wild type (Table 1). *Inset*, for a better resolution of the block development, the first 10 s of drug superfusion are shown. In the figure and the *inset*, values of every 20th pulse and every third pulse are depicted, respectively *B*, same protocol as in *A* but the holding potential was changed to −90 mV. External QX-222 resulted in a stronger current reduction with a holding potential of −90 mV than with −120 mV. Note the changed scaling of the *ordinate*. Values of every 20th pulse are depicted. *Inset*, for a better resolution of the block development, the first 20 s of drug superfusion are shown. *Error bars* represent S.E.

The EAP Is Located Close to the Domain III Selectivity Filter—The experiments shown in Fig. 2 suggest that mutations at site 1575 open an access pathway for QX-222. However, the question arises whether this access pathway is also physically located at site 1575. Alternatively, mutations at this site may produce allosteric effects, opening a pathway at a site distant from 1575. Here we made use of the swing out hypothesis (see the Introduction) that predicts that the EAP opened by mutations at site 1575 should be modulated by mutations at the neighboring site 1237. To this end, we combined the mutants that open the EAP, I1575A, I1575C, and I1575E, with the mutant K1237E. Only the constructs K1237E/I1575C and K1237E/I1575E produced currents large enough to be studied. As shown in Fig. 3*B*, both double mutants were insensitive to external QX-222. This supports the idea that the EAP opened by mutations at site 1575 is located between the IIIP and the DIVS6.

A Tryptophan in the DIV P-loop Controls External Access of QX-222—Next we tested the Trp-lock hypothesis (see the Introduction) that states that Trp-1531 is a major determinant of the EAP (Fig. 1, *C* and *D*). Thus, we examined the effect of reducing the volume of the side chain at site 1531 on the accessibility for external QX-222. As shown in Fig. 4, *A* and *B*, both W1531G and W1531A were sensitive to external QX-222. The amount of steady-state block in these constructs was substantially smaller at a holding potential of −120 mV than at −90 mV (Fig. 4, *A* and *B*, respectively).

Drug Access and Egress via Site 1531 Are Very Fast—Most interestingly, mutations at site 1531 allowed for very rapid interaction of QX-222 with the binding site. Hence, both the time course of onset of block and of relief from block upon washout was significantly faster with mutations at site 1531 than with mutations at site 1575 (Table 1). This suggests that the EAP opened by mutations at site 1531 is substantially more permeable for QX-222 than the pathway opened at site 1575. It is noteworthy that the amount of steady-state block of W1531G at a holding potential of −120 mV was smaller than that with mutations at site 1575 (Table 1). This may be due to the fact that Gly-1531 not only allows quick access to the binding site but also produces a rapid egress pathway, thereby limiting the steady-state block. To determine the time course of egress from the binding site, we tested the time course of escape of QX-222 when applied intracellularly (see "Experimental Procedures"). As shown in Fig. 5, the time course of current increase following a rapid depolarizing pulse train in the absence of the drug was monoexponential, reflecting the time course of recovery of channels accumulated in the fast inactivated state during the pulse train. During exposure to intracellular QX-222, this time course could be fit by the sum of two exponential functions, reflecting recovery from fast inactivation of unblocked channels and recovery from drug block, respectively. Drug block recovered with a time constant of ~100 s in I1575E and with time constants less than 1.5 s in W1531A and W1531G (Fig. 5).

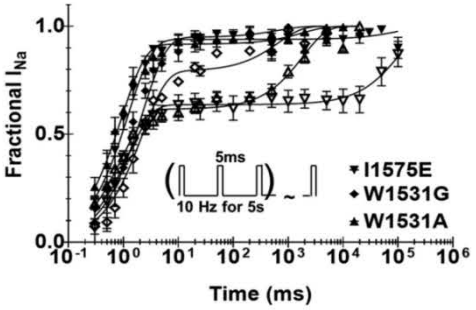

FIGURE 5. **Recovery from block by intracellular QX-222.** A 5-s-long 10-Hz pulse train was applied for repetitive openings of the channels to bind QX-222 to the inner vestibule. After the last pulse in the train, the cell was repolarized to −140 mV for various durations followed by a test pulse to −10 mV. The peak amplitudes of the residual sodium currents evoked by the test pulse were plotted as a function of time and fitted with the sum of two exponential functions. *Filled symbols* indicate drug-free controls, and *open symbols* represent data with 500 μM QX-222 in the intracellular solution. In I1575E, intracellular QX-222 gave rise to a slow recovering component, indicating the slow egress of QX-222 through the EAP. In W1531A/G, this second component was substantially faster, suggesting that these mutations allowed for rapid egress of QX-222 via the EAP. The time constants of this second exponential recovery were significantly smaller in W1531G and W1531A than in I1575E (0.7 ± 0.2 s, $n = 7$; 1.8 ± 0.2 s, $n = 5$; and 105.2 ± 23.1 s, $n = 7$, respectively; $p < 0.01$.). *Error bars* represent S.E.

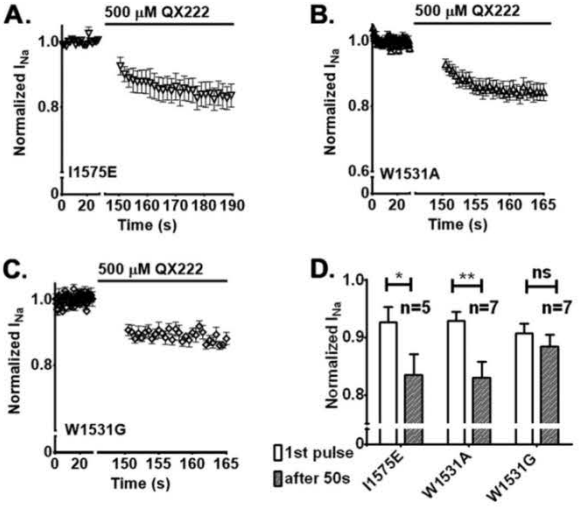

FIGURE 6. **Use-dependent block by external QX-222.** A 2-Hz pulse train was applied for 30 s at a holding potential of −120 mV. Thereafter, external perfusion with QX-222 was started while cells were kept at the holding potential for 120 s. Then repetitive pulsing was again applied at 2 Hz for 90 s. During this period, block increased in I1575E (*A*) and in W1531A (*B*) but not in W1531G (*C*). Use-dependent block was quantified as the ratio of block present with the first pulse and the block with the 100th pulse (*D*). *, $p < 0.05$; **, $p < 0.01$; *ns*, not significant. *Error bars* represent S.E.

Thus, mutations at site 1531 open a pathway that allows both fast access and fast egress.

Trp-1531 Allows for Gated Access in 1575 Mutants—The fast access pathway created by mutations at site 1531 suggests that Trp-1531 constitutes a substantial barrier for the external access into the internal vestibule. This raises the question how QX-222 can travel into the channel with the mutations at site 1575 in which Trp-1531 may still restrict the access to the internal vestibule. Perhaps Trp-1531 acts like a gate and periodically opens or closes the EAP during channel activation and/or inactivation. In that case, block by QX-222 may be use-dependent. To explore this possibility, we held the channels at a potential of −120 mV while applying QX-222 externally for 120 s. During this period, channels are expected to reside in the closed state. Thereafter, a 2-Hz pulse train was applied for 50 s. The amount of use-dependent block was defined as the ratio of current reduction produced by the first *versus* the last pulse in the train. Fig. 6 shows that I1575E and W1531A but not W1531G were blocked by QX-222 in a use-dependent fashion. This suggests that both tryptophan and alanine side chains at position 1531 act as a gate, perhaps restricting drug egress between pulses. In W1531G, the amino acid side chain is absent, and this appears to allow access during the resting state of the channel with no additional block during repetitive pulsing. This notion is supported by the data presented in Fig. 5 demonstrating a substantially slower egress of QX-222 in W1531A than in W1531G. However, in these experiments, QX-222 was loaded into the channel from the intracellular space. When applied from the extracellular side as with the experiments in Fig. 6, QX-222 may leave the channel not only via the EAP but also via the internal pore when the activation gate is opened by the test pulses. The likelihood of this escape would be greatly determined by the off-rate from the receptor. In this case, the use-dependent block shown in Fig. 6, *A* and *B*, may have resulted from differences in the periodic development of a high affinity state during the pulse train. Because the amphiphilic congener of QX-222, lidocaine, is known to bind to the inactivated state (39), we examined the affinity of QX-222 to the fast inactivated state in W1531A and W1531G. 500 μM QX-222 shifted the steady-state inactivation curve to more hyperpolarized potentials in W1531A but not in W1531G, indicating a loss of high affinity binding in W1531G (Fig. 7, *A* and *B*). This suggests that the loss of use-dependent development in W1531G may in part be a result of a loss in high affinity binding. (We did not test possible effects of QX-222 in I1575E because block development in this mutant is very slow such that development of steady state during the 50-ms conditioning prepulse is unlikely.) Conversely, if the sole difference between binding of QX-222 to W1531A and to W1531G were due to a higher affinity of QX-222 for W1531A then the block time constant should be faster with W1531A. However, the time constant of block development is ~3 times slower in W1531A than in W1531G, supporting the notion of a substantial difference in drug access between the constructs.

Mutations that alter the external accessibility of QX-222 may also give rise to alterations in the kinetic behavior of the channel. This has been reported previously for mutations at both sites 1575 and 1531 (14, 40, 41). Because QX-222 is likely to bind to the inactivated state (Fig. 7*A*), we examined the effect of the mutations at sites 1237, 1531, and 1575 on a number of kinetic parameters of fast inactivation (Table 2). The time constant of entry into inactivation was significantly increased only by K1237E/I1575E. With the exception of I1575E/F1579A, all mutants shifted the half-point of inactivation to more negative potentials, suggesting stabilization of the fast inactivated state. Also, the time course of recovery from inactivation was pro-

longed by all constructs except I1575E/F1579A. These data confirm previous reports suggesting that the region at the interface between the P-loops of domains III and IV and the S6 segment of domain IV is a critical determinant of inactivation (23, 42–45).

The Mutation W1531G Opens an Access Pathway for Inorganic Ions—Mutations at site 1531 have been shown previously to shift the V_{rev} to more negative values, indicating a loss of selectivity for Na^+ ions (46). In our hands, the V_{rev} was unchanged by W1531A but was shifted by ~−30 mV in W1531G, suggesting a reduced selectivity for permeation of sodium in this construct. This may be the result of structural alterations in the domain IV P-loop region, perhaps as a consequence of increased backbone flexibility at Gly-1531. Alternatively, the access pathway for QX-222 created by the mutation at site 1531 may be permeable for small inorganic ions. If this additional ionic pathway is nonselective, the V_{rev} of the inward current would be shifted toward zero. To investigate this possibility, we blocked the current through the selectivity filter in W1531G and in W1531A with TTX. Interestingly, both Trp-1531 mutations had highly reduced TTX sensitivity (the IC_{50} for reduction of peak inward currents was 9.1 ± 2.2 nM, 0.7 ± 0.1 μM, and 2.0 ± 0.3 μM for wild-type, W1531A, and W1531G, respectively; Fig. 8*C*, *inset*). Fig. 8, *A* and *B*, show the effect of TTX on the V_{rev} in wild type and W1531G. TTX had no effect on the V_{rev} in wild type and W1531A channels (data not shown) but substantially shifted the V_{rev} of W1531G toward zero (Fig. 8*B*). This suggests the presence of a nonselective ionic pathway that is not blocked by TTX.

Interestingly, with W1531G, even high concentrations of TTX blocked only ~80% of the current (Fig. 8*C*, *inset*). This

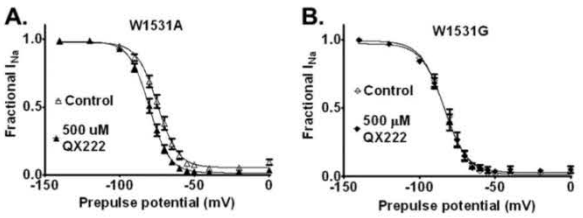

FIGURE 7. **Effect of QX-222 on inactivation properties of channels carrying mutations at site 1531.** *A*, in W1531A, 500 μM QX-222 significantly shifted the steady-state inactivation curve to hyperpolarized potentials. $V_{1/2}$ was −74.6 ± 0.6 and −80.0 ± 0.5 mV under control conditions and with QX-222, respectively ($n = 9$; $p < 0.0001$). *B*, in W1531G, 500 μM QX-222 did not produce a significant shift in the steady-state inactivation curve. $V_{1/2}$ was −82.7 ± 0.7 and −84.1 ± 0.8 mV under control conditions and with QX-222, respectively ($n = 6$; $p = 0.17$). *Error bars* represent S.E.

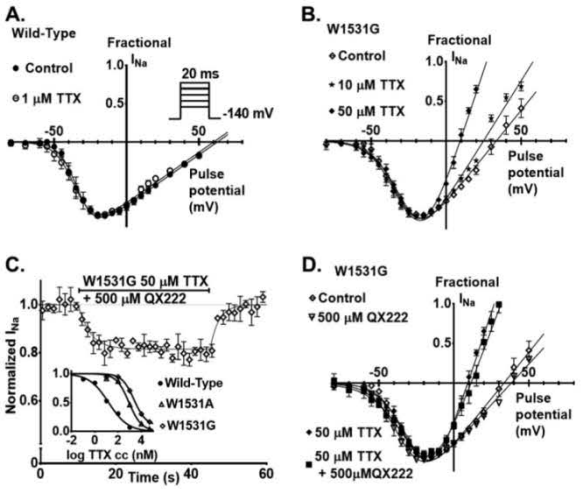

FIGURE 8. **W1531G opens an access pathway for ionic current.** *A*, in wild-type channels, 1 μM TTX blocked currents by 93.0 ± 1.4%. The V_{rev} was 63 ± 3 mV ($n = 5$) under drug-free conditions and 60 ± 3 mV ($n = 7$) during external application of 1 μM TTX ($p > 0.99$). The corresponding values for W1531A were 64 ± 1 ($n = 4$) and 61 ± 4 mV ($n = 5$) during drug-free control and external application of 10 μM TTX ($p = 0.24$; data not shown), respectively, which was associated with a current reduction by 86 ± 1%. *B*, block of the selectivity filter by 50 μM TTX in W1531G reduced currents by 83 ± 3% and resulted in a significant shift in the V_{rev} from 35 ± 1 ($n = 13$) to 9 ± 1 mV ($n = 12$; $p < 0.0001$). *C*, in the presence of 50 μM TTX, additional superfusion with 500 μM QX-222 (indicated by *horizontal bar*) blocked 18.5 ± 0.5% of W1531G channels. The time constant of block development was 3.17 ± 0.45 s. *Inset*, TTX sensitivity decreased for both mutants (IC_{50} for W1531A, 0.84 ± 0.06 μM, $n = 4$; W1531G, 2.30 ± 0.31 μM, $n = 3$; wild type, 15.10 ± 2.23 nM, $n = 5$). Residual current was 0 ± 1% for wild type, 1 ± 2% for W1531A, and 10 ± 5% for W1531G channels. *D*, external application of 500 μM QX-222 produced a minor nonsignificant shift of the V_{rev} from 33 ± 1 ($n = 13$) to 38 ± 1 mV ($n = 6$; $p > 0.05$). During superfusion with 50 μM TTX, additional application of 500 μM QX-222 resulted in a small nonsignificant shift of the V_{rev} from 9 ± 1 ($n = 12$) to 11 ± 1 mV ($n = 7$; $p > 0.05$). *Error bars* represent S.E.

TABLE 2

Kinetic properties and voltage dependence of inactivation in $Na_V1.4$ channel and its mutants

The time constant of entry into inactivation was determined by single exponential fits to the decay phase of Na^+ currents elicited by 20-ms pulses to −10 mV from a holding potential of −140 mV. The voltage dependence of steady-state inactivation was determined as described under "Experimental Procedures." The time course of recovery from inactivation was determined by 20-ms test pulses to −20 mV introduced at variable times following a 50-ms inactivating prepulse to −20 mV. The maximum inward currents elicited by the test pulses were normalized to the respective maximum value and plotted as a function of the time after the conditioning prepulses. The time constant of recovery was determined by single exponential fits to these plots.

	Time constant of entry into inactivation	Steady-state inactivation ($V_{1/2}$)	Steady-state inactivation curve slope (k)	Time constant of recovery from inactivation
	ms	*mV*	*mV*	*ms*
NaV1.4	0.34 ± 0.02	−65.6 ± 0.6	5.94 ± 0.55	0.87 ± 0.06
I1575A	0.48 ± 0.19	−80.1 ± 1.0[a]	6.72 ± 0.87	1.37 ± 0.12[b]
I1575C	0.43 ± 0.08	−76.9 ± 1.1[b]	7.64 ± 0.97	1.09 ± 0.08[b]
I1575E	0.30 ± 0.02	−75.0 ± 0.7[c]	7.24 ± 0.61	1.61 ± 0.12[b]
I1575H	0.26 ± 0.03	−84.3 ± 1.0[a]	6.31 ± 0.79	0.88 ± 0.07
I1575E/F1579A	0.49 ± 0.02	−61.6 ± 1.1	6.95 ± 0.98	0.94 ± 0.18
K1237E/I1575E	1.05 ± 0.20[b]	−76.3 ± 0.8[b]	5.41 ± 0.79	1.22 ± 0.13[b]
K1237E/I1575C	0.48 ± 0.05	−76.1 ± 0.9[b]	5.16 ± 0.82	1.21 ± 0.18[b]
W1531A	0.42 ± 0.04	−74.0 ± 1.0[c]	7.17 ± 0.92	1.66 ± 0.14[b]
W1531G	0.44 ± 0.03	−82.7 ± 0.7[a]	7.53 ± 0.57	1.62 ± 0.10[b]

[a] $p < 0.001$ compared with data from wild type.
[b] $p < 0.01$ compared with data from wild type.
[c] $p < 0.05$ compared with data from wild type.

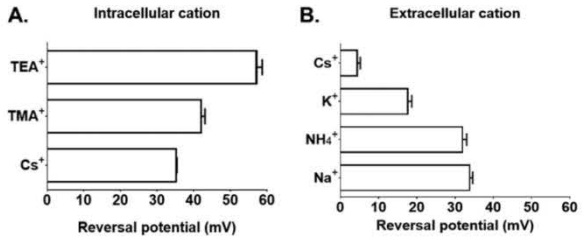

FIGURE 9. **Ion selectivity of W1531G.** *A*, the V_{rev} was shifted toward more positive potentials when intracellular 105 mM Cs^+ (35 ± 1 mV, n = 13) was replaced by 105 mM TMA^+ (42 ± 2 mV, n = 4) and 105 mM TEA^+ (57 ± 4 mV, n = 5) using the same current-voltage pulse protocol as in Fig. 8. This suggests that TMA^+ is less permeable than Cs^+. W1531G does not appear to conduct TEA^+ because with the TEA^+ intracellular solution V_{rev} is similar to that of the wild-type channel, and this value is close to the calculated V_{rev} of a perfectly sodium-selective conductance in this solution (68 mV). *B*, similar experiment to *A* but the extracellular 140 mM Na^+ was replaced by 140 mM NH_4Cl^+ (V_{rev} = 32 ± 1 mV, n = 6), K^+ (V_{rev} = 18 ± 1 mV, n = 4), and Cs^+ (V_{rev} = 4 ± 1 mV, n = 4). *Error bars* represent S.E.

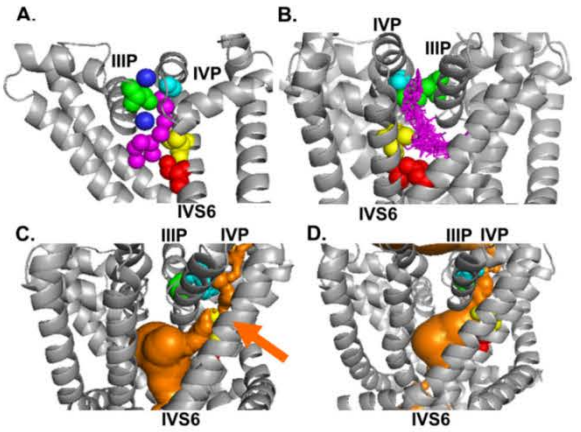

FIGURE 10. *A*, during the MD simulation of W182G (*cyan*) mutant Na_VRh channel, water molecules (*magenta*) penetrate the cavity between Ser-180 (*green*) and Ile-204 (*yellow*) originally occupied by the bulky side chain of Trp-182. *Blue spheres* are sodium ions in the selectivity filter. *B*, homogenous distribution of 30 docking poses of QX-222 molecules (*magenta*) along the EAP in the Na_VRh-based homology model. *C*, in the wild-type Na_VRh crystal structure, the HOLE algorithm was unable to identify a continuous tunnel (*orange* object) from the extracellular space to the inner vestibule between IVS6 and IIIP. The *arrow* indicates the site of interruption of the pathway. *D*, after introduction of the mutation W182G, the pathway identified by HOLE (*orange* object) becomes contiguous.

could indicate that concentrations of TTX >50 μM block 100% of channels and that the residual current is flowing through the EAP. Fig. 8*C* shows that in the presence of 50 μM TTX 500 μM QX-222 gives rise to an additional block by ~20%. Under these conditions, QX-222 most likely reaches its binding site only via the EAP in channels whose main permeation pathway is blocked by TTX. Furthermore, in TTX-blocked W1531G channels, addition of QX-222 did not produce any significant shift of the V_{rev} (Fig. 8*D*). This would be expected if ~100% of conductance via the main ionic pathway is blocked by TTX and all of the measured current flows through the EAP.

To characterize the permeability of the EAP in W1531G for cations of different volumes, we systematically exchanged the major cations Na^+ and Cs^+ in the intracellular and extracellular solution by other ion species and determined the change of V_{rev} produced by the ion exchange (Fig. 9, *A* and *B*). From the measured values for V_{rev}, we determined the following permeability sequence (ionic diameter in parentheses; Ref. 24): Na^+ (2 Å) > NH_4^+ (3.6 Å) > K^+ (3 Å) > Cs^+ (3.4 Å) > TMA^+ (6.0 Å)). TEA^+ (8.2 Å) was not permeable. Thus, the decrease in permeability through the EAP roughly correlates with the respective increase in ionic diameter of the permeating ions and suggests that the EAP acts as a molecular sieve, selecting by size of the ion.

A Molecular Model of the EAP—As mentioned above, the access pathway by mutations at site 1531 was predicted by the location of the homologous amino acid in published structures of bacterial VGSCs (1–4). We wondered whether the molecular dimensions of such a pathway would be consistent with the available structures. To this end, we examined the crystal structure of Na_VRh (4) and an Na_VRh-based homology model of the $rNa_V1.4$ for the presence of such EAP. As mentioned under "Experimental Procedures," we first simulated the mutation to a glycine at a position homologous to Trp-1531 in the Na_VRh crystal structure (W182G of chain D). During the MD simulations, the mutated structure remained stable in the vicinity of Gly-182. The space previously occupied by the side chain of Trp-182 was filled by water molecules (Fig. 10*A*). Fig. 10*D* shows that the algorithm HOLE identified a contiguous pathway in this mutated crystal structure but not in the wild-type channel (Fig. 10*C*). This pathway was parallel to the ion-conducting pore in the outer vestibule at the interface between chains C and D. This snapshot of the MD simulation was used for building a homology model of $rNa_V1.4$. In the mutated homology model (W1531G), the docking procedure (see "Experimental Procedures") resulted in a homogeneous distribution of docking poses of QX-222 molecules along the EAP, suggesting the absence of significant steric hindrance for the permeation of QX-222 (Fig. 10*B*).

DISCUSSION

In this work we used the modulation of EAPs for QX-222 to test structural predictions from homology models as well as available crystal structures of bacterial VGSCs.

The EAP Opened by Mutations at Site 1575—Previously, Sunami *et al.* (18) demonstrated that not only substitutions of the native isoleucine by alanine, (resulting in a shorter side chain at site 1575) opened an EAP but also replacements with larger and more reactive side chains (cysteine) or introduction of a negative charge (glutamate). These latter substitutions produced a stronger block by QX-222 than the replacement by alanine. In our study, however, charged substitutions at site 1575 produced less block than the uncharged mutation I1575A. Furthermore, in our hands, block equilibrium in the mutants at site 1575 was reached within 50–100 s (Fig. 2), which is faster than in the study by Sunami *et al.* (18). Perhaps these discrepancies are due to the use of different expression systems, *i.e. Xenopus laevis* oocytes in Sunami *et al.* (18) *versus* mammalian cells in the present study. In addition to this earlier report, we show that a positively charged histidine at site 1575 also allows accessibility by QX-222. In summary, these data suggest that the physiologic closure of the EAP is produced by a subtle "con-

formational balance" at site 1575 that is easily disrupted by introduction of both steric and electrostatic influences.

Topology of the DIV-S6 EAP—Using a homology model of the $Na_V1.5$ channel, Bruhova *et al.* (20) proposed that QX-314 enters the internal vestibule through a "sidewalk" between segments IIIP, IIIS6, and IVS6. Tikhonov and Zhorov (22) suggested that this access pathway may be generated by a tunnel formed by the inner helices of repeats III and IV and the IIIP. Thus, we propose that the EAP created by mutations at site 1575 opens a pathway between Lys-1237 of the PIII and Ile-1575 of IVS6. To provide an experimental assessment of this molecular localization of the EAP, we tested the swing out hypothesis, which states that the mutation K1237E should modulate the EAP created by mutations at site 1575 (see the Introduction). Indeed, as shown in Fig. 3*B*, the double mutants I1575E/K1237E and I1575C/K1237E were impermeable to QX-222, suggesting that the EAP created by I1575E/C is closed by the additional mutation K1237E (Fig. 3*B*). The simplest interpretation of this phenomenon would assume a lateral motion by Glu-1237, resulting in an interaction with site 1575, thereby causing a local conformational change that obstructs the EAP. In the case of I1575E/K1237E, the fact that both Glu-1575 and Glu-1237 carry negative charges argues against a simple "closing" of the pathway between the IIIP and the IVS6 because electrostatic repulsion would probably prevent a direct contact between these amino acids. Most likely, a complex structural rearrangement at this location is produced by the double mutant, resulting in the closure of the EAP.

As mentioned earlier, the "swing out hypothesis" is based on homology models of the VGSC that were derived from crystal structures of bacterial K^+ channels. As shown in Fig. 1, the more recent structures of bacterial VGSC predict a substantially different arrangement of the interface between the P-loops of DIII and IV and the S6 segment of DIV: the tryptophan homologous to rNav1.4 Trp-1531 occupies the space between the homologous positions 1237 (selectivity filter of DIII) and 1575 (DIV-S6). In this structure, a swing out of IIIP can only occur if the side chain homologous to Trp-1531 moves away to open a space between DIV-S6 and IIIP. The fact that mutations at site 1531 open a highly permeable EAP for QX-222 suggests that a conformational change at this site may provide substantial space (Trp-lock hypothesis). Perhaps this space could also be provided if Trp-1531 "flipped" into a different direction. Such "flipping" action of Trp-1531 has been suggested previously by Tsang *et al.* (41) to reconcile the fact that mutation W1531C is both accessible from the outside (47) and interacts with local anesthetics in the internal vestibule. Furthermore, Payandeh *et al.* (2) recently presented crystallographic evidence for a conformational change involving homologous position Trp-179 associated with inactivation in the bacterial VGSC Na_VAb. Thus, in the mutants at site 1575, a molecular rearrangement of the interface between the selectivity filter and the IVS6 may allow for access of QX-222 when the entrance into the internal cavity is cleared by a flipping motion of Trp-1531.

The EAP Opened at Site 1531—One motif of the P-loop region that is shared among bacterial and mammalian VGSCs is a ring of tryptophan residues located two positions upstream of the selectivity filter (the only exception is the tryptophan in the IIP that is located immediately upstream of the glutamate of the selectivity filter in mammalian VGSCs). As mentioned in the Introduction, the Trp-lock hypothesis states that Trp-1531 represents a substantial steric hindrance for external access of QX-222. This idea is supported by the fact that replacements of Trp-1531 by both alanine and glycine resulted in a significant block by externally applied QX-222 (Fig. 4). Moreover, the development of block was extremely fast, having a time constant of <3 s as opposed to time constants >10 s with mutations at site 1575 (Table 1). As a matter of fact, to date there is no report of such rapid access for charged lidocaine analogues when applied from the external solution. This suggests that the pathway opened by mutations at site 1531 is highly permeable for the QX-222 molecule. Such high permeability is also supported by the experiments presented in Fig. 5 examining the egress of QX-222 once loaded into the internal vestibule from the cytoplasmic side. In both mutants at site 1531, QX-222 escaped rapidly with a time constant of <1.5 s (Fig. 5). In W1531G, the combination of rapid drug access and drug egress may also account for the moderate level of external block by QX-222 (Fig. 4 and Table 1). Previously, Tsang *et al.* (41) investigated the effect of external application of QX-222 to the mutants W1531C, W1531A, and W1531Y. These authors concluded that the tested mutants were insensitive to external QX-222 (although Fig. 6C of Tsang *et al.* (41) suggests an ~10% block with W1531A). Conversely, these authors observed a very rapid recovery from block by internally applied QX-314 in the mutant W1531C, which might indicate rapid egress from the binding site similar to the data shown in Fig. 5 of the present study. One reason why Tsang *et al.* (41) might have failed to observe block during continuous application of depolarizing test pulses may be the low pulsing rate in their experiments (0.25 Hz). Given the rapid egress of QX-222 in the mutants at site 1531 (Fig. 5), the drug most likely escapes between pulses at low stimulation frequencies.

Kinetic Changes Imposed by Mutations at Site 1531—The principle kinetic changes imposed by mutations at site 1531 are as follows. 1) Both W1531A and W1531G gave rise to a substantial shift of the voltage dependence of fast inactivation to hyperpolarized potentials. This shift was larger with W1531G than with W1531A (Fig. 7 and Table 2). 2) External application of QX-222 induced a further hyperpolarizing shift in W1531A but not in W1531G. The half-point of fast inactivation with W1531A during application of QX-222 matched the half-point of inactivation of W1531G under drug-free conditions (Fig. 7). 3) Block by QX-222 is use-dependent in W1531A but not in W1531G (Fig. 6). 4) Block by QX-222 is strongly enhanced by depolarized holding potentials in W1531A but not in W1531G (Fig. 4).

Previously, Tsang *et al.* (41) reported that the mutant W1531C gives rise to a hyperpolarizing shift of the half-point of fast inactivation by ~30 mV, which is consistent with our findings in W1531A/G. These authors argued that "nonaromatic substitutions of Trp-1531 intrinsically mimic local anesthetic drug action (or normal drug-bound channels) by negatively shifting the steady-state fast inactivation." In the following, we expand on this suggestion and propose an idea of the molecular

underpinnings of the kinetic effects produced by mutations at site 1531.

The DIV-S6 is crucial for the development inactivation (23, 48–51). As mentioned above, the available crystal structures of VGSCs suggest that Trp-1531 is in close spatial relationship to DIV-S6. Perhaps an interaction of Trp-1531 and DIV-S6 intrinsically destabilizes fast inactivation, resulting in the "physiological" $V_{1/2}$ of inactivation (−65 mV; Table 1). This would explain why mutations at site 1531 stabilize inactivation. This stabilization is smaller with W1531A ($V_{1/2}$ of inactivation = −74.0 mV; Table 2) because the alanine side chain may still interact with DIV-S6, whereas such interaction would be lost with W1531G ($V_{1/2}$ of inactivation = −82.7 mV; Table 2). Perhaps position 1575 in DIV-S6 is part of this interaction site, which would explain why mutations at this site also stabilize inactivation (Table 2).

In theory, the stabilization of inactivation with mutations at site 1531 should enhance drug binding to the high affinity inactivated state as has been reported for other mutations that stabilize inactivation (52). Paradoxically, however, nonaromatic substitutions at this site reduce high affinity binding of local anesthetic agents (41). In the present study, QX-222 stabilized inactivation in W1531A but not in W1531G. In the context of our working hypothesis, an interaction between QX-222 and Ala-1531 could disturb the destabilizing activity of Ala-1531 on inactivation, thereby shifting the half-point of inactivation to the same potential as with W1531G ($V_{1/2}$ of inactivation = −83.2 mV; Table 2). The absence of a side chain in this latter construct may result in a complete loss of destabilization of inactivation and consequently of any modulatory activity by QX-222. The fact that inactivation is stabilized by QX-222 in W1531A but not in W1531G may also account for the finding that use-dependent block (Figs. 4 and 6) and enhanced block at depolarized potentials (Fig. 4) were observed with W1531A but not with W1531G.

Hence QX-222 may act as an allosteric modulator of inactivation, a concept that has been proposed previously as a mechanism for local anesthetic drug action (53). However, with the mutations W1531A/G, the situation is more complicated as these constructs also open an access/egress pathway for QX-222. For example, the fact that QX-222 produces more block at a holding potential of −90 mV in W1531A than in W1531G (Fig. 4) may partially result from slower drug egress via the EAP in W1531A (Fig. 5).

W1531G Gives Rise to a Second Ion Conducting Pathway—To test for the presence of a second non-selective ion-conducting pathway, we sought to block the main ion-conducting pore by application of TTX. To this end, we had to apply substantially higher concentrations of TTX with the mutants at site 1531 than with wild-type channels. A number of mutations in the region of the selectivity filter have been reported previously to reduce affinity to TTX (for a review, see Ref. 54), but site 1531 has not been tested in this regard. Although the insensitivity to TTX by the mutations at site 1531 may indicate a conformational change at the selectivity filter, the V_{rev} is only shifted in W1531G, not in W1531A, despite similar reductions in TTX sensitivity. Also, a number of isoforms of Na^+ channels are naturally insensitive to TTX despite unchanged selectivity (55). Thus, the function of the selectivity filter may be intact in the mutations at site 1531. Fig. 8 shows that the V_{rev} of W1531G is negatively shifted compared with wild-type channels and that this shift is increased in a concentration-dependent fashion with external application of TTX. This suggests the presence of a second nonspecific ion-conducting pathway in this mutant. No shift in the V_{rev} was observed in W1531A, perhaps because of a lower permeability of this EAP as a consequence of steric hindrance by the alanine side chain. Accordingly, the rate of block development by QX-222 was substantially smaller in W1531A than in W1531G. Perhaps QX-222 can still enter the channel during a "flip" of the Ala-1531 side chain (see above). The notion that the EAP is a separate pore is supported by the fact that upon channel block by TTX addition of QX-222 gave rise to a substantial further reduction in the current as if the QX-222 molecules passing through the EAP can still reach their binding site and block the current through the EAP (Fig. 8*C*). The fact that QX-222 did not completely block channels via the EAP may be a consequence of a high off-rate from the receptor such that drug molecules may leave the channel into the intracellular compartment during channel opening.

The EAP appears to support size-specific flow of monovalent cations. The largest cation that could pass ionic current was TMA. This suggests that the EAP has a maximum diameter of ~6 Å. Recently, Prütting and Grissmer (56) reported a mutation in the pore helix of the hKv1.3 channel to create an ion-conducting pore parallel to the central potassium-conducting pore. The proposed pathway is lined by the pore helix and the adjacent S5 and S6, *i.e.* a similar location as the EAP described in this study. Interestingly, this pathway had a permeability for cations that is comparable with the EAP described in this study ($Na^+ > NH_4^+ > Cs^+ > K^+$). Furthermore, analogous to the EAP, current flow through this parallel current pathway was unaffected by pore blockers like charybdotoxin and tetraethylammonium (56). A comparable pathway running in parallel to the central pore was also proposed from molecular dynamics simulations in KcsA channels (57). How large is the conductance of the accessory ion-conducting pathway? If we assume that this pathway is non-selective for cations, then the calculated V_{rev} would be 6 mV under the given experimental conditions. In W1531G, the V_{rev} was shifted from 63 ± 3 (wild type) to 35 ± 1 mV. Assuming that this shift is produced by the addition of a second conductance with a V_{rev} of 6 mV, the conductance of the additional pathway would be about the same as the ionic conductance through the selectivity filter. Thus, the mutation W1531G may have created a substantial second ion-conducting pore.

A Molecular Model of the EAP—As shown in Fig. 10, both the crystal structure of the VGSC Na_VRh and a homology model based on this structure support the idea that QX-222 can pass through the interface between the IIIP and the IVS6 once the steric hindrance of Trp-1531 in $rNa_V1.4$ or its homologue Trp-182 in Na_VRh are replaced by glycines. We adopted the Na_VRh x-ray structure to construct our homology model because the filter sequence can be aligned without gaps in contrast to other bacterial crystal structures (3, 4). The docking of QX-222 enabled us to confirm the absence of putative steric constraints along the EAP. However, because of the substantial difference

in primary sequences between prokaryotic and eukaryotic VGSCs, no inferences regarding the site of the extracellular entrance to the EAP can be made. With regard to the interface between the selectivity filter and the inner vestibule, our study suggests strong structural similarities between eukaryotic and prokaryotic VGSCs.

Biological Significance of the EAP—The cardiac sodium channel isoform can be blocked by permanently charged local anesthetics in its native state (12), which may be of substantial clinical importance (13). Qu *et al.* (15) showed that a molecular determinant of the heart-specific access pathway is a threonine located in the upper DIV-S6 at a site homologous to Cys-1572 in $rNa_V1.4$. The location of this site suggests that it may be a part of the DIV-S6 EAP considered in our study. The natural occurrence of an EAP in the cardiac isoform suggests some biological significance of EAPs, although the exact biological function remains to be determined. In addition, EAPs may be relevant in pathological processes. Thus, a naturally occurring mutation in the cardiac isoform, S1710L, has been reported to enhance external block by QX-314 and in reduced use-dependent block by the clinically used antiarrhythmic drug mexiletine (19). Ser-1710 is located next to the putative selectivity filter in domain IV and, thus, is located close to the domain IV-S6 EAP described in our present study. To the best of our knowledge, there are no reports of naturally occurring mutations at the sites in human sodium channel isoforms homologous to site $rNa_V1.4$ Trp-1531. However, a naturally occurring mutation in $hNa_V1.5$ one position N-terminal of the position homologous to $rNa_V1.4$ Trp-1531 has been found to be associated with Brugada syndrome (58). This mutation had no effects on ionic selectivity but resulted in changes in inactivation gating. These findings suggest that mutations in the vicinity of Trp-1531 are compatible with life and may result in significant human pathology.

Acknowledgment—We thank Dr. Boris S. Zhorov, Department of Biochemistry and Biomedical Sciences, McMaster University, Hamilton, Ontario, Canada for providing the coordinates of the homology models of the mammalian Na_V (22, 26).

REFERENCES

1. Payandeh, J., Scheuer, T., Zheng, N., and Catterall, W. A. (2011) The crystal structure of a voltage-gated sodium channel. *Nature* **475,** 353–358
2. Payandeh, J., Gamal El-Din, T. M., Scheuer, T., Zheng, N., and Catterall, W. A. (2012) Crystal structure of a voltage-gated sodium channel in two potentially inactivated states. *Nature* **486,** 135–139
3. McCusker, E. C., Bagnéris, C., Naylor, C. E., Cole, A. R., D'Avanzo, N., Nichols, C. G., and Wallace, B. A. (2012) Structure of a bacterial voltage-gated sodium channel pore reveals mechanisms of opening and closing. *Nat. Commun.* **3,** 1102
4. Zhang, X., Ren, W., DeCaen, P., Yan, C., Tao, X., Tang, L., Wang, J., Hasegawa, K., Kumasaka, T., He, J., Wang, J., Clapham, D. E., and Yan, N. (2012) Crystal structure of an orthologue of the NaChBac voltage-gated sodium channel. *Nature* **486,** 130–134
5. Terlau, H., Heinemann, S. H., Stühmer, W., Pusch, M., Conti, F., Imoto, K., and Numa, S. (1991) Mapping the site of block by tetrodotoxin and saxitoxin of sodium channel II. *FEBS Lett.* **293,** 93–96
6. Heinemann, S. H., Terlau, H., Stühmer, W., Imoto, K., and Numa, S. (1992) Calcium channel characteristics conferred on the sodium channel by single mutations. *Nature* **356,** 441–443
7. Schlief, T., Schönherr, R., Imoto, K., and Heinemann, S. H. (1996) Pore properties of rat brain II sodium channels mutated in the selectivity filter domain. *Eur. Biophys. J.* **25,** 75–91
8. Favre, I., Moczydlowski, E., and Schild, L. (1996) On the structural basis for ionic selectivity among Na^+, K^+, and Ca^{2+} in the voltage-gated sodium channel. *Biophys. J.* **71,** 3110–3125
9. Hille, B. (1977) Local anesthetics: hydrophilic and hydrophobic pathways for the drug-receptor reaction. *J. Gen. Physiol.* **69,** 497–515
10. Frazier, D. T., Narahashi, T., and Yamada, M. (1970) The site of action and active form of local anesthetics. II. Experiments with quaternary compounds. *J. Pharmacol. Exp. Ther.* **171,** 45–51
11. Strichartz, G. R. (1973) The inhibition of sodium currents in myelinated nerve by quaternary derivatives of lidocaine. *J. Gen. Physiol.* **62,** 37–57
12. Alpert, L. A., Fozzard, H. A., Hanck, D. A., and Makielski, J. C. (1989) Is there a second external lidocaine binding site on mammalian cardiac cells? *Am. J. Physiol. Heart Circ. Physiol.* **257,** H79–H84
13. Lee, P. J., Sunami, A., and Fozzard, H. A. (2001) Cardiac-specific external paths for lidocaine, defined by isoform-specific residues, accelerate recovery from use-dependent block. *Circ. Res.* **89,** 1014–1021
14. Ragsdale, D. S., McPhee, J. C., Scheuer, T., and Catterall, W. A. (1994) Molecular determinants of state-dependent block of Na^+ channels by local anesthetics. *Science* **265,** 1724–1728
15. Qu, Y., Rogers, J., Tanada, T., Scheuer, T., and Catterall, W. A. (1995) Molecular determinants of drug access to the receptor site for antiarrhythmic drugs in the cardiac Na^+ channel. *Proc. Natl. Acad. Sci. U.S.A.* **92,** 11839–11843
16. Sunami, A., Dudley, S. C., Jr., and Fozzard, H. A. (1997) Sodium channel selectivity filter regulates antiarrhythmic drug binding. *Proc. Natl. Acad. Sci. U.S.A.* **94,** 14126–14131
17. Sunami, A., Glaaser, I. W., and Fozzard, H. A. (2000) A critical residue for isoform difference in tetrodotoxin affinity is a molecular determinant of the external access path for local anesthetics in the cardiac sodium channel. *Proc. Natl. Acad. Sci. U.S.A.* **97,** 2326–2331
18. Sunami, A., Glaaser, I. W., and Fozzard, H. A. (2001) Structural and gating changes of the sodium channel induced by mutation of a residue in the upper third of IVS6, creating an external access path for local anesthetics. *Mol. Pharmacol.* **59,** 684–691
19. Sasaki, K., Makita, N., Sunami, A., Sakurada, H., Shirai, N., Yokoi, H., Kimura, A., Tohse, N., Hiraoka, M., and Kitabatake, A. (2004) Unexpected mexiletine responses of a mutant cardiac Na^+ channel implicate the selectivity filter as a structural determinant of antiarrhythmic drug access. *Mol. Pharmacol.* **66,** 330–336
20. Bruhova, I., Tikhonov, D. B., and Zhorov, B. S. (2008) Access and binding of local anesthetics in the closed sodium channel. *Mol. Pharmacol.* **74,** 1033–1045
21. Lipkind, G. M., and Fozzard, H. A. (2000) KcsA crystal structure as framework for a molecular model of the Na^+ channel pore. *Biochemistry* **39,** 8161–8170
22. Tikhonov, D. B., and Zhorov, B. S. (2005) Modeling P-loops domain of sodium channel: homology with potassium channels and interaction with ligands. *Biophys. J.* **88,** 184–197
23. Zarrabi, T., Cervenka, R., Sandtner, W., Lukacs, P., Koenig, X., Hilber, K., Mille, M., Lipkind, G. M., Fozzard, H. A., and Todt, H. (2010) A molecular switch between the outer and the inner vestibules of the voltage-gated Na^+ channel. *J. Biol. Chem.* **285,** 39458–39470
24. Sun, Y. M., Favre, I., Schild, L., and Moczydlowski, E. (1997) On the structural basis for size-selective permeation of organic cations through the voltage-gated sodium channel: effect of alanine mutations at the DEKA locus on selectivity, inhibition by Ca^{2+} and H^+, and molecular sieving. *J. Gen. Physiol.* **110,** 693–715
25. Huang, C. J., and Moczydlowski, E. (2001) Cytoplasmic polyamines as permeant blockers and modulators of the voltage-gated sodium channel. *Biophys. J.* **80,** 1262–1279
26. Tikhonov, D. B., and Zhorov, B. S. (2012) Architecture and pore block of eukaryotic voltage-gated sodium channels in view of NavAb bacterial sodium channel structure. *Mol. Pharmacol.* **82,** 97–104
27. Todt, H., Dudley, S. C., Jr., Kyle, J. W., French, R. J., and Fozzard, H. A. (1999) Ultra-slow inactivation in μ1 Na^+ channels is produced by a struc-

tural rearrangement of the outer vestibule. *Biophys. J.* **76,** 1335–1345
28. Dudley, S. C., Jr., Todt, H., Lipkind, G., and Fozzard, H. A. (1995) A μ-conotoxin-insensitive Na^+ channel mutant: possible localization of a binding site at the outer vestibule. *Biophys. J.* **69,** 1657–1665
29. Boehm, S. (1999) ATP stimulates sympathetic transmitter release via presynaptic P2X purinoceptors. *J. Neurosci.* **19,** 737–746
30. Kutzner, C., Grubmüller, H., de Groot, B. L., and Zachariae, U. (2011) Computational electrophysiology: the molecular dynamics of ion channel permeation and selectivity in atomistic detail. *Biophys. J.* **101,** 809–817
31. Hornak, V., Abel, R., Okur, A., Strockbine, B., Roitberg, A., and Simmerling, C. (2006) Comparison of multiple Amber force fields and development of improved protein backbone parameters. *Proteins* **65,** 712–725
32. Berger, O., Edholm, O., and Jähnig, F. (1997) Molecular dynamics simulations of a fluid bilayer of dipalmitoylphosphatidylcholine at full hydration, constant pressure, and constant temperature. *Biophys. J.* **72,** 2002–2013
33. Cordomi, A., Caltabiano, G., and Pardo, L. (2012) Membrane protein simulations using AMBER force field and Berger lipid parameters. *J. Chem. Theory Comput.* **8,** 948–958
34. Jorgensen, W. L., Chandrasekhar, J., Madura, J. D., Impey, R. W., and Klein, M. L. (1983) Comparison of simple potential functions for simulating liquid water. *J. Chem. Phys.* **79,** 926–935
35. Ke, S., Zangerl, E. M., and Stary-Weinzinger, A. (2013) Distinct interactions of Na^+ and Ca^{2+} ions with the selectivity filter of the bacterial sodium channel NaVAb. *Biochem. Biophys. Res. Commun.* **430,** 1272–1276
36. DeLano, W. L. (2010) *The PyMOL Molecular Graphics System*, version 1.3r1, Schrodinger, LLC, New York
37. Smart, O. S., Goodfellow, J. M., and Wallace, B. A. (1993) The pore dimensions of gramicidin A. *Biophys. J.* **65,** 2455–2460
38. Knape, K., Linder, T., Wolschann, P., Beyer, A., and Stary-Weinzinger, A. (2011) *In silico* analysis of conformational changes induced by mutation of aromatic binding residues: consequences for drug binding in the hERG K^+ channel. *PLoS One* **6,** e28778
39. Bean, B. P., Cohen, C. J., and Tsien, R. W. (1983) Lidocaine block of cardiac sodium channels. *J. Gen. Physiol.* **81,** 613–642
40. Bai, C. X., Glaaser, I. W., Sawanobori, T., and Sunami, A. (2003) Involvement of local anesthetic binding sites on IVS6 of sodium channels in fast and slow inactivation. *Neurosci. Lett.* **337,** 41–45
41. Tsang, S. Y., Tsushima, R. G., Tomaselli, G. F., Li, R. A., and Backx, P. H. (2005) A multifunctional aromatic residue in the external pore vestibule of Na^+ channels contributes to the local anesthetic receptor. *Mol. Pharmacol.* **67,** 424–434
42. Cuello, L. G., Jogini, V., Cortes, D. M., Pan, A. C., Gagnon, D. G., Dalmas, O., Cordero-Morales, J. F., Chakrapani, S., Roux, B., and Perozo, E. (2010) Structural basis for the coupling between activation and inactivation gates in K^+ channels. *Nature* **466,** 272–275
43. Ong, B. H., Tomaselli, G. F., and Balser, J. R. (2000) A structural rearrangement in the sodium channel pore linked to slow inactivation and use dependence. *J. Gen. Physiol.* **116,** 653–662
44. Fukuda, K., Nakajima, T., Viswanathan, P. C., and Balser, J. R. (2005) Compound-specific Na^+ channel pore conformational changes induced by local anaesthetics. *J. Physiol.* **564,** 21–31
45. Yang, Y. C., Hsieh, J. Y., and Kuo, C. C. (2009) The external pore loop interacts with S6 and S3-S4 linker in domain 4 to assume an essential role in gating control and anticonvulsant action in the Na^+ channel. *J. Gen. Physiol.* **134,** 95–113
46. Tsushima, R. G., Li, R. A., and Backx, P. H. (1997) Altered ionic selectivity of the sodium channel revealed by cysteine mutations within the pore. *J. Gen. Physiol.* **109,** 463–475
47. Chiamvimonvat, N., Pérez-García, M. T., Ranjan, R., Marban, E., and Tomaselli, G. F. (1996) Depth asymmetries of the pore-lining segments of the Na^+ channel revealed by cysteine mutagenesis. *Neuron* **16,** 1037–1047
48. McPhee, J. C., Ragsdale, D. S., Scheuer, T., and Catterall, W. A. (1995) A critical role for transmembrane segment IVS6 of the sodium channel α subunit in fast inactivation. *J. Biol. Chem.* **270,** 12025–12034
49. McPhee, J. C., Ragsdale, D. S., Scheuer, T., and Catterall, W. A. (1994) A mutation in segment IVS6 disrupts fast inactivation of sodium channels. *Proc. Natl. Acad. Sci. U.S.A.* **91,** 12346–12350
50. O'Reilly, J. P., Wang, S. Y., and Wang, G. K. (2000) A point mutation in domain 4-segment 6 of the skeletal muscle sodium channel produces an atypical inactivation state. *Biophys. J.* **78,** 773–784
51. Wang, S. Y., Bonner, K., Russell, C., and Wang, G. K. (2003) Tryptophan scanning of D1S6 and D4S6 C-termini in voltage-gated sodium channels. *Biophys. J.* **85,** 911–920
52. Fan, Z., George, A. L., Jr., Kyle, J. W., and Makielski, J. C. (1996) Two human paramyotonia congenita mutations have opposite effects on lidocaine block of Na^+ channels expressed in a mammalian cell line. *J. Physiol.* **496,** 275–286
53. Balser, J. R., Nuss, H. B., Orias, D. W., Johns, D. C., Marban, E., Tomaselli, G. F., and Lawrence, J. H. (1996) Local anesthetics as effectors of allosteric gating. Lidocaine effects on inactivation-deficient rat skeletal muscle Na channels. *J. Clin. Investig.* **98,** 2874–2886
54. Fozzard, H. A., and Lipkind, G. M. (2010) The tetrodotoxin binding site is within the outer vestibule of the sodium channel. *Mar. Drugs* **8,** 219–234
55. Catterall, W. A., Goldin, A. L., and Waxman, S. G. (2005) International Union of Pharmacology. XLVII. Nomenclature and structure-function relationships of voltage-gated sodium channels. *Pharmacol. Rev.* **57,** 397–409
56. Prütting, S., and Grissmer, S. (2011) A novel current pathway parallel to the central pore in a mutant voltage-gated potassium channel. *J. Biol. Chem.* **286,** 20031–20042
57. Furini, S., Beckstein, O., and Domene, C. (2009) Permeation of water through the KcsA K^+ channel. *Proteins* **74,** 437–448
58. Amin, A. S., Verkerk, A. O., Bhuiyan, Z. A., Wilde, A. A., and Tan, H. L. (2005) Novel Brugada syndrome-causing mutation in ion-conducting pore of cardiac Na^+ channel does not affect ion selectivity properties. *Acta Physiol. Scand.* **185,** 291–301

5 Discussion

In this thesis, comprehensive investigations of the functions of the selectivity filter (SF) in BacNa$_V$s with regard to ion selectivity, conduction and potential access pathways for quaternary amine local anesthetics have been performed.

5.1 EEEE locus determines Na^+ and Ca^{2+} selectivity (Discussion for chapter 4.1)

The carboxyl oxygens of the glutamic acids (E177 in Na$_V$Ab and E53 in Na$_V$Ms), which have been proposed to form a high-field strength site (site S$_{HFS}$) for ion conduction and selectivity (Eisenman and Horn, 1983), play a central role in these key channel functions consensually supported by our studies (Ke et al., 2013, 2014) and other studies (Carnevale et al., 2011; Corry and Thomas, 2011; Furini and Domene, 2012; Qiu et al., 2012; Corry, 2013; Stock et al., 2013; Chakrabarti et al., 2013; Ulmschneider et al., 2013; Tang et al., 2014). This EEEE ring defines an electro-negative region at the extracellular entrance of the SF of BacNa$_V$s, which rapidly attracts cations in the vicinity of the channel outer vestibule. As proposed by structural studies (Payandeh et al., 2011), Na^+ ions tend to be directly coordinated with side chain oxygens of glutamic acids in an off-axis manner (Carnevale et al., 2011; Ke et al., 2013; Ulmschneider et al., 2013). One water molecule from Na^+ ion's first hydration shell is replaced by a carboxyl oxygen from a glutamic acid side-chain. This site is energetically favorable to bind not only Na^+, but also K^+ and Ca^{2+} ions. However, these ions experience distinct energy barriers when moving inwardly at a site, which is located at the equivalent positions of glutamic acid side chain carbon atoms (site S$_{S178/L176}$, Figure 2C, in chapter 4.1 (Ke et al., 2013); site S$_{BAR}$ Figure 3, in chapter 4.2 (Ke et al., 2014)). As introduced in chapter 1.4.4, two computational studies have suggested that K^+ ions fail to maintain the optimal geometry at this narrow region (Corry and Thomas, 2011; Furini and Domene, 2012). Our study (Figure 2C & E, chapter 4.1 (Ke

et al., 2013)), for the first time, revealed that this site will also provide discrimination between Na^+ and Ca^{2+} ions based on PMF calculations. The geometrically non-optimal coordination leads to a larger barrier for Ca^{2+} (4.3 kcal/mol) with respect to Na^+ (1.4 kcal/mol). In addition, Ca^{2+} can induce a conformational change of the EEEE locus due to strong electrostatic interactions. The side chains of the glutamic acids adopt a novel inward-facing conformation (χ_2 angle ~ 60, flipped) compared to the outward facing configuration (χ_2 angle ~ 290, flipped) in the crystal structure.

Later, a paper published by Corry (Corry, 2013), has demonstrated similar mechanisms for Ca^{2+} and Na^+ selectivity. The ion–protein interactions are not able to compensate for the reduced ion–water interactions that are enforced by the limited space at this hydrophobic site. Ca^{2+} compensates the larger free energy penalty, compared to Na^+, to lose half of the water (on average) when permeating this barrier. Interestingly, in the same study, a two-ion PMF calculation demonstrated that a sodium ion is able to bypass a calcium ion, which bound tightly to a glutamic acid side chain in the SF of Na_VAb; meanwhile, Ca^{2+} can easily displace a sodium ion, which pre-occupied site S_{HFS}, and push it through the pore. These findings suggested, in general, the radius of an electronegative Ca^{2+} selective filter will be narrower than Na^+ selective ions. (Corry, 2013)

Analogous mutations in the SF of the bacterial Na_VAb channel (sequence: TLESWSM) have been introduced, in order to create a Ca^{2+} selective Ca_VAb (sequence: TLDDWSD) channel for structural and electrophysiological studies (Tang et al., 2014). These additional negative charges in the SF, which totally abolish the original configuration of site S_{HFS}, accentuate the differences of the binding affinities for Ca^{2+} over Na^+ to 100:1. Three narrow binding sites have been suggested to be able to accommodate Ca^{2+} ions with their first hydration shell, meanwhile excluding Na^+ ions (Tang et al., 2014). Although in vertebrate calcium channels, the four glutamate residues are proposed to be pseudo-

symmetrically positioned (Ellinor et al., 1995), they might share similar molecular mechanisms for Ca^{2+} permeation and selectivity (Tang et al., 2014).

5.2 Significance of structural configurations the EEEE locus (Discussion for chapter 4.2)

Later in 2013, Chakrabarti et al, reported that a similar alternative configuration of the EEEE locus can occur in equilibrium simulations with Na^+ (Chakrabarti et al., 2013), as observed in our simulations with Ca^{2+} (Ke et al., 2013). However, it was not clear why these structural changes of the SF were not reported in previous simulations as well as the detailed mechanism underlying this structural rearrangement (Furini and Domene, 2013). Our further simulation study (Chapter 4.2, Ke et al., 2014) with depolarizing membrane potential provides evidence that increased propensity of outward sodium transitions might be the reason to trigger these conformational changes. The non-flipped conformation, which forms the native barrier site S_{BAR}, prevents Na^+ efflux with a larger energy barrier compared to Na^+ influx (Furini and Domene, 2012; Stock et al., 2013; Ke et al., 2014). The inward-facing (flipped) configuration of glutamic acid offers direct coordination for outward traversing Na^+ ions, and energetically facilitates Na^+ outward conduction (Figure 7, 8 & 9, Chapter 4.2, Ke et al., 2014). Equilibrium simulations suggest this configuration may serve as a first step to drive channel slow inactivation by triggering a kink in the S6 segment (Boiteux et al., 2014a). In our publication, restrains imposed on the lower S6 helix, necessary due to the use of a truncated open Na_VMs structure, precluded observations of the formation of this slow inactivated state. Interestingly, in our preliminary simulations with no restraints on the pore gate, the occurrences of a two-fold assembly of the lower S6 segments akin to the inactivated Na_VAb x-ray structure (Payandeh et al., 2012) was observed. Further simulation studies with an unrestrained full-length structure and experimental

validations including introducing artificial substitutions of glutamic acids will validate this hypothesis.

5.3 Probing the role of the selectivity filter (SF) in the external drug access pathway (EAP) in mammalian Na_Vs (Discussion for chapter 4.3)

Previous electrophysiology and homology modeling studies based on K^+ channel structures suggested an external access pathway (EAP) for local anesthetics. Residue I1575 was identified as a structural determinant for creating a so-called engineered EAP for charged local anesthetics, QX-222 in rat Na_V 1.4 channels (Sunami et al., 2001; Lipkind and Fozzard, 2000; Tikhonov and Zhorov, 2005). In our third study (Chapter 4.3, Lukacs et al., 2014), experimental data by the Todt lab showed that W1531G can generate a non-selective SF in the rat Na_V1.4 channel. Homology modeling studies using the newly published Na_VAb structure as template suggested that this mutant might collectively contribute to the formation of this EAP with previous published structural determinants at position 1575.

Equilibrium simulations, performed with mutants W182G (W1531 in Na_V1.4) and L179S in one subunit of the bacterial channel Na_VRh, showed that water molecules can solvate the cavity where originally occupied by tryptophan side chains. The HOLE (Smart et al., 1993) analysis suggests there might be an additional contiguous pore connecting the outer and inner vestibules other than the SF, when the bulky tryptophan side chain is removed (**Figure 5.1**) . Subsequent molecular modeling and docking studies showed the QX-222 might utilize this EAP to access the pore cavity (Figure 10 in chapter 4.3). Our study sheds light on the applicability of BacNa_Vs structures as templates for modeling the external access pathway of charged local anesthetics in mammalian sodium channels. Neutral local anesthetic (benzocaine) and antiepileptic (phenytoin) drugs have been shown, in MD simulations, to access the bacterial channel via the hydrophobic pathway facilitated by the fenestrations of BacNa_Vs (Martin

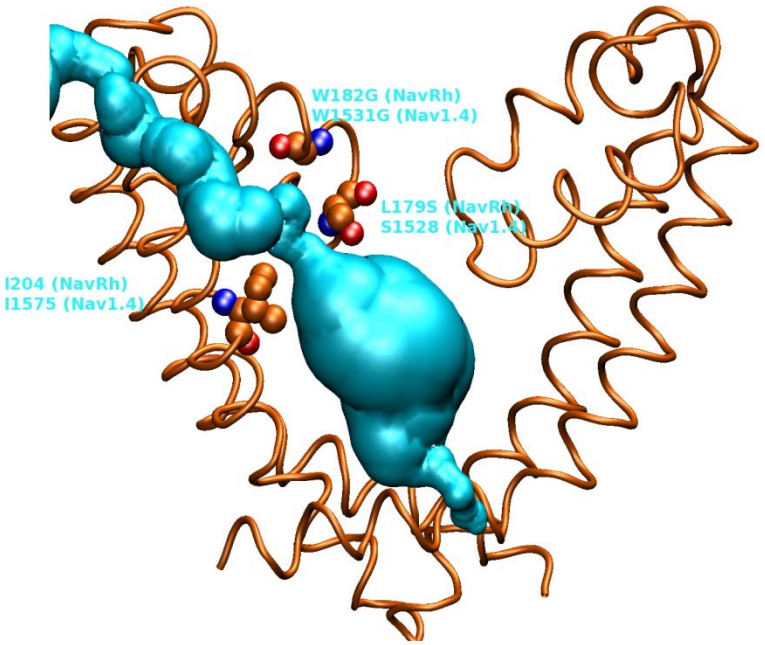

Figure 5.1. The continuous pore indicated by HOLE analysis (Smart et al., 1993) from the simulated model with W-G and L-S mutants based on the Na_VRh structure. Relevant structural determinants and their numberings of both bacterial (Na_VRh) and mammalian ($rNa_V1.4$) Na_Vs are highlighted.

and Corry, 2014; Boiteux et al., 2014b). QX-314, a permanent charged local anesthetic drug, was proposed to use the similar pathways to block the closed channel with mutated μ-conotoxin occluding the outer vestibule in vertebrate Na_Vs channels (Sunami et al., 2001; Zhorov and Tikhonov, 2013). However, electrophysiological studies failed to show evidence that QX-314 can utilize this hydrophobic route in $BacNa_V$s (Lee et al., 2012). Detailed mechanisms of possible access pathways for charged molecules require further investigations.

5.4 Prospects

There are future prospects that can be addressed in terms of better sampling during simulations. Better Ca^{2+} ion parameters will offer better quantitative interpretations of the simulation results (Mamatkulov et al., 2013; Corry, 2013). Current Ca^{2+} parameters are quite deviated in terms of Lennard Jones parameters among mainstream force fields. Almost all of them fail to describe specific effects of ion interactions with complex

proteins such as ion channels and transporters (Mamatkulov et al., 2013). One future direction, which might require a large amount of referential quantum calculations, can determine a set of specific pairwise LJ parameters between calcium and other interacting atoms respectively. In addition, due to their high charge density, divalent ions are more likely to polarize surrounding molecules than is the case for monovalent ions. Therefore, the use of polarizable force fields to parameterize correct polarization of the atoms interacting with Ca^{2+} will also improve this issue (Corry, 2013).

An applied membrane potential ensures a realistic setup of the driving force for ion flux and even the charged molecules. However, the transmembrane potential may experience large fluctuations with finite simulation size during ion permeation. Similar fluctuations may also occur when simulations involve large conformational changes of the protein. In addition, according to equation (27), these different conformational configurations may also change local electrostatic profiles (e.g. shifting or creating new electrostatic potential barriers). Additionally, current non-polarizable force fields overestimate the electrostatic potential barriers in the lipid head group region (Klauda et al., 2010; Jensen et al., 2013). Therefore, a polarizable force field is essential in reproducing not only the correct area per lipid values of membrane but also the realistic electrostatic potentials of the system (Jensen et al., 2013). The reproducibility of water polarization is also of great interest to characterize both the dipole moments and the free energy profiles of water molecules interacting with ions in the SF (Lamoureux and Roux, 2003). These improvements enable simulations with lowered physiological membrane potentials and better ensemble average with fewer fluctuations. In addition, estimations of two-dimensional electrostatic potential profiles (Aksimentiev and Schulten, 2005; Delemotte et al., 2008) and charge free energy profiles (Dong et al., 2013; Roux, 2008) will provide good opportunities to characterize residue-based fractional

charge free energy differences during conduction of these charge molecules compared to equilibrium simulations.

Summarizing, this thesis provides novel insights into substantial roles of the dynamics of EEEE locus, which determines two crucial ion interacting sites, S_{HFS} and S_{BAR}, in ion selectivity (Na^+ and Ca^{2+}) and conduction directionalities of $BacNa_Vs$. Additionally, a SF involved engineered external pathway for charged local anesthetics has been probed. As Na^+ channels are important drug targets to treat a plethora of pathophysiological conditions, our studies shed lights on the feasibility of using bacterial Na_Vs structures as models to characterize mammalian channel functions. Further studies with more structural information and better sampling techniques will provide detailed insights into Na^+ and Ca^{2+} discrimination and conductance as well as drug interactions with mammalian sodium and calcium channels.

6 References

Aksimentiev, A., and K. Schulten. 2005. Imaging alpha-hemolysin with molecular dynamics: ionic conductance, osmotic permeability, and the electrostatic potential map. *Biophys. J.* 88:3745–3761. doi:10.1529/biophysj.104.058727.

Andavan, G.S.B., and R. Lemmens-Gruber. 2011. Voltage-gated sodium channels: mutations, channelopathies and targets. *Curr. Med. Chem.* 18:377–397.

Aqvist, J., and V. Luzhkov. 2000. Ion permeation mechanism of the potassium channel. *Nature*. 404:881–884. doi:10.1038/35009114.

Bagnéris, C., P.G. DeCaen, B.A. Hall, C.E. Naylor, D.E. Clapham, C.W.M. Kay, and B.A. Wallace. 2013. Role of the C-terminal domain in the structure and function of tetrameric sodium channels. *Nat. Commun.* 4. doi:10.1038/ncomms3465.

Bagnéris, C., P.G. DeCaen, C.E. Naylor, D.C. Pryde, I. Nobeli, D.E. Clapham, and B.A. Wallace. 2014. Prokaryotic NavMs channel as a structural and functional model for eukaryotic sodium channel antagonism. *Proc. Natl. Acad. Sci.* 111:8428–8433. doi:10.1073/pnas.1406855111.

Balser, J.R., H.B. Nuss, D.W. Orias, D.C. Johns, E. Marban, G.F. Tomaselli, and J.H. Lawrence. 1996. Local anesthetics as effectors of allosteric gating. Lidocaine effects on inactivation-deficient rat skeletal muscle Na channels. *J. Clin. Invest.* 98:2874–2886.

Beneski, D.A., and W.A. Catterall. 1980. Covalent labeling of protein components of the sodium channel with a photoactivable derivative of scorpion toxin. *Proc. Natl. Acad. Sci. U. S. A.* 77:639–643.

Berendsen, H.J.C., J.P.M. Postma, W.F. van Gunsteren, A. DiNola, and J.R. Haak. 1984. Molecular dynamics with coupling to an external bath. *J. Chem. Phys.* 81:3684–3690. doi:10.1063/1.448118.

Bernèche, S., and B. Roux. 2001. Energetics of ion conduction through the K+ channel. *Nature*. 414:73–77. doi:10.1038/35102067.

Boiteux, C., I. Vorobyov, and T.W. Allen. 2014a. Ion conduction and conformational flexibility of a bacterial voltage-gated sodium channel. *Proc. Natl. Acad. Sci.* 111:3454–3459. doi:10.1073/pnas.1320907111.

Boiteux, C., I. Vorobyov, R.J. French, C. French, V. Yarov-Yarovoy, and T.W. Allen. 2014b. Local anesthetic and antiepileptic drug access and binding to a bacterial voltage-gated sodium channel. *Proc. Natl. Acad. Sci.* 111:13057–13062. doi:10.1073/pnas.1408710111.

Bussi, G., D. Donadio, and M. Parrinello. 2007. Canonical sampling through velocity rescaling. *J. Chem. Phys.* 126:014101. doi:10.1063/1.2408420.

Carboni, M., Z.-S. Zhang, V. Nepliouéva, C.F. Starmer, and A.O. Grant. 2005. Slow sodium channel inactivation and use-dependent block modulated by the same domain IV S6 residue. *J. Membr. Biol.* 207:107–117. doi:10.1007/s00232-005-0805-0.

Carnevale, V., W. Treptow, and M.L. Klein. 2011. Sodium Ion Binding Sites and Hydration in the Lumen of a Bacterial Ion Channel from Molecular Dynamics Simulations. *J Phys Chem Lett*. 2:2504–2508. doi:10.1021/jz2011379.

Catterall, W.A. 2012. Voltage-gated sodium channels at 60: structure, function and pathophysiology. *J. Physiol.* 590:2577–2589. doi:10.1113/jphysiol.2011.224204.

Catterall, W.A., S. Cestèle, V. Yarov-Yarovoy, F.H. Yu, K. Konoki, and T. Scheuer. 2007. Voltage-gated ion channels and gating modifier toxins. *Toxicon*. 49:124–141. doi:10.1016/j.toxicon.2006.09.022.

Chakrabarti, N., C. Ing, J. Payandeh, N. Zheng, W.A. Catterall, and R. Pomès. 2013. Catalysis of Na+ permeation in the bacterial sodium channel NaVAb. *Proc. Natl. Acad. Sci.* 201309452. doi:10.1073/pnas.1309452110.

Chen, R., and S.-H. Chung. 2012. Binding Modes of μ-Conotoxin to the Bacterial Sodium Channel (NaVAb). *Biophys. J.* 102:483–488. doi:10.1016/j.bpj.2011.12.041.

Chen, Z., B.-H. Ong, N.G. Kambouris, E. Marbán, G.F. Tomaselli, and J.R. Balser. 2000. Lidocaine induces a slow inactivated state in rat skeletal muscle sodium channels. *J. Physiol.* 524:37–49. doi:10.1111/j.1469-7793.2000.t01-1-00037.x.

Cornell, W.D., P. Cieplak, C.I. Bayly, I.R. Gould, K.M. Merz, D.M. Ferguson, D.C. Spellmeyer, T. Fox, J.W. Caldwell, and P.A. Kollman. 1995. A Second Generation Force Field for the Simulation of Proteins, Nucleic Acids, and Organic Molecules. *J. Am. Chem. Soc.* 117:5179–5197. doi:10.1021/ja00124a002.

Corry, B. 2013. Na(+)/Ca(2+) selectivity in the bacterial voltage-gated sodium channel NavAb. *PeerJ*. 1:e16. doi:10.7717/peerj.16.

Corry, B., T.W. Allen, S. Kuyucak, and S.H. Chung. 2001. Mechanisms of permeation and selectivity in calcium channels. *Biophys. J.* 80:195–214.

Corry, B., S. Lee, and C.A. Ahern. 2014. Pharmacological insights and quirks of bacterial sodium channels. *Handb. Exp. Pharmacol.* 221:251–267. doi:10.1007/978-3-642-41588-3_12.

Corry, B., and M. Thomas. 2011. Mechanism of Ion Permeation and Selectivity in a Voltage Gated Sodium Channel. *J Am Chem Soc*. doi:10.1021/ja210020h.

Crozier, P.S., D. Henderson, R.L. Rowley, and D.D. Busath. 2001. Model channel ion currents in NaCl-extended simple point charge water solution with applied-field molecular dynamics. *Biophys. J.* 81:3077–3089.

Cuello, L.G., V. Jogini, D.M. Cortes, and E. Perozo. 2010. Structural mechanism of C-type inactivation in K+ channels. *Nature*. 466:203–208.

Darden, T., D. York, and L. Pedersen. 1993. Particle mesh Ewald: An N log (N) method for Ewald sums in large systems. *J. Chem. Phys.* 98:10089–10089.

Delemotte, L., F. Dehez, W. Treptow, and M. Tarek. 2008. Modeling Membranes under a Transmembrane Potential. *J. Phys. Chem. B*. 112:5547–5550. doi:10.1021/jp710846y.

Van Der Spoel, D., E. Lindahl, B. Hess, G. Groenhof, A.E. Mark, and H.J.. Berendsen. 2005. GROMACS: fast, flexible, and free. *J. Comput. Chem.* 26:1701.

Dong, H., G. Fiorin, V. Carnevale, W. Treptow, and M.L. Klein. 2013. Pore waters regulate ion permeation in a calcium release-activated calcium channel. *Proc. Natl. Acad. Sci.* 110:17332–17337. doi:10.1073/pnas.1316969110.

Doyle, D.A., J.M. Cabral, R.A. Pfuetzner, A. Kuo, J.M. Gulbis, S.L. Cohen, B.T. Chait, and R. MacKinnon. 1998. The structure of the potassium channel: molecular basis of K+ conduction and selectivity. *science*. 280:69.

Durell, S.R., and H.R. Guy. 2001. A putative prokaryote voltage-gated Ca(2+) channel with only one 6TM motif per subunit. *Biochem. Biophys. Res. Commun.* 281:741–746. doi:10.1006/bbrc.2001.4408.

Eisenman, G., and R. Horn. 1983. Ionic selectivity revisited: The role of kinetic and equilibrium processes in ion permeation through channels. *J. Membr. Biol.* 76:197–225. doi:10.1007/BF01870364.

Ellinor, P.T., J. Yang, W.A. Sather, J.-F. Zhang, and R.W. Tsien. 1995. Ca2+ channel selectivity at a single locus for high-affinity Ca2+ interactions. *Neuron*. 15:1121–1132. doi:10.1016/0896-6273(95)90100-0.

Errington, A.C., T. Stöhr, C. Heers, and G. Lees. 2008. The investigational anticonvulsant lacosamide selectively enhances slow inactivation of voltage-gated sodium channels. *Mol. Pharmacol.* 73:157–169. doi:10.1124/mol.107.039867.

Featherstone, D.E., J.E. Richmond, and P.C. Ruben. 1996. Interaction between fast and slow inactivation in Skm1 sodium channels. *Biophys. J.* 71:3098–3109. doi:10.1016/S0006-3495(96)79504-8.

Feenstra, K.A., B. Hess, and H.J.C. Berendsen. 1999. Improving efficiency of large time-scale molecular dynamics simulations of hydrogen-rich systems. *J. Comput. Chem.* 20:786–798. doi:10.1002/(SICI)1096-987X(199906)20:8<786::AID-JCC5>3.0.CO;2-B.

Fozzard, H.A., P.J. Lee, and G.M. Lipkind. 2005. Mechanism of local anesthetic drug action on voltage-gated sodium channels. *Curr. Pharm. Des.* 11:2671–2686.

Frazier, D.T., T. Narahashi, and M. Yamada. 1970. The site of action and active form of local anesthetics. II. Experiments with quaternary compounds. *J. Pharmacol. Exp. Ther.* 171:45–51.

Frenkel, D., and B. Smit. 2001. Understanding Molecular Simulation: From Algorithms to Applications. Academic Press. 662 pp.

Furini, S., and C. Domene. 2012. On Conduction in a Bacterial Sodium Channel. *PLoS Comput Biol*. 8:e1002476. doi:10.1371/journal.pcbi.1002476.

Furini, S., and C. Domene. 2013. K+ and Na+ Conduction in Selective and Nonselective Ion Channels Via Molecular Dynamics Simulations. *Biophys. J.* 105:1737–1745. doi:10.1016/j.bpj.2013.08.049.

Gilchrist, J., B.M. Olivera, and F. Bosmans. 2014. Animal Toxins Influence Voltage-Gated Sodium Channel Function. *In* Voltage Gated Sodium Channels. P.C. Ruben, editor. Springer Berlin Heidelberg. 203–229.

Goldin, A.L. 1999. Diversity of mammalian voltage-gated sodium channels. *Ann. N. Y. Acad. Sci.* 868:38–50.

Goldin, A.L., T. Snutch, H. Lübbert, A. Dowsett, J. Marshall, V. Auld, W. Downey, L.C. Fritz, H.A. Lester, and R. Dunn. 1986. Messenger RNA coding for only the alpha subunit of the rat brain Na channel is sufficient for expression of functional channels in Xenopus oocytes. *Proc. Natl. Acad. Sci. U. S. A.* 83:7503–7507.

Goldschen-Ohm, M.P., and B. Chanda. 2014. Probing gating mechanisms of sodium channels using pore blockers. *Handb. Exp. Pharmacol.* 221:183–201. doi:10.1007/978-3-642-41588-3_9.

Gouaux, E., and R. MacKinnon. 2005. Principles of Selective Ion Transport in Channels and Pumps. *Science*. 310:1461–1465. doi:10.1126/science.1113666.

Heinemann, S.H., H. Terlau, W. Stühmer, K. Imoto, and S. Numa. 1992. Calcium channel characteristics conferred on the sodium channel by single mutations. *Nature*. 356:441–443.

Hess, B., H. Bekker, H.J.C. Berendsen, and J.G.E.M. Fraaije. 1997. LINCS: A linear constraint solver for molecular simulations. *J. Comput. Chem.* 18:1463–1472. doi:10.1002/(SICI)1096-987X(199709)18:12<1463::AID-JCC4>3.0.CO;2-H.

Hess, B., C. Kutzner, D. van der Spoel, and E. Lindahl. 2008. GROMACS 4: Algorithms for Highly Efficient, Load-Balanced, and Scalable Molecular Simulation. *J Chem Theory Comput*. 4:435–447. doi:10.1021/ct700301q.

Hess, P., and R.W. Tsien. 1984. Mechanism of ion permeation through calcium channels. *Nature*. 309:453–456. doi:10.1038/309453a0.

Hille, B. 1972. The permeability of the sodium channel to metal cations in myelinated nerve. *J. Gen. Physiol.* 59:637–658.

Hille, B. 1977a. Local anesthetics: hydrophilic and hydrophobic pathways for the drug-receptor reaction. *J. Gen. Physiol.* 69:497–515. doi:10.1085/jgp.69.4.497.

Hille, B. 1977b. The pH-dependent rate of action of local anesthetics on the node of Ranvier. *J. Gen. Physiol.* 69:475–496.

Hille, B. 2001. Ion channels of excitable membranes. Sinauer. 814 pp.

Hodgkin, A.L., and A.F. Huxley. 1952a. The components of membrane conductance in the giant axon of Loligo. *J. Physiol.* 116:473–496.

Hodgkin, A.L., and A.F. Huxley. 1952b. Currents carried by sodium and potassium ions through the membrane of the giant axon of Loligo. *J. Physiol.* 116:449–472.

Hodgkin, A.L., and A.F. Huxley. 1952c. The dual effect of membrane potential on sodium conductance in the giant axon of Loligo. *J. Physiol.* 116:497–506.

Hodgkin, A.L., and A.F. Huxley. 1952d. A quantitative description of membrane current and its application to conduction and excitation in nerve. *J. Physiol.* 117:500–544.

Hoover, William G., and W.G. Hoover. 1985. Canonical dynamics: Equilibrium phase-space distributions. *Phys Rev A*. 31:1695–1697. doi:10.1103/PhysRevA.31.1695.

Hub, J.S., B.L. de Groot, and D. van der Spoel. 2010. g_wham—A Free Weighted Histogram Analysis Implementation Including Robust Error and Autocorrelation Estimates. *J Chem Theory Comput*. 6:3713–3720. doi:10.1021/ct100494z.

Hummer, G. 2014. Potassium ions line up. *Science*. 346:303–303. doi:10.1126/science.1260555.

Irie, K., K. Kitagawa, H. Nagura, T. Imai, T. Shimomura, and Y. Fujiyoshi. 2010. Comparative study of the gating motif and C-type inactivation in prokaryotic voltage-gated sodium channels. *J. Biol. Chem.* 285:3685–3694. doi:10.1074/jbc.M109.057455.

Isom, L.L., K.S. De Jongh, D.E. Patton, B.F. Reber, J. Offord, H. Charbonneau, K. Walsh, A.L. Goldin, and W.A. Catterall. 1992. Primary structure and functional expression of the beta 1 subunit of the rat brain sodium channel. *Science*. 256:839–842.

Isom, L.L., D.S. Ragsdale, K.S. De Jongh, R.E. Westenbroek, B.F. Reber, T. Scheuer, and W.A. Catterall. 1995. Structure and function of the beta 2 subunit of brain sodium channels, a transmembrane glycoprotein with a CAM motif. *Cell*. 83:433–442.

Jarzynski, C. 1997. Nonequilibrium Equality for Free Energy Differences. *Phys. Rev. Lett.* 78:2690–2693. doi:10.1103/PhysRevLett.78.2690.

Jensen, M.Ø., D.W. Borhani, K. Lindorff-Larsen, P. Maragakis, V. Jogini, M.P. Eastwood, R.O. Dror, and D.E. Shaw. 2010. Principles of conduction and hydrophobic gating in K+ channels. *Proc. Natl. Acad. Sci. U. S. A.* 107:5833–5838. doi:10.1073/pnas.0911691107.

Jensen, M.Ø., V. Jogini, M.P. Eastwood, and D.E. Shaw. 2013. Atomic-level simulation of current–voltage relationships in single-file ion channels. *J. Gen. Physiol.* 141:619–632. doi:10.1085/jgp.201210820.

Ke, S., E.N. Timin, and A. Stary-Weinzinger. 2014. Different Inward and Outward Conduction Mechanisms in NaVMs Suggested by Molecular Dynamics Simulations. *PLoS Comput Biol*. 10:e1003746. doi:10.1371/journal.pcbi.1003746.

Ke, S., E.-M. Zangerl, and A. Stary-Weinzinger. 2013. Distinct interactions of Na+ and Ca2+ ions with the selectivity filter of the bacterial sodium channel NaVAb. *Biochem. Biophys. Res. Commun.* 430:1272–1276. doi:10.1016/j.bbrc.2012.12.055.

Khalili-Araghi, F., E. Tajkhorshid, and K. Schulten. 2006. Dynamics of K+ Ion Conduction through Kv1.2. *Biophys. J.* 91:L72–L74. doi:10.1529/biophysj.106.091926.

Kirkwood, J.G. 1935. Statistical Mechanics of Fluid Mixtures. *J. Chem. Phys.* 3:300–313. doi:10.1063/1.1749657.

Klauda, J.B., R.M. Venable, J.A. Freites, J.W. O'Connor, D.J. Tobias, C. Mondragon-Ramirez, I. Vorobyov, A.D. MacKerell, and R.W. Pastor. 2010. Update of the CHARMM All-Atom Additive Force Field for Lipids: Validation on Six Lipid Types. *J. Phys. Chem. B*. 114:7830–7843. doi:10.1021/jp101759q.

Köpfer, D.A., C. Song, T. Gruene, G.M. Sheldrick, U. Zachariae, and B.L. de Groot. 2014. Ion permeation in K+ channels occurs by direct Coulomb knock-on. *Science*. 346:352–355. doi:10.1126/science.1254840.

Korkosh, V.S., B.S. Zhorov, and D.B. Tikhonov. 2014. Folding similarity of the outer pore region in prokaryotic and eukaryotic sodium channels revealed by docking of conotoxins GIIIA, PIIIA, and KIIIA in a NavAb-based model of Nav1.4. *J. Gen. Physiol.* 144:231–244. doi:10.1085/jgp.201411226.

Kumar, S., J.M. Rosenberg, D. Bouzida, R.H. Swendsen, and P.A. Kollman. 1992. THE weighted histogram analysis method for free-energy calculations on biomolecules. I. The method. *J. Comput. Chem.* 13:1011–1021. doi:10.1002/jcc.540130812.

Kutzner, C., H. Grubmüller, B.L. de Groot, and U. Zachariae. 2011. Computational Electrophysiology: The Molecular Dynamics of Ion Channel Permeation and Selectivity in Atomistic Detail. *Biophys. J.* 101:809–817.

Kutzner, C., D. van der Spoel, M. Fechner, E. Lindahl, U.W. Schmitt, B.L. de Groot, and H. Grubmüller. 2007. Speeding up parallel GROMACS on high-latency networks. *J. Comput. Chem.* 28:2075–2084. doi:10.1002/jcc.20703.

Lamoureux, G., and B. Roux. 2003. Modeling induced polarization with classical Drude oscillators: Theory and molecular dynamics simulation algorithm. *J. Chem. Phys.* 119:3025–3039. doi:10.1063/1.1589749.

Lee, S., S.J. Goodchild, and C.A. Ahern. 2012. Local anesthetic inhibition of a bacterial sodium channel. *J. Gen. Physiol.* 139:507–516. doi:10.1085/jgp.201210779.

Liebeskind, B.J., D.M. Hillis, and H.H. Zakon. 2013. Independent acquisition of sodium selectivity in bacterial and animal sodium channels. *Curr. Biol.* 23:R948–R949. doi:10.1016/j.cub.2013.09.025.

Li, H.-L., A. Galue, L. Meadows, and D.S. Ragsdale. 1999. A molecular basis for the different local anesthetic affinities of resting versus open and inactivated states of the sodium channel. *Mol. Pharmacol.* 55:134–141.

Lipkind, G.M., and H.A. Fozzard. 2000. KcsA crystal structure as framework for a molecular model of the Na+ channel pore. *Biochemistry (Mosc.)*. 39:8161–8170.

Long, S.B. 2005. Crystal Structure of a Mammalian Voltage-Dependent Shaker Family K+ Channel. *Science*. 309:897–903. doi:10.1126/science.1116269.

Lukacs, P., V.S. Gawali, R. Cervenka, S. Ke, X. Koenig, L. Rubi, T. Zarrabi, K. Hilber, A. Stary-Weinzinger, and H. Todt. 2014. Exploring the structure of the voltage-gated Na+ channel by an engineered drug access pathway to the receptor site for local anesthetics. *J. Biol. Chem.* 289:21770–21781. doi:10.1074/jbc.M113.541763.

Mamatkulov, S., M. Fyta, and R.R. Netz. 2013. Force fields for divalent cations based on single-ion and ion-pair properties. *J. Chem. Phys.* 138:024505–024505–12. doi:doi:10.1063/1.4772808.

Martin, L.J., and B. Corry. 2014. Locating the Route of Entry and Binding Sites of Benzocaine and Phenytoin in a Bacterial Voltage Gated Sodium Channel. *PLoS Comput Biol*. 10:e1003688. doi:10.1371/journal.pcbi.1003688.

McCusker, E.C., C. Bagnéris, C.E. Naylor, A.R. Cole, N. D'Avanzo, C.G. Nichols, and B.A. Wallace. 2012. Structure of a bacterial voltage-gated sodium channel pore reveals mechanisms of opening and closing. *Nat. Commun.* 3:1102. doi:10.1038/ncomms2077.

Morais-Cabral, J.H., Y. Zhou, and R. MacKinnon. 2001. Energetic optimization of ion conduction rate by the K+ selectivity filter. *Nature*. 414:37–42. doi:10.1038/35102000.

Noda, M., T. Ikeda, H. Suzuki, H. Takeshima, T. Takahashi, M. Kuno, and S. Numa. 1986. Expression of functional sodium channels from cloned cDNA. *Nature*. 322:826–828. doi:10.1038/322826a0.

Noda, M., S. Shimizu, T. Tanabe, T. Takai, T. Kayano, T. Ikeda, H. Takahashi, H. Nakayama, Y. Kanaoka, N. Minamino, K. Kangawa, H. Matsuo, M.A. Raftery, T. Hirose, S. Inayama, H. Hayashida, T. Miyata, and S. Numa. 1984. Primary structure of Electrophorus electricus sodium channel deduced from cDNA sequence. *Nature*. 312:121–127. doi:10.1038/312121a0.

Nose, S, and S. Nose. 1984. A unified formulation of the constant temperature molecular-dynamics methods. *J. Chem. Phys.* 81:511–519. doi:10.1063/1.447334.

Noskov, S.Y., S. Bernèche, and B. Roux. 2004. Control of ion selectivity in potassium channels by electrostatic and dynamic properties of carbonyl ligands. *Nature*. 431:830–834. doi:10.1038/nature02943.

Parrinello, M., and A. Rahman. 1981. Polymorphic transitions in single crystals: A new molecular dynamics method. *J. Appl. Phys.* 52:7182–7190. doi:10.1063/1.328693.

Payandeh, J., T.M.G. El-Din, T. Scheuer, N. Zheng, and W.A. Catterall. 2012. Crystal structure of a voltage-gated sodium channel in two potentially inactivated states. *Nature*. 486:135–139. doi:10.1038/nature11077.

Payandeh, J., and D.L. Minor Jr. 2015. Bacterial Voltage-Gated Sodium Channels (BacNaVs) from the Soil, Sea, and Salt Lakes Enlighten Molecular Mechanisms of Electrical Signaling and Pharmacology in the Brain and Heart. *J. Mol. Biol.* 427:3–30. doi:10.1016/j.jmb.2014.08.010.

Payandeh, J., T. Scheuer, N. Zheng, and W.A. Catterall. 2011. The crystal structure of a voltage-gated sodium channel. *Nature*. 475:353–358.

Peters, C.H., and P.C. Ruben. 2014. Introduction to Sodium Channels. *In* Voltage Gated Sodium Channels. P.C. Ruben, editor. Springer Berlin Heidelberg. 1–6.

Qiu, H., R. Shen, and W. Guo. 2012. Ion solvation and structural stability in a sodium channel investigated by molecular dynamics calculations. *Biochim. Biophys. Acta BBA - Biomembr.* 1818:2529–2535. doi:10.1016/j.bbamem.2012.06.003.

Ragsdale, D.S., J.C. McPhee, T. Scheuer, and W.A. Catterall. 1994. Molecular determinants of state-dependent block of Na+ channels by local anesthetics. *Science*. 265:1724–1728.

Ragsdale, D.S., J.C. McPhee, T. Scheuer, and W.A. Catterall. 1996. Common molecular determinants of local anesthetic, antiarrhythmic, and anticonvulsant block of voltage-gated Na+ channels. *Proc. Natl. Acad. Sci.* 93:9270–9275.

Ren, D. 2011. Sodium Leak Channels in Neuronal Excitability and Rhythmic Behaviors. *Neuron*. 72:899–911.

Ren, D., B. Navarro, H. Xu, L. Yue, Q. Shi, and D.E. Clapham. 2001. A prokaryotic voltage-gated sodium channel. *Science*. 294:2372.

Richmond, J.E., D.E. Featherstone, H.A. Hartmann, and P.C. Ruben. 1998. Slow Inactivation in Human Cardiac Sodium Channels. *Biophys. J.* 74:2945–2952. doi:10.1016/S0006-3495(98)78001-4.

Roux, B. 1995. The calculation of the potential of mean force using computer simulations. *Comput. Phys. Commun.* 91:275–282. doi:10.1016/0010-4655(95)00053-I.

Roux, B. 1997. Influence of the membrane potential on the free energy of an intrinsic protein. *Biophys. J.* 73:2980–2989.

Roux, B. 2008. The Membrane Potential and its Representation by a Constant Electric Field in Computer Simulations. *Biophys. J.* 95:4205–4216. doi:10.1529/biophysj.108.136499.

Roux, B. 2011. Computational Electrophysiology: The Molecular Dynamics of Ion Channel Permeation and Selectivity in Atomistic Detail. *Biophys. J.* 101:755–756. doi:10.1016/j.bpj.2011.07.002.

Sachs, J.N., P.S. Crozier, and T.B. Woolf. 2004. Atomistic simulations of biologically realistic transmembrane potential gradients. *J. Chem. Phys.* 121:10847–10851. doi:10.1063/1.1826056.

Sather, W.A., and E.W. McCleskey. 2003. Permeation and selectivity in calcium channels. *Annu. Rev. Physiol.* 65:133–159.

Shaya, D., F. Findeisen, F. Abderemane-Ali, C. Arrigoni, S. Wong, S.R. Nurva, G. Loussouarn, and D.L. Minor Jr. 2014. Structure of a Prokaryotic Sodium Channel Pore Reveals Essential Gating Elements and an Outer Ion Binding Site Common to Eukaryotic Channels. *J. Mol. Biol.* 426:467–483. doi:10.1016/j.jmb.2013.10.010.

Shaya, D., M. Kreir, R.A. Robbins, S. Wong, J. Hammon, A. Brüggemann, and D.L. Minor. 2011. Voltage-Gated Sodium Channel (NaV) Protein Dissection Creates a Set of Functional Pore-Only Proteins. *Proc. Natl. Acad. Sci.* doi:10.1073/pnas.1106811108.

Silva, J. 2014. Slow Inactivation of Na+ Channels. *In* Voltage Gated Sodium Channels. P.C. Ruben, editor. Springer Berlin Heidelberg. 33–49.

Silva, J.R., and S.A.N. Goldstein. 2013. Voltage-sensor movements describe slow inactivation of voltage-gated sodium channels I: Wild-type skeletal muscle NaV1.4. *J. Gen. Physiol.* 141:309–321. doi:10.1085/jgp.201210909.

Smart, O.S., J.M. Goodfellow, and B.A. Wallace. 1993. The pore dimensions of gramicidin A. *Biophys. J.* 65:2455–2460. doi:10.1016/S0006-3495(93)81293-1.

Souaille, M., and B. Roux. 2001. Extension to the weighted histogram analysis method: combining umbrella sampling with free energy calculations. *Comput. Phys. Commun.* 135:40–57. doi:10.1016/S0010-4655(00)00215-0.

Stock, L., L. Delemotte, V. Carnevale, W. Treptow, and M.L. Klein. 2013. Conduction in a Biological Sodium Selective Channel. *J. Phys. Chem. B*. 117:3782–3789. doi:10.1021/jp401403b.

Strichartz, G.R. 1973. The inhibition of sodium currents in myelinated nerve by quaternary derivatives of lidocaine. *J. Gen. Physiol.* 62:37–57.

Suenaga, A., Y. Komeiji, M. Uebayasi, T. Meguro, M. Saito, and I. Yamato. 1998. Computational observation of an ion permeation through a channel protein. *Biosci. Rep.* 18:39–48.

Sunami, A., S.C. Dudley, and H.A. Fozzard. 1997. Sodium channel selectivity filter regulates antiarrhythmic drug binding. *Proc. Natl. Acad. Sci. U. S. A.* 94:14126–14131.

Sunami, A., I.W. Glaaser, and H.A. Fozzard. 2001. Structural and gating changes of the sodium channel induced by mutation of a residue in the upper third of IVS6, creating an external access path for local anesthetics. *Mol. Pharmacol.* 59:684–691.

Tang, L., T.M. Gamal El-Din, J. Payandeh, G.Q. Martinez, T.M. Heard, T. Scheuer, N. Zheng, and W.A. Catterall. 2014. Structural basis for Ca2+ selectivity of a voltage-gated calcium channel. *Nature*. 505:56–61. doi:10.1038/nature12775.

Thomas, M., D. Jayatilaka, and B. Corry. 2011. Mapping the importance of four factors in creating monovalent ion selectivity in biological molecules. *Biophys. J.* 100:60–69. doi:10.1016/j.bpj.2010.11.022.

Tieleman, D.P., H.J. Berendsen, and M.S. Sansom. 2001. Voltage-dependent insertion of alamethicin at phospholipid/water and octane/water interfaces. *Biophys. J.* 80:331–346.

Tikhonov, D.B., I. Bruhova, and B.S. Zhorov. 2006. Atomic determinants of state-dependent block of sodium channels by charged local anesthetics and benzocaine. *FEBS Lett.* 580:6027–6032. doi:10.1016/j.febslet.2006.10.035.

Tikhonov, D.B., and B.S. Zhorov. 2005. Modeling P-Loops Domain of Sodium Channel: Homology with Potassium Channels and Interaction with Ligands. *Biophys. J.* 88:184–197. doi:10.1529/biophysj.104.048173.

Tikhonov, D.B., and B.S. Zhorov. 2012. Architecture and Pore Block of Eukaryotic Voltage-Gated Sodium Channels in View of NavAb Bacterial Sodium Channel Structure. *Mol. Pharmacol.* 82:97–104. doi:10.1124/mol.112.078212.

Torrie, G.M., and J.P. Valleau. 1977. Nonphysical sampling distributions in Monte Carlo free-energy estimation: Umbrella sampling. *J. Comput. Phys.* 23:187–199. doi:10.1016/0021-9991(77)90121-8.

Treptow, W., and M. Tarek. 2006. K+ conduction in the selectivity filter of potassium channels is monitored by the charge distribution along their sequence. *Biophys. J.* 91:L81–83. doi:10.1529/biophysj.106.095992.

Tsai, C.-J., K. Tani, K. Irie, Y. Hiroaki, T. Shimomura, D.G. McMillan, G.M. Cook, G.F.X. Schertler, Y. Fujiyoshi, and X.-D. Li. 2013. Two Alternative Conformations of a Voltage-Gated Sodium Channel. *J. Mol. Biol.* 425:4074–4088. doi:10.1016/j.jmb.2013.06.036.

Ulmschneider, M.B., C. Bagnéris, E.C. McCusker, P.G. DeCaen, M. Delling, D.E. Clapham, J.P. Ulmschneider, and B.A. Wallace. 2013. Molecular dynamics of ion transport through the open conformation of a bacterial voltage-gated sodium channel. *Proc. Natl. Acad. Sci.* 201214667. doi:10.1073/pnas.1214667110.

Vilin, Y.Y., N. Makita, A.L. George Jr., and P.C. Ruben. 1999. Structural Determinants of Slow Inactivation in Human Cardiac and Skeletal Muscle Sodium Channels. *Biophys. J.* 77:1384–1393. doi:10.1016/S0006-3495(99)76987-0.

Wang, S.Y., and G.K. Wang. 1997. A mutation in segment I-S6 alters slow inactivation of sodium channels. *Biophys. J.* 72:1633–1640. doi:10.1016/S0006-3495(97)78809-X.

Watts, R.O. 1974. Monte Carlo studies of liquid water. *Mol. Phys.* 28:1069–1083. doi:10.1080/00268977400102381.

Wennberg, C.L., T. Murtola, B. Hess, and E. Lindahl. 2013. Lennard-Jones Lattice Summation in Bilayer Simulations Has Critical Effects on Surface Tension and Lipid Properties. *J. Chem. Theory Comput.* 9:3527–3537. doi:10.1021/ct400140n.

West, J.W., D.E. Patton, T. Scheuer, Y. Wang, A.L. Goldin, and W.A. Catterall. 1992. A cluster of hydrophobic amino acid residues required for fast Na (+)-channel inactivation. *Proc. Natl. Acad. Sci.* 89:10910–10914.

Xiong, W., R.A. Li, Y. Tian, and G.F. Tomaselli. 2003. Molecular Motions of the Outer Ring of Charge of the Sodium Channel. *J. Gen. Physiol.* 122:323–332. doi:10.1085/jgp.200308881.

Yang, J., P.T. Elllnor, W.A. Sather, J.I.F. Zhang, and R.W. Tsien. 1993. Molecular determinants of Ca2+ selectivity and ion permeation in L-type Ca2+ channels. *Nature*. 366:158–161.

Yue, L., B. Navarro, D. Ren, A. Ramos, and D.E. Clapham. 2002. The cation selectivity filter of the bacterial sodium channel, NaChBac. *J. Gen. Physiol.* 120:845–853.

Zhang, X., W. Ren, P. DeCaen, C. Yan, X. Tao, L. Tang, J. Wang, K. Hasegawa, T. Kumasaka, J. He, J. Wang, D.E. Clapham, and N. Yan. 2012. Crystal structure of an orthologue of the NaChBac voltage-gated sodium channel. *Nature*. 486:130–134. doi:10.1038/nature11054.

Zhong, Q., P.B. Moore, D.M. Newns, and M.L. Klein. 1998. Molecular dynamics study of the LS3 voltage-gated ion channel. *FEBS Lett.* 427:267–270. doi:10.1016/S0014-5793(98)00304-4.

Zhorov, B.S., and D.B. Tikhonov. 2013. Ligand action on sodium, potassium, and calcium channels: role of permeant ions. *Trends Pharmacol. Sci.* 34:154–161. doi:10.1016/j.tips.2013.01.002.

Zwanzig, R.W. 1954. High-Temperature Equation of State by a Perturbation Method. I. Nonpolar Gases. *J. Chem. Phys.* 22:1420–1426. doi:10.1063/1.1740409.

7 Curriculum Vitae

Personal Information:

Given Name: **Song** Family Name: **Ke** Date of Birth: **05.07.1987**

Gender: **Male** Nationality: **China** Email: **song.ke@univie.ac.at**

Educations:

2011.10- **PhD student** in international PhD program '**Moltag**', Molecular Modeling lab, Department of Pharmacology and Toxicology, University of Vienna

2009-2010 **MSc** in Drug Discovery, The School of Pharmacy, University of London

Relevant Academic Projects:

2014.04-2014.06 Molecular dynamics simulations on TRPV1 cryo-EM structures and GPU computing. (University of Dundee)

2011.10- Molecular dynamics simulations on voltage-gated sodium channels.

2011.03-2011.08 Homology modeling and molecular dynamics simulation studies on Ion channel: TRPM8. (Queen's University Belfast)

2010.10-2011.02 Docking studies to identify glycosylated-novobiocins' potential binding pockets in human HSP90 full-length 3D structure. (The School of Pharmacy, University of London)

2010.05-2010.09 Computer-aided target fishing for novel Aryl-aminopyridine analogues. (The school of Pharmacy, University of London)

Academic Skills and Knowledge:

In-silico Bioinformatics

Operating Environment:
Linux, Windows, Mac

Biophysics:
Molecular dynamics simulation (GROMACS, atomistic & coarse-grained), Thermodynamics, Statistical mechanics, Electrostatics (beginner).

Scripting:
Shell (Full work proficiency): Sed, Awk, etc;
Python (Full work proficiency): Numpy, Scipy, Matplotlib, etc;
Tcl/tk (Limited work proficiency): rendering figures and movies in VMD

Biostatistics:
Principle Component Analysis (PCA), Partial Least Squares Regression (PLS)

Publications:

1. R. Cervenka, P. Lukacs, V.S. Gawali, **S. Ke**, X. Koenig, L. Rubi, The pivot point for channel activation in a bacterial Na+ channel structure is a determinant of inactivation in mammalian Na+ channels. Submitted
2. **S. Ke**, E.N. Timin, A. Stary-Weinzinger, Different Inward and Outward Conduction Mechanisms in NaVMs Suggested by Molecular Dynamics Simulations, PLoS Comput Biol. 10 (2014) e1003746. doi:10.1371/journal.pcbi.1003746.
3. P. Lukacs, V.S. Gawali, R. Cervenka, **S. Ke**, X. Koenig, L. Rubi, et al., Exploring the structure of the voltage-gated Na^+ channel by an engineered drug access pathway to the receptor site for local anesthetics, J. Biol. Chem. 289 (2014) 21770–21781. doi:10.1074/jbc.M113.541763.
4. **S. Ke**, E.-M. Zangerl, A. Stary-Weinzinger, Distinct interactions of Na^+ and Ca^{2+} ions with the selectivity filter of the bacterial sodium channel NaVAb, Biochemical and Biophysical Research Communications. 430 (2013) 1272–1276. doi:10.1016/j.bbrc.2012.12.055.
5. S. Erić, **S. Ke**, T. Barata, T. Solmajer, J. Antić Stanković, Z. Juranić, et al., Target fishing and docking studies of the novel derivatives of aryl-aminopyridines with potential anticancer activity, Bioorg. Med. Chem. 20 (2012) 5220–5228. doi:10.1016/j.bmc.2012.06.051.
6. M. Sgobba, O. Olubiyi, **S. Ke**, S. Haider, Molecular dynamics of HIV1-integrase in complex with 93del - a structural perspective on the mechanism of inhibition, J. Biomol. Struct. Dyn. 29 (2012) 863–877. doi:10.1080/07391102.2012.10507418.
7. S.M. Patel, M. de la Fuente, **S. Ke**, A.M.R. GuimarŃes, A.O. Oliyide, X. Ji, et al., High throughput discovery of heteroaromatic-modifying enzymes allows enhancement of novobiocin selectivity, Chemical Communications. 47 (2011) 10569–10571.

Poster Presentations:

1. A novel gating mechanism of the NavMs selectivity filter suggested by molecular dynamics simulations; 58th Biophysical meeting/San Francisco, USA (2014)
2. Sodium flux in bacterial sodium channel NavMs from MD simulations; 5th OGMBT meeting/ Innsbruck, Austria (2013)
3. Computational insights into atomistic details of Na^+ versus Ca^{2+} discrimination in sodium channel NavAb; 57th Biophysical meeting/ Philadelphia, USA (2013)
4. First computational insights into atomistic details of Na^+ versus Ca^{2+} discrimination in a bacterial sodium channel; Cold spring harbor (CHINA) - Ion Channels: Biophysics, Diseases and Therapeutics meeting. Suzhou, China (2012)

Papers and Posters print (PDF) can be provided as requested!